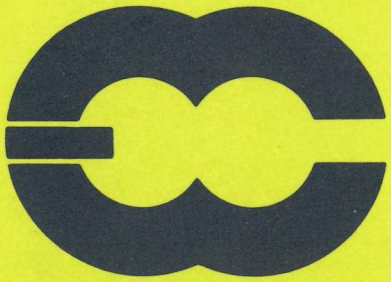

European Centre
for Medium Range
Weather Forecasts

Comparative Extended Range Numerical Integrations with the E.C.M.W.F. Global Forecasting Model 1: The N24, Non-Adiabatic Experiment

Internal Report 6
Research Dept. March 77

Centre Européen pour les Prévisions Météorologiques
a Moyen Terme

Europäisches Zentrum Für Mittelfristige Wettervorhersagen

COMPARATIVE EXTENDED RANGE NUMERICAL INTEGRATIONS WITH THE E.C.M.W.F. GLOBAL FORECASTING MODEL 1: THE N24, NON-ADIABATIC EXPERIMENT

By

D.J. Gauntlett, D.M. Burridge and K. Arpe

European Centre for Medium Range Weather Forecasts, Bracknell

Internal Report No. 6 March 1977
RESEARCH DEPARTMENT

1. Introduction

An essential prerequisite to the successful development and implementation of any new operational NWP model is the thorough testing and evaluation of the various options exercised in selecting a particular numerical framework for integrating the equations of atmospheric flow. As far as construction of the first operational extended range forecasting model for the E.C.M.W.F. is concerned, this design and evaluation process has now reached an advanced stage, see for example, BURRIDGE (1976), BURRIDGE and HASELER (1977) . The purpose of this paper is to complement and extend these earlier results by reporting on a recent comparative extended range numerical experiment involving the GFDL global forecasting model (MANABE et al (1974)) and a prototype E.C.M.W.F. model which includes all of the physical parameterisations of the former but differs significantly in terms of numerical design.

The experiment involves comparison of a ten day integration with the E.C.M.W.F. model at N24 resolution (hereinafter referred to as the D24 result) with corresponding integrations of the GFDL model at both N24 and N48 resolution. The very preliminary nature of the D24 result should be emphasised as this represents the first ten day integration made with the E.C.M.W.F. formulation and considerable subsequent consolidation is anticipated. To assist in the evaluation process the comprehensive diagnostic verification package designed by ARPE et al (1976) has been employed. In addition to computing the usual bulk verification statistics such as RMS error, correlation coefficients etc., this package has the ability to stratify and display verification parameters in a wide variety of space and time domains. All experiments are based on the real data analyses prepared by MIYAKODA et al (1970) for 1 March 1965 and used previously in many studies by the GFDL group.

2. Main features of the respective models:

2.1 The E.C.M.W.F. model

(a) The differential equations

Although coded independently, the E.C.M.W.F. model formulation used in this study is similar to that described by BURRIDGE and HASELER (1977) (hereinafter referred to as I) and only an abbreviated description is therefore necessary here. Thus, using the so-called "sigma" vertical coordinate system, the equations of motion for a hydrostatic atmosphere obeying the perfect gas law may be written :

$$\frac{\partial u}{\partial t} = \frac{1}{\cos\theta} Z\, p_s\, v \cos\theta - \frac{1}{a\cos\theta}\frac{\partial H}{\partial \lambda} - \frac{RT}{a\cos\theta}\frac{\partial}{\partial\lambda}(\ell n p_s) - \dot{\sigma}\frac{\partial u}{\partial\sigma} + F_u \qquad (1)$$

$$\frac{\partial v}{\partial t} = - Z\, p_s\, u - \frac{1}{a}\frac{\partial H}{\partial\theta} - \frac{RT}{a}\frac{\partial}{\partial\theta}(\ell n p_s) - \dot{\sigma}\frac{\partial v}{\partial\sigma} + F_v \qquad (2)$$

$$\frac{\partial(p_s T)}{\partial t} = - \frac{1}{a\cos\theta}\left\{\frac{\partial}{\partial\lambda}(p_s u T) + \frac{\partial}{\partial\theta}(p_s v\cos\theta\, T)\right\} - \frac{\partial}{\partial\sigma}(\dot{\sigma} p_s T) + \left[\frac{RT\omega}{\sigma c_p}\right] + Q \qquad (3)$$

$$\frac{\partial(p_s q)}{\partial t} = - \frac{1}{a\cos\theta}\left\{\frac{\partial}{\partial\lambda}(p_s u q) + \frac{\partial}{\partial\theta}(p_s v\cos\theta\, q)\right\} - \frac{\partial}{\partial\sigma}(\dot{\sigma} p_s q) + S \qquad (4)$$

$$\frac{\partial p_s}{\partial t} = - \frac{1}{a\cos\theta}\left\{\frac{\partial}{\partial\lambda}(p_s u) + \frac{\partial}{\partial\theta}(p_s v\cos\theta)\right\} - \frac{\partial}{\partial\sigma}(\dot{\sigma} p_s) \qquad (5)$$

$$\frac{\partial\phi}{\partial\ell n\sigma} = - RT \qquad (6)$$

where,

$$Z = \frac{1}{p_s\cos\theta}\left\{f\cos\theta + \frac{\partial v}{\partial\lambda} - \frac{\partial(u\cos\theta)}{\partial\theta}\right\}$$

and,

$$H = \phi + \tfrac{1}{2}\left\{u^2 + \frac{1}{\cos\theta} v^2\cos\theta\right\}$$

Finally, the surface pressure tendency equation and the diagnostic equations for $p_s\dot{\sigma}$ and $\left|\frac{RT\omega}{c_p\sigma}\right|$ are readily obtained by appropriate vertical integration of (5) and use of the lower and upper boundary conditions, $(\dot{\sigma}p_s)_{\sigma=0}=0$ and $(\dot{\sigma}p_s)_{\sigma=1}=0$. These remaining differential equations take the form:

$$\frac{\partial p_s}{\partial t} = -\int_0^1 \frac{1}{a\cos\theta}\left\{\frac{\partial}{\partial\lambda}(p_s u) + \frac{\partial}{\partial\theta}(p_s v\cos\theta)\right\} d\sigma \qquad (7)$$

$$p_s\dot{\sigma} = -\frac{\partial p_s}{\partial t} - \int_0^\sigma \frac{1}{a\cos\theta}\left\{\frac{\partial}{\partial\lambda}(p_s u) + \frac{\partial}{\partial\theta}(p_s v\cos\theta)\right\} d\sigma \qquad (8)$$

$$\left|\frac{RT\omega}{\sigma c_p}\right| = \frac{RT}{\sigma c_p}\int_0^\sigma \frac{1}{a\cos\theta}\left\{\frac{\partial}{\partial\lambda}(p_s u) + \frac{\partial}{\partial\theta}(p_s v\cos\theta)\right\} d\sigma$$

$$+ \frac{RT}{a\cos\theta c_p}\left\{p_s u\frac{\partial}{\partial\lambda}(\ell n p_s) + p_s v\cos\theta\frac{\partial}{\partial\theta}(\ell n p_s)\right\} \qquad (9)$$

(b) The finite difference equations

The horizontal grid used in the model is the so-called Arakawa C grid which has been used very successfully by ARAKAWA and LAMB (1976), and also, BURRIDGE (1975). The vertical distribution of variables is quite conventional with horizontal wind components, temperature and mixing ratio stored at the main levels, k, whilst the vertical velocity σ and the geopotential ϕ are stored at intermediate hald levels $k + \frac{1}{2}$.

Thus using the notation,

$$\Delta_x A(x) = A(x+\tfrac{\Delta x}{2}) - A(x-\tfrac{\Delta x}{2})$$

$$\bar{A}^x = \tfrac{1}{2}\{A(x+\tfrac{\Delta x}{2}) + A(x-\tfrac{\Delta x}{2})\}$$

$$\delta_x A = \{A(x+\tfrac{\Delta x}{2}) - A(x-\tfrac{\Delta x}{2})\}/\Delta x$$

for spatial differences envolving x,y and σ; and for the time dimension, the particular differencing operator

$$\delta_t A = \{A(t+\tfrac{\Delta t}{2}) - A(t-\tfrac{\Delta t}{2})\}/\Delta t$$

where,

$$\tilde{A}(t-\Delta t)=A(t-\Delta t)+\alpha(A(t-2\Delta t)-2A(t-\Delta t)+A(t))$$

and $\alpha=0.005$, equations (1) to (9) may be re-written in the following form;

$$\delta_t u = \frac{1}{\cos\theta}\,\bar{Z}^{\lambda}\,\overline{V}^{\lambda\theta} - \frac{1}{a\cos\theta}\delta_\lambda H - \frac{R\bar{T}^{\lambda}}{a}\delta_\lambda(\ell n p_s) - \frac{1}{\overline{p_s}^{\lambda}}\,\frac{\overline{p\dot{\sigma}}^{\lambda}\,\Delta_\sigma u}{\Delta_\sigma \sigma} + F_u \qquad (10)$$

$$\delta_t v = -\bar{Z}^{\theta}\,\bar{U}^{\lambda\theta} - \frac{1}{a}\delta_\theta H - \frac{R\bar{T}^{\theta}}{a}\delta_\theta(\ell n p_s) - \frac{1}{\overline{p_s}^{\theta}}\,\frac{\overline{p_s\dot{\sigma}}^{\theta}\,\Delta_\sigma v}{\Delta_\sigma \sigma} + F_v \qquad (11)$$

$$\delta_t(p_s T) = -\frac{1}{a\cos\theta}\{\delta_\lambda(U\bar{T}^{\lambda}) + \delta_\theta(V\bar{T}^{\theta})\} - \delta_\sigma(\dot{\sigma}p_s\bar{T}^{\sigma}) + \left[\frac{R}{c_p}\,\frac{T\omega}{\sigma}\right] + Q \qquad (12)$$

$$\delta_t(p_s q) = -\frac{1}{a\cos\theta}\{\delta_\lambda(U\bar{q}^{\lambda}) + \delta_\theta(V\bar{q}^{\theta})\} - \delta_\sigma(\dot{\sigma}p_s\bar{q}^{\sigma}) + S \qquad (13)$$

$$Q_{k+\frac{1}{2}} = Q_s + \sum_{\ell=k+1}^{KMAX} RT_\ell(\Delta_\sigma \ell n\sigma)_\ell \qquad (14)$$

$$\delta_t p_s = -\frac{1}{a\cos\theta}\sum_{\ell=1}^{KMAX}(\delta_\lambda U + \delta_\theta(V\cos\theta))_\ell\,(\Delta_\sigma)_\ell \tag{15}$$

$$(p_s\dot{\sigma})_{k+\frac{1}{2}} = -\frac{1}{a\cos\theta}\sum_{\ell=1}^{k}(\delta_\lambda U + \delta_\theta(V\cos\theta))_\ell\,(\Delta_\sigma)_\ell - \sigma_{k+\frac{1}{2}}\,\delta_t(p_s) \tag{16}$$

$$\left|\frac{RT\omega}{c_p\sigma}\right|_k = -\frac{R}{c_p}\frac{\Delta_\sigma \ell n\sigma}{\Delta_\sigma\sigma}\left[\sum_{\ell=1}^{k}(\delta_\lambda U + \delta_\theta(V\cos\theta))_\ell\,(\Delta_\sigma\sigma)_\ell\right]$$

$$-\frac{R}{c_p}\frac{\Delta_\sigma \ell n\sigma}{\Delta_\sigma\sigma}\beta_k(\delta_\lambda U + \delta_\theta(V\cos\theta))_k\,\Delta\sigma_k$$

$$+\frac{R}{c_p}\frac{i}{a\cos}\left[\overline{\overline{T}^{\lambda}\,U\delta_\lambda(\ell n p_s)}^{\lambda} + \overline{\overline{T}^{\theta}\,V\delta_\theta(\ell n p_s)}^{\theta}\right]$$

where,

$$U = \overline{p_s}^{\lambda}u \qquad , \quad V = \overline{p_s}^{\theta}\,v\cos\theta,$$

$$Z = \frac{1}{p_s\cos\theta}\lambda\theta\left[f\cos\theta + \delta_\lambda v - \delta_\theta(u\cos\theta)\right],$$

$$H = \phi + \tfrac{1}{2}\left(\overline{u^2}^{\lambda} + \frac{1}{\cos\theta}\,\overline{v^2\cos\theta}^{\theta}\right)$$

and,

$$\beta_k = \ell n(\sigma_{k+\frac{1}{2}}/\sigma_k)\ /\ \ell n(\sigma_{k+\frac{1}{2}}/\sigma_{k-\frac{1}{2}})$$

Particular differencing procedures are obviously required in the vicinity of the polar singularities. These procedures, which are fully described in I and therefore not repeated, ensure conservation within the model of mass and potential enstrophy. Special filtering procedures are also required at high latitudes to overcome the severe restriction on numerical stability arising from the convergence of the meridians to the poles. Again the procedures outlined in I involving the application of a latitudinally dependent spatial filtering operator have been found to be most satisfactory in ameliorating this problem.

(c) Non-adiabatic terms

With the exception of the contributions to F_u and F_v in equations (1) and (2) resulting from horizontal numerical diffusion, the formulations for all non-adiabatic terms are identical to those contained in the GFDL model and summarized in Table 2. In this preliminary experiment, horizontal diffusion in the ECMWF model was modelled according to a very simple $K\nabla^2$ formulation with $K = 2.5 \times 10^5$ m^2 s^{-1}.

2.2 The GFDL model

As the GFDL model has already been extensively described in the literature, e.g. MANABE, HOLLOWAY and SPELMAN (1974), only a brief summary of the essential model characteristics will be included here. These are listed in Tables 1 and 2.

Numerical Aspect

1.	Horizontal Grid	Modified Kurihara (N24 or N48 resolution).
2.	Vertical Grid	Nine level, sigma coordinate .
3.	Space finite difference scheme	Centred, second order, energy conserving flux form. Non staggered grid.
4.	Time differencing	Euler backward for $t \leq 12$ hrs. Centred leap frog scheme with periodic time smoothing for $t > 12$ hrs.

TABLE 1 : Primary Numerical Characteristics of the GFDL model.

PHYSICAL PARAMETERISATION	TYPE AND COMMENTS
1. Radiation	MANABE and STRICKLER (1964) / MANABE and WETHERALD (1967). Radiation calculation is dependent on: (i) Climatological distribution of absorbers (H_2O, CO_2, O_3) (ii) Climatological surface temperature for sea and sea ice points. (iii) Specified zonal mean cloudiness. (iv) Specified limits of sea ice extent. (v) Time dependent surface albedo influenced by snow, soil moisture, ice. (vi) Specified absorptivity, reflectivity and height of zonal mean clouds.
2. Horizontal Diffusion	SMAGORINSKY (1963) non linear type.
3. Vertical Diffusion	Mixing length hypothesis. ℓ = 0 at 2.5 km. No vertical diffusion of temperature.
4. Surface Fluxes	Bulk aerodynamic formulae. C_d = 0.002.
5. Convection (moist and dry)	Energy conserving convective adjustment type. Critical relative humidity for onset of moist adjustment = 0.8.
6. Hydrology	Account taken of rainfall, evaporation, snow accumulation, snow melt and run-off.

TABLE 2 : SUMMARY OF PHYSICAL PARAMETERISATIONS INCLUDED IN THE GFDL MODEL

3. Results

In order to coherently summarise the results of the investigation, and also to facilitate comparison with previous and future experimental extended range integrations conducted at the ECMWF, the comprehensive display and verification package used by ARPE et al (1976) has also been used in this study. It is convenient therefore to partition results into three sections. The first section will be concerned with a synoptic review of the experiment and will include presentation of daily and time averaged 1000 mb and 500 mb charts, together with a selection of relevant Hovmöller and cyclone trajectory diagrams. Next, consideration will be given to conventional verification parameters (RMS errors, anomaly correlation coefficients etc.). Finally, verifications will be included of key diagnostic parameters such as kinetic energy and available potential energy as well as the transfer between these quantities. As appropriate, the results of all sections will be stratified into four spectral domains; zonal flow, wave numbers 1 to 3, 4 to 9, and 10 to 20. The NMC operational analyses are again used as a verification base.

3.1 Synoptic comparison

The case study chosen for the comparative integrations is the Northern hemisphere late winter situation, 00Z 1/3/65. The situation has been previously used extensively by the GFDL group, and also, in earlier experimental extended range integrations at the ECMWF by ARPE et al (1976). The situation is characterised by, see fig. 3.1.1, an active large scale tilting trough over Western Europe with a marked SW/NE orientation; a strong stationary high pressure area over Siberia; an active slow moving large scale trough over the Central Pacific; and, an initially weak low level cyclone over the U.S. with its attendant upper level trough at 500 mb.

During the course of the next ten days, see figs. 3.1.2 to 3.1.21, a considerable re-organisation of this broad synoptic framework occurs. Thus, after promoting low level cyclogenetic activity during the first four days, the West European trough becomes progressive and moves steadily eastward to be replaced by marked ridges at 1000 mb and 500 mb over Western Europe by day 10. These developments are in harmony with the slow weakening and eventual eastward translation of the Siberian high. By contrast, the Central pacific is dominated by a large scale trough for the entire period. Within this large scale trough smaller scale troughs are generated moving eastward and decaying. Simultaneous and frequent cyclogenesis at 1000 mb can also be seen. During the 10 day period, the main cyclogenetic region shifts westward and this allows the development of a marked surface anticyclone and 500 mb ridge over the eastern Pacific after day 5.

The upper level trough initially over the U.S. progresses steadily eastward and, after a period of repeated cyclogenesis over the continental U.S. and adjacent Eastern waters, leads to the establishment of the major 500 mb trough at 70°W by the tenth day.

The following figures, 3.1.22 to 3.1.25, show the behaviour of troughs and ridges for the respective models during these 10 days by means of Hovmöller's trough-ridge diagrams, but with a spectral decomposition. To facilitate comparison, the axes of the troughs and ridges from the verifying NMC analyses (lowest panel) are repeated in the upper panels.

As can be seen from the 500 mb trough-ridge diagram for latitude 50°N and wave number 1 to 3, fig. 3.1.22, all models enjoy some success in describing these broad scale synoptic evolutions with slight phase and intensity advantages being evident for N48 relative to D24.

Corresponding forecast quality is not maintained in the trough-ridge diagrams for wave numbers 4 to 9. Furthermore, there is evidence of relative N48 superiority in some points. Thus, the trough starting at about 150°E moves to the east for two days and then remains almost stationary. Both, D24 and N24, did not predict this change in propagation velocity. The ridge starting at about 280°E remains stationary for three days and then propagates to the east. Again the D24-and N24 run do not predict the change in propagation velocity. Different conclusions emerge, however, when the stationary component of this figure is removed. Figures 3.1.24 and 3.1.25, for example, show trough-ridge diagrams of the 500 mb transient waves at 40°N. For easier comparison figure 3.1.24 shows only the axes of troughs and ridges but not their intensities, while figure 3.1.25 gives their intensities. The D24 run now seems to be the superior forecast. The trough and ridge starting at 230°E and 250°E respectively are predicted best by D24, the ones starting at 90°, 110°, 290° and 310° are of the same quality for D24 and N48, while N24 is failing mostly.

Further evidence of the relative success of the models in a broader space and time context can be gauged from figs. 3.1.26 to 3.1.27 which show forecast five day mean 500 mb anomaly charts for the D24 and N48 models centred on days 2.5 and 7.5 of the prediction. To facilitate verification, the figures also include March climatology and the corresponding observed anomalies based on the NMC operational analyses. For the first five day averaging period, the anomalies forecast by both models verify exceptionally well. Even for the second period there is reasonable agreement although significant discrepancies are evident over Western Europe and the Eastern Atlantic. The reasons for these discrepancies will emerge in the more detailed discussion to follow.

Another feature of the anomaly forecasts which will be the subject of later detailed scrutiny is the isolation of the anomaly centre near 140°E during the second period. This centre, it will be seen, is associated with the retrogression of a preferred area of cyclogenetic activity during the latter stage of the forecast and is correctly simulated in general terms by both models.

Considerable care must be exercised in assessing individual model forecasts for particular days. This is especially so during the latter stages of the forecast period when seemingly good verifications of individual synoptic systems can arise even though the evolutinary processes which have produced a particular synoptic distribution are quite in error. In order to further elucidate this problem, forecast and observed trajectories for all major depressions N of 40°N for the D24 model are shown in fig. 3.1.28. Here, forecast trajectories are indicated by the full line and observed trajectories by the dashed line. Individual cyclones may be identified by the larger bold numbers preceding each trajectory. In the European sector, the forecast trajectories of cyclone 1 (37.5°N, 15°W) and cyclone 4 (70°N, 25°E) are realistic. Although somewhat delayed, the genesis of cyclone 2 over the Norwegian Sea is correctly predicted. The forecast subsequent movement of this depression is however very poor.

The formation of cyclone 3 on the second day (67°N, 78°W) was well forecast, although subsequent verification is poor. In the forecast this feature merges with an old cyclone, which originally came from the Pacific and becomes stationary while in reality it moves to the Norwegian Sea. This failure, coupled with the poor prediction of cyclone 2, gives a bad forecast over Western Europe.

Over the Pacific we find reasonable forecasts of some cyclone developments. For example, cyclones 12 and 13 were forecast well up to day 3. New cyclogeneses near Japan (cyclone 11) on day 2 or 3 and its further development up to day 7 were also well predicted. As far as later cyclogenetic events are concerned however there is little correspondence between the forecast and reality. Despite this deficiency, the broad path of forecast cyclone trajectories is reasonable. Notice also that toward the end of the forecast period there is a tendency for the main cyclogenetic area to retrogress westward (cyclone 16, 40°N, 135°W; cyclone 17, 48°N, 135°W). This tendency is also observed in the forecast model (cyclone 15, 35°N, 140°W).

Forecast trajectories in the major Western Atlantic trough area also indicate broad qualitative agreement with reality. However, the eventual translation of cyclone 5 (37.5°N, 60°W) into Western Europe is a notable failure and associated no doubt with previously mentioned forecast failures in the European sector during the first three or four days of the forecast.

So far detailed synoptic comment has been focussed almost entirely on the D24 model. In order to highlight quality differences between the D24, N48 and N24 models, the following specific synoptic examples are cited for 1000 mb and 500 mb respectively:

(a) 1000 mb

1. Mention has already been made of the failure of the D24 model to adequately represent cyclogenetic developments over Western Europe during the initial stage of the forecast. Inspection of the respective model outputs for day 3 shows that position errors associated with the rapid southerly translation of the cyclone along 0^{o} E are slightly reduced in the N48 model, probably as result of superior N/S resolution. By day 4 however this advantage has been lost as the cyclone in all models curves prematurely eastward. The D24 and N48 are superior to N24 both in terms of movement and intensity.

2. Near Newfoundland, a slow moving depression dominates the first few days of the forecast period. Until day 3 all models describe the evolution of this feature satisfactorily. Beyond day 3 all models predict a spurious north eastward movement which is more accentuated in the N48 model. D24 is superior to N24 and N48 both in terms of general forecast character and also specific location and intensity.

3. Comparison of the N48 and D24 forecasts for day 9 underline the comparable performance of these models even though synoptic features in the former are for the most part more intense (but not necessarily more correct !). This is especially evident for systems with marked meridional extent. The N24 model by contrast appears to be diverging fairly rapidly both from reality and the former models. Another feature which is evident in the day 9 forecast is the continued successful prediction of the evolution of the Siberian high.

(b) 500 mb

1. During the first two or three days of the 500 mb forecast, the D24 model performs as well, perhaps even slightly better in some instances than the N48 model and is significantly superior to the N24 model. The 500 mb forecast for day 3 highlights some of these aspects. Note for example, the successful prediction of a small high pressure cell over the Western U.S. by the D24 model and the generally good position and intensity verification of most major synoptic features.

(b) 500 mb (continued)

2. However with increasing forecast extent, see for example day 8, it is evident that the N48 model is able to maintain more definition and intensity in the major planetary waves. There are also synoptic features such as the marked ridge off the West coast of the U.S. which are exclusive to the N48 model. The D24 model,however, remains generally superior to the N24 model.

In summary, all models but more especially the N48 and D24 models demonstrate some ability in being capable of delineating over the ten day forecast period the evolution of broader scale synoptic aspects such as the movement of primary areas of cyclogenetic action. Except for isolated cases, however, predictions associated with individual synoptic systems do not verify exceptionally well for periods in excess of approximately three to four days. In this regard, the developments of individual models are more similar to each other than to the real atmosphere with closer correspondence between D24 and N48 than between D24 and N24.

3.2 Objective verifications

There is no unanimity among meteorologists as to the best method of statistically measuring the skill or otherwise of a particular numerical forecast. MIYAKODA et al (1972) include comprehensive discussion and examples of several of the more common methods used. In this report, consideration is given to only two verification parameters, root mean square error and anomaly correlation coefficients, however an extensive variety of presentation and sampling formats is employed.

Fig. 3.2.1, for example, shows RMS height errors for the respective models averaged over the atmospheric layer 1000 - 200 mb north of 20^{o}N and plotted as a function of forecast extent. An interesting aspect of these results is the relatively good performance of the D24 model especially in the wave number 4 - 9 domain. This is further emphasised in figure 3.2.2 where mean total RMS errors between 20^{o}N and 82.5^{o}N are displayed as a function of pressure. It shows the commonly observed characteristic of NWP models for the high RMS errors associated with the larger natural variance in the upper atmosphere to gradually spread to lower levels. There is also an error propagation upward from the surface. Again however the relatively good performance of the D24 model at all levels is noteworthy.

Similar conclusions can be drawn from figure 3.2.3 which shows the corresponding latitudinal distribution of RMS height errors. The patterns are characterised by maxima near 40^{o}N and 65^{o}N which are probably associated with higher natural atmospheric variance in the vicinity of the sub-tropical and polar front jets respectively.

The most substantial RMS error differences between the respective models however are observed in the lower level forecast temperature fields. Fig. 3.2.4, for example, shows RMS 850 mb temperature errors again displayed as a function of time and spectral interval. The clear superiority of the D24 model is manifestly evident especially for wave numbers 4 - 9 and for periods in excess of 3 days.

Before attempting to reach any substantive conclusions from the above results it is advantageous to inspect the corresponding verifications based on anomaly correlation coefficients. These verifications are shown in figs. 3.2.5 and 3.2.6 and broadly similar comments can be made to those relating to RMS errors. A notable exception however is the tendency for correlation errors to propagate upward from the lower layers of the atmosphere. This is due to the normalising effect of the correlation coefficients. Notice also that D24 superiority is now confined mostly to higher levels, this contrasts to the vertical distribution of RMS errors where the D24 model maintained a general superiority at all levels.

In summary, it would appear that the D24 model, despite resolution disadvantagesin the N/S direction and in E/W direction at lower latitudes, displays a level of objective verification accuracy which is at least comparable, and in some instances superior, to the N48 model. What explanations can be given for this rather unexpected result ? Part of the answer of course lies in the notorious sensitivity of the RMS error statistics to any smoothing of forecast fields. In this context, the use in the D24 model of a finite difference scheme with less inherent computational noise and a less scale selective "del squared" diffusion scheme are advantageous. But this argument does not apply to the correlation coefficients.

3.3 Energetics

In evaluating the results to follow it is advantageous to bear in mind the following aspects of the experimental configuration. First, the energetics from the ECMWF diagnostic package are presently computed on a geostrophic wind basis only. This strategy is reasonable when comparisons are required between a particular NWP model and the real atmosphere. Indeed, due to the paucity of conventional wind observations this is the only satisfactory approach that can be adopted in this instance. For inter model comparisons, however, energetical differences between models may be distorted (especially at smaller scales) due to variations in the numerical definition of geostrophy in the respective models. Secondly, many components of the forecast energy budget are known to be quite sensitive to the type of diffusion scheme used to control high wave number energy accumulation resulting from natural and spurious cascade processes.

As previously mentioned, only a simple linear horizontal diffusion scheme has been used in the D24 model, whereas the N24 and N48 models incorporate the more scale selective non linear parameterisation scheme of SMAGORINSKY (1963). As far as vertical diffusion is concerned, all models have identical parameterisation and parameter settings as described in section 2.

For a broad overview of the energetical response of the various models it is convenient to commence with figure 3.3.1 which shows the spectral partitioning of energy in the D24, N24 and N48 models for the spatial domain 40°N to 60°N and averaged from day 7.5 to day 10. Compared with observation, all models show the familiar underestimation of forecast kinetic energy at low wave numbers. This deficiency is especially pronounced in the lower resolution models. At higher wave numbers there is some evidence of a distortion in the spectra for the N24 and N48 models when comparisons are made with both observations and the theoretical -3 distribution.

Further information relating to the time variation of forecast energy in various spectral bands is given in figure 3.3.2. Several aspects of this figure are worthy of comment. First, all model results indicate an energy deficiency in all spectral intervals prior to forecast commencement. This probably reflects deficiencies in the procedures used to initialise the respective models and is more pronounced in the D24 case where a simple linear interpolation procedure was used to convert the initialised N48 Kuri-grid data to the required staggered grid format. With increasing forecast extent the kinetic energy deficiencies of all models become more pronounced, again especially in the lower resolution models. Furthermore, beyond day 4 the D24 model would appear to be even slightly inferior to the N24 model. This result is surprising in view of the relative quality of the synoptic and objective verifications of the former model and probably reflects the deficiencies of the simple linear diffusion scheme used in that model. For the N48 model, some distortion in the forecast kinetic energy is evident in the wave number 4 - 9 spectral band for periods beyond five days.

In order to provide more details of the spatial distribution of zonal kinetic energy, a meridional cross section of the mean zonal wind averaged over the last three days of the forecast is shown in figure 3.3.3. Whereas only small differences between the respective models were apparent for the overall mean kinetic energy (fig. 3.3.2) and in the vertical profiles of aereal mean zonal wind (right panels of fig. 3.3.3), the meridional cross sections indicate substantial model differences. The subtropical jet is too weak and too far south in all models but especially the D24 run. Furthermore, the D24 model does not show a well defined jet core. In northern areas it is the N24 model which shows some unrealistic features. Here the D24 model has a high zonal resolution and this helps to give results which are closer to reality.

Details of the vertical distribution of eddy kinetic energy are shown in the time-pressure cross sections of figure 3.3.4 and figure 3.3.5. Clearly, all models have difficulty in concentrating energy in the upper troposphere especially in the long waves. The D24 model is the most inferior in this regard.

Discussion now focusses on the forecast available potential energy distributions for the various models. In figure 3.3.6, the time variations of available potential energy expressed as a function of wave number indicate that although the predicted zonal temperature variances are generally too small for all models, the temperature variations in the meridional direction (i.e. the zonal part) are slightly excessive beyond the fifth day. Inspection of the meridional and vertical distributions of available potential energy, figures 3.3.7 and 3.3.8, indicate similar general deficiencies to those already referred to in the kinetic energy discussion. Again, the sharp differences between 500 mb and 300 mb are not reproduced by the models and this is probably associated with the poor numerical definition of the tropopause. The GFDL-N48 and N24 models contain some unrealistically high values at the lowest level of 850 mb which are not found at the D24 run. This may be associated with differences in the finite difference representation in the respective models of the " ω term " in the thermodynamic equation.

Finally, figures 3.3.9 and 3.3.10 show the variation with time of the transfer from zonal kinetic energy to eddy kinetic energy, and the transfer of zonal available potential energy to eddy potential energy respectively. In the lower wave number regions for the first two or three days of the forecast, all models display at least a qualitative ability to predict the evolution of the relevant transfers. Beyond this time however there is little agreement between forecast and observation for any of the models and especially in the high wave number domain. Inspection of the meridional and vertical distribution of the transfer from zonal to eddy kinetic energy (fig. 3.3.11), which is a mean of the first three days, again gives evidence of the similarity between the D24 and N48 runs.

4. Conclusions

In essence, this experiment has been concerned with the task of making a preliminary practical assessment of one component of the E.C.M.W.F.'s first operational extended range forecasting model i.e., the numerical configuration. This assessment has been made in two ways. First, by comparison against the N24 and N48 GFDL model with equivalent non-adiabatic forcing, and secondly, by comparison with NMC operational verification analyses.

Synoptic and objective verifications indicate that the E.C.M.W.F. model (D24) is generally superior to the N24 model and in many instances approaches the performance of the N48 model. However, verification of forecast energetics for the respective models indicate some relative deficiencies for the D24 model. These deficiencies are probably associated with the limitations of the simple linear diffusion scheme used exclusively in the D24 model in this preliminary experiment. This limitation will be relaxed in future experiments.

All models, but more especially the N48 and D24 models demonstrate reasonable ability in being capable of delineating over the ten day forecast period the evolution of broader scale synoptic aspects such as the movement of primary areas of cyclogenetic action. Except for isolated cases, however, predictions associated with individual synoptic systems do not verify exceptionally well for periods in excess of approximately three to four days. In this regard, the performance of individual models is more similar to each other than to the real atmosphere, with closer correspondence between the D24 and N48 models than between D24 and N24.

Acknowledgements

The substantial programming advice and assistance given by Mr. N. Storer and Mr. J.K. Gibson during the course of this study is gratefully acknowledged.

References

Arakawa, A. and Lamb, V.R. (1976) "Computational design of the basic dynamical processes of the UCLA general circulation model". Dept. Meteorology, University of California, Los Angeles.

Arpe, K., Bengtsson, L., Hollingsworth, A. and Janjic, Z. (1976) " A case study of a ten day prediction". ECMWF Technical Report No. 1, 105 pp.

Burridge, D.M. (1975) "A split semi-implicit reformulation of the Bushby-Simpson ten level model". Q.J.R.M.S., 101, pp. 777-792.

Burridge, D.M. (1976) "Preliminary design of the E.C.M.W.F. Forecasting Model - Numerical formulation". Internal ECMWF paper.

Burridge, D.M. and Haseler, J. (1977) "A model for medium range weather forecasting - adiabatic formulation ". (In preparation).

Manabe,S. and Strickler, R.F. (1964) "Thermal equilibrium of the atmosphere with a convective adjustment". J.A.S. 21 pp. 361-385.

Manabe, S. and Wetherald, R.T. (1967) "Thermal equilibrium of the atmosphere with a given distribution of relative humidity". J.A.S. 24, pp. 241-259.

Manabe, S., Holloway,J.L. and Spelman, M.J. (1974) "GFDL Global 9 Level atmospheric model". GARP Publication Series No. 14. pp. 7 - 27.

References (continued)

Miyakoda, K., Moyer,R.W. Stambler, H.M., Clarke, R.H. and Strickler, R.F.	(1971)	"A prediction experiment with a global model on the Kurihara grid". Journal of Met. Soc. of Japan, 49, pp. 521-536.
Miyakoda, K., Hembree,G.D. Strickler, R.F. and Spelman, I.	(1972)	"Cumulative results of extended forecast experiments. I. Model performance for Winter cases". M.W.R., Vol.100, pp. 836 - 855.
Smagorinsky, J.	(1963)	"General circulation experiments with the primitive equation, I., the basic experiment ". M.W.R., Vol. 9, pp.99-152.

EUROPEAN CENTRE FOR
MEDIUM RANGE WEATHER
FORECASTS

Research Department (RD)

Internal Report No. 6

No. 1 Users Guide for the G.F.D.L. Model
(November 1976)

No. 2 The Effect of Replacing Southern Hemispheric
Analyses by Climatology on Medium Range
Weather Forecasts
(January 1977)

No. 3 Test of a Lateral Boundary Relaxation Scheme
in a Barotropic Model
(February 1977)

No. 4 Parameterisation of the surface fluxes
(February 1977)

No. 5 An Improved Algorithm for the Direct Solution of
Poisson's Equation over Irregular Regions
(February 1977)

No. 6 Comparative Extended Range Numerical Integrations
with the E.C.M.W.F. Global Forecasting Model
1: The N24, Non-Adiabatic Experiment
(March 1977)

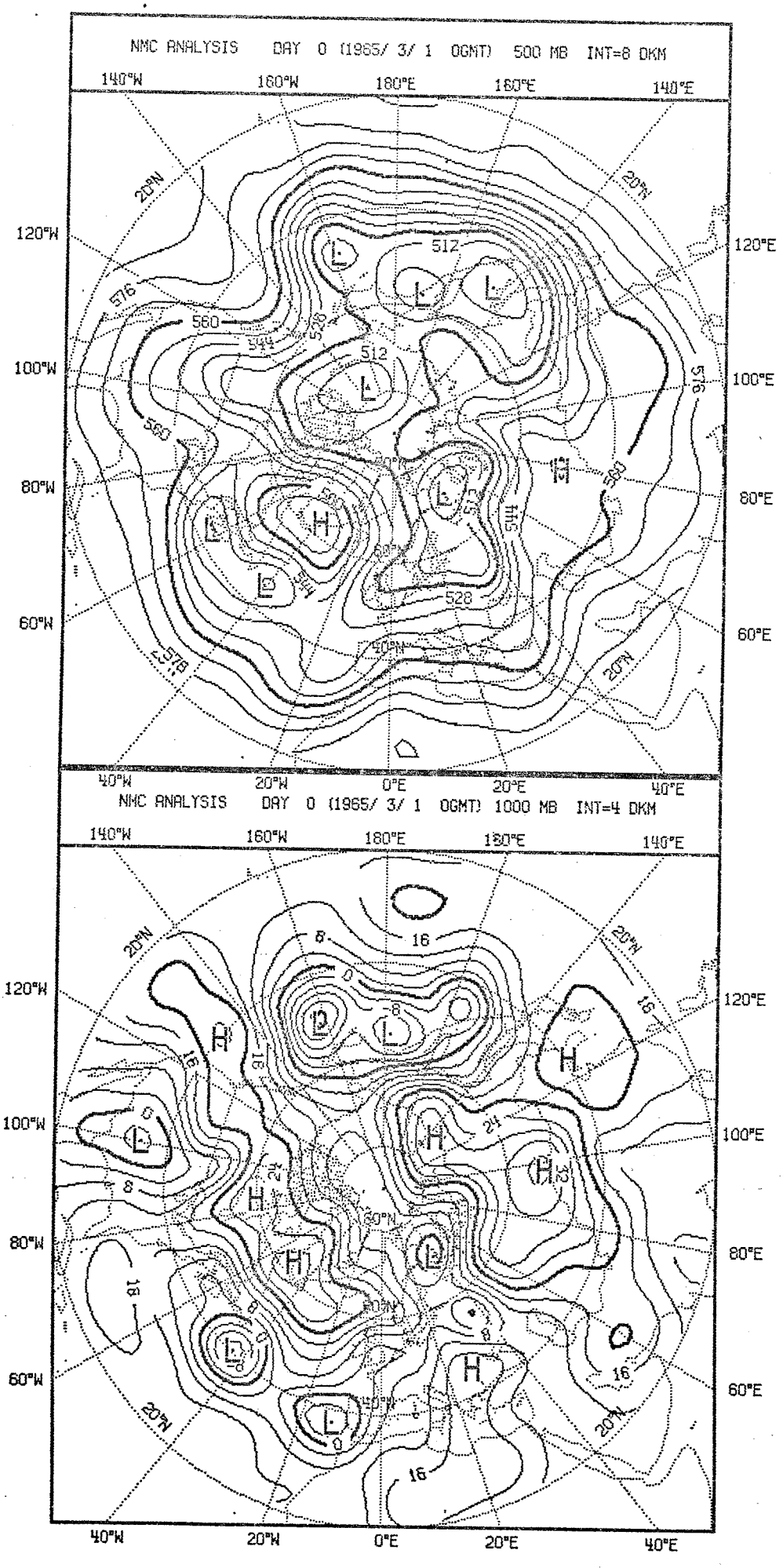

Fig. 3.1.1 : Day 0 observed maps of 500 mb (top) and 1000 mb (bottom) geopotential height.

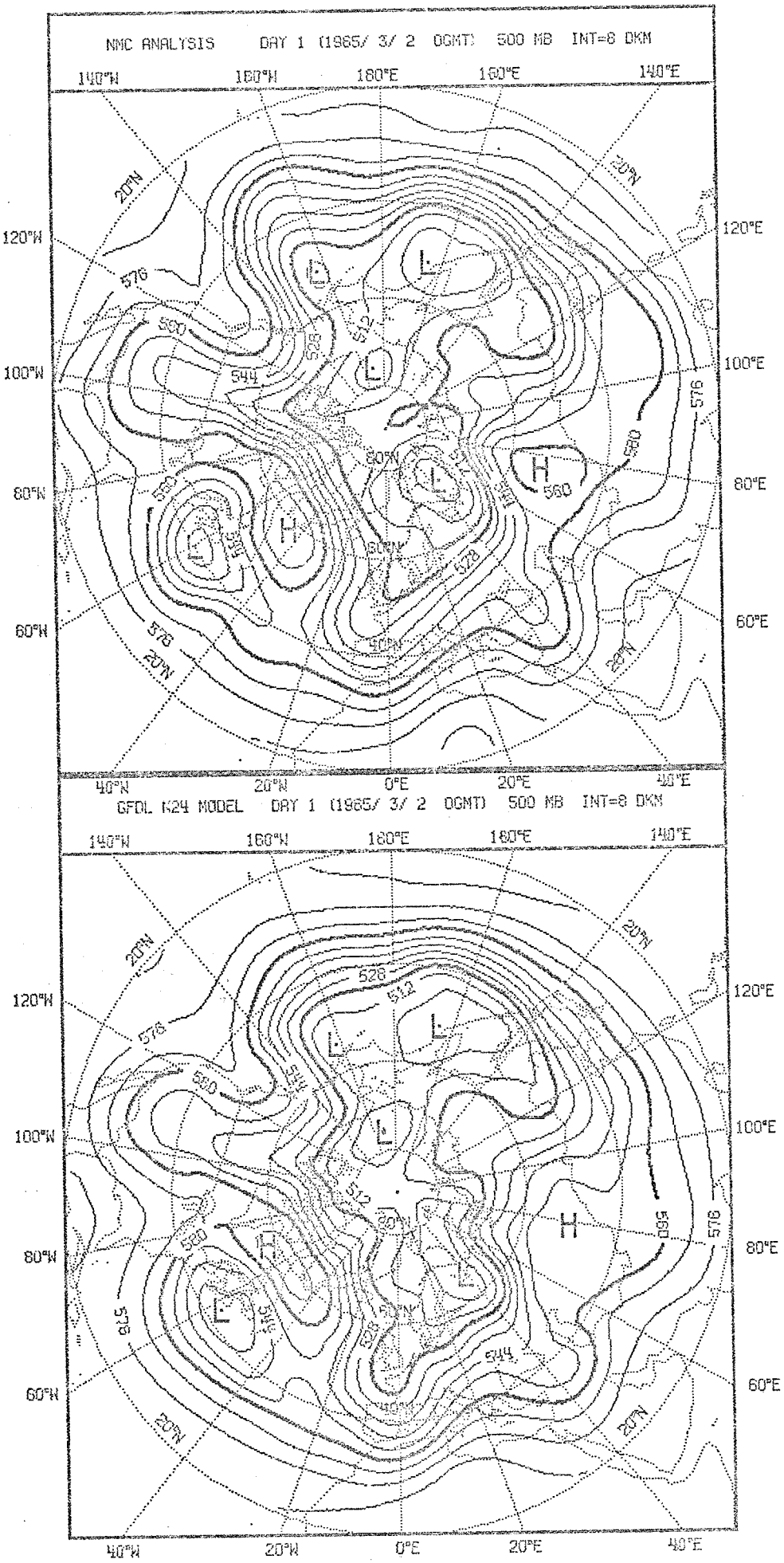
NMC ANALYSIS DAY 1 (1985/ 3/ 2 0GMT) 500 MB INT=6 DKM
140°W
160°W
180°E
160°E
140°E
120°W
100°W
80°W
60°W
120°E
100°E
80°E
60°E
20°N
40°N
20°W
0°E
20°E
40°E
576
560
544
528
512
496
480
H
L
GFDL N24 MODEL DAY 1 (1985/ 3/ 2 0GMT) 500 MB INT=6 DKM

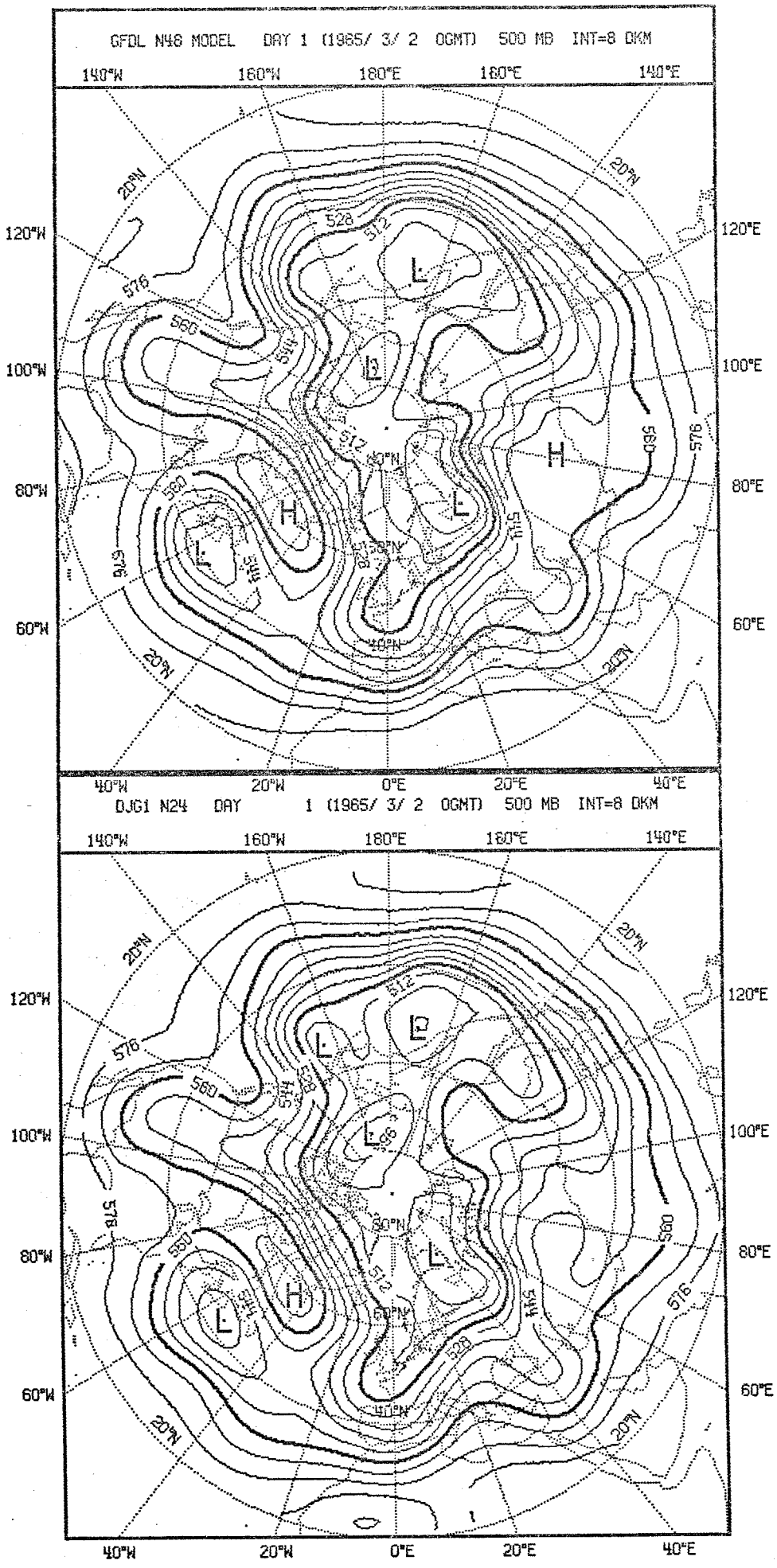

Fig. 3.1.2: Observed (top left) and predicted fields of 500 mb geopotential height, day 1.

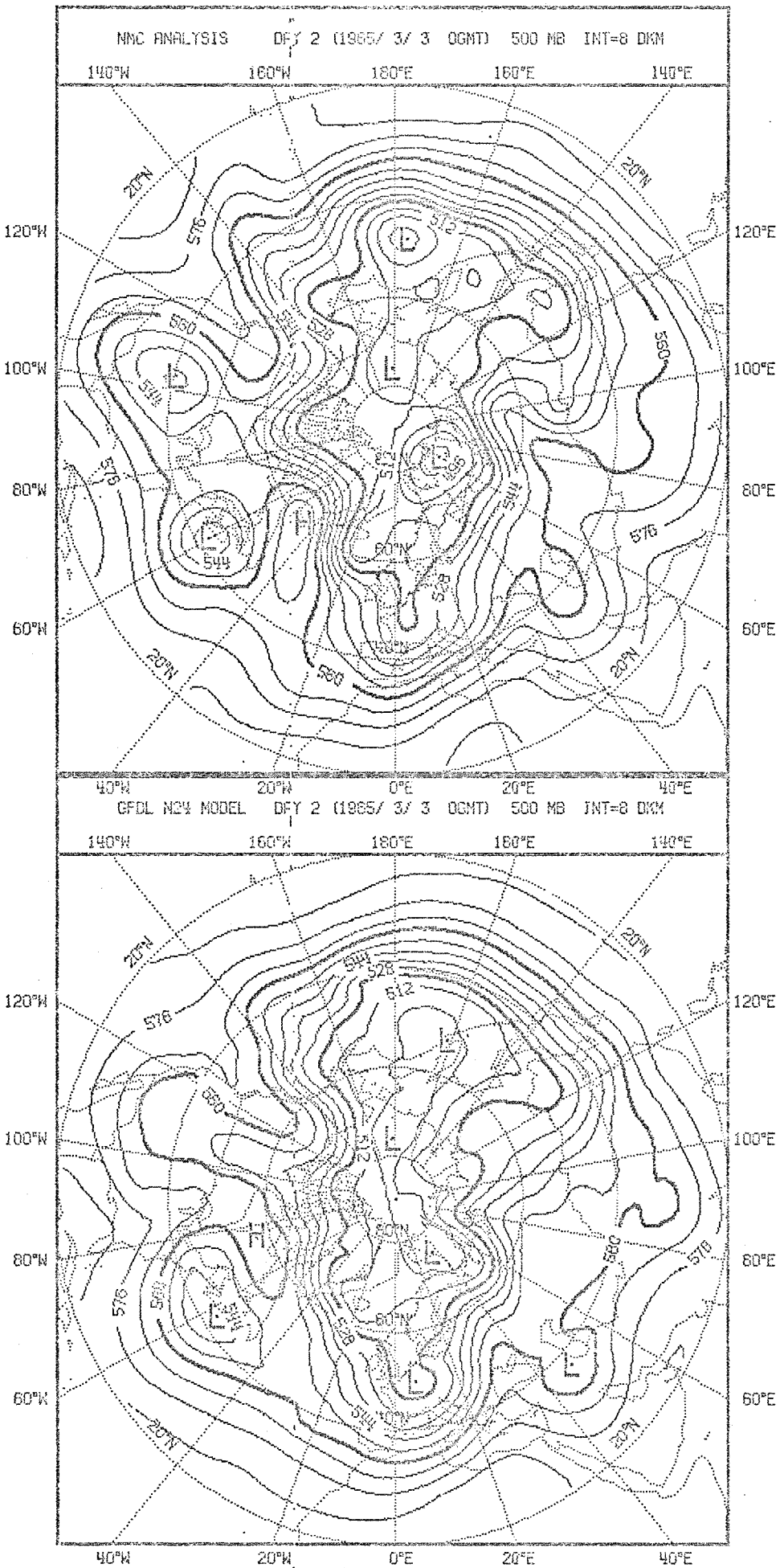
NMC ANALYSIS DFY 2 (1985/ 3/ 3 0GMT) 500 MB INT=8 DKM
140°W
160°W
180°E
160°E
140°E
120°W
100°W
80°W
60°W
120°E
100°E
80°E
60°E
40°W
20°W
0°E
20°E
40°E
20°N
80°N
544
552
560
568
576
584
592
GFDL N24 MODEL DFY 2 (1985/ 3/ 3 0GMT) 500 MB INT=8 DKM
512
528
536

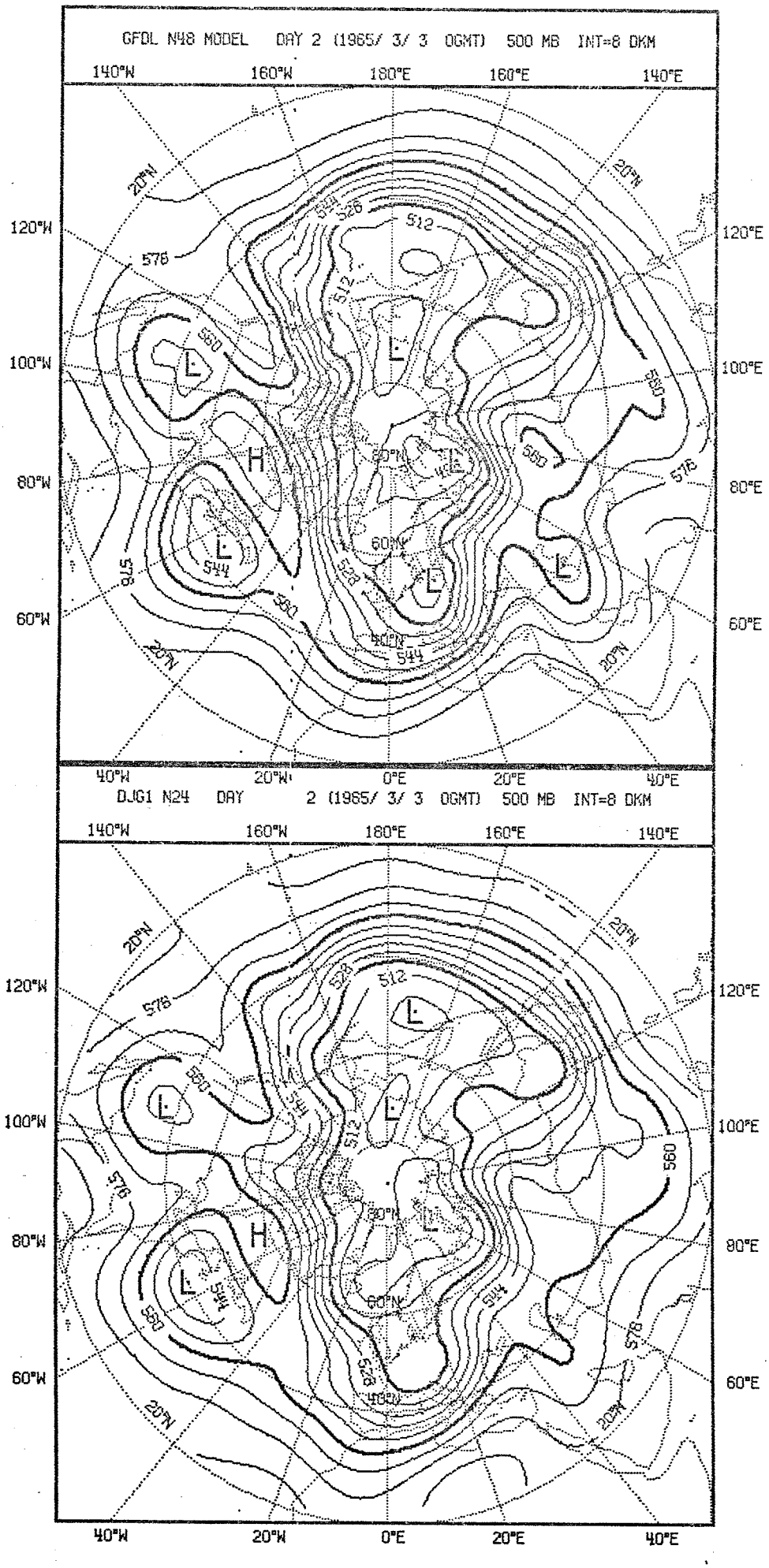

Fig. 3.1.3: Observed (top left) and predicted fields of 500 mb geopotential height, day 2.

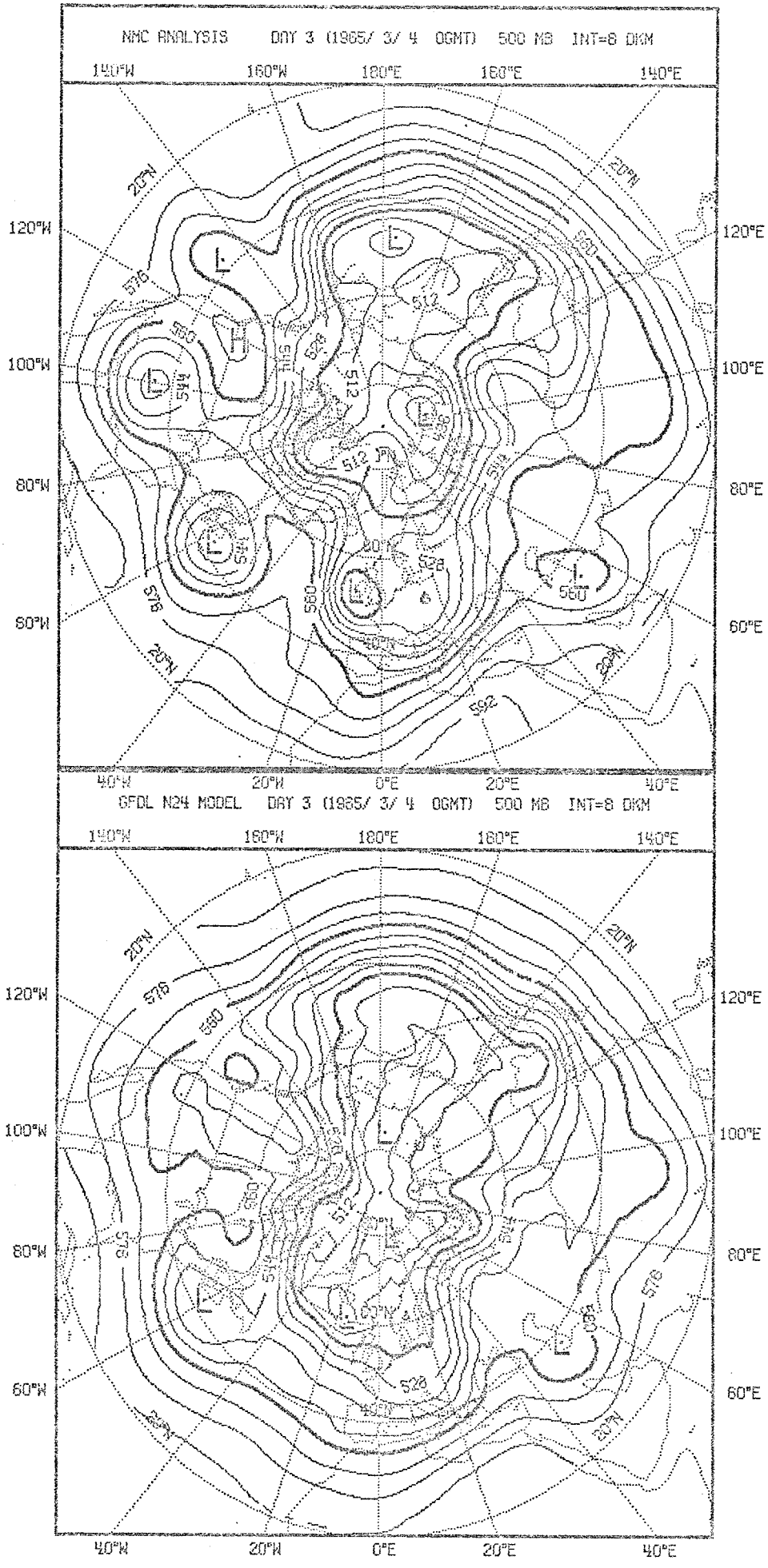
NMC ANALYSIS DAY 3 (1985/ 3/ 4 0GMT) 500 MB INT=8 DKM
140°W
160°W
180°E
160°E
140°E
120°W
100°W
80°W
60°W
120°E
100°E
80°E
60°E
20°N
40°W
20°W
0°E
20°E
40°E
GFDL N24 MODEL DAY 3 (1985/ 3/ 4 0GMT) 500 MB INT=8 DKM

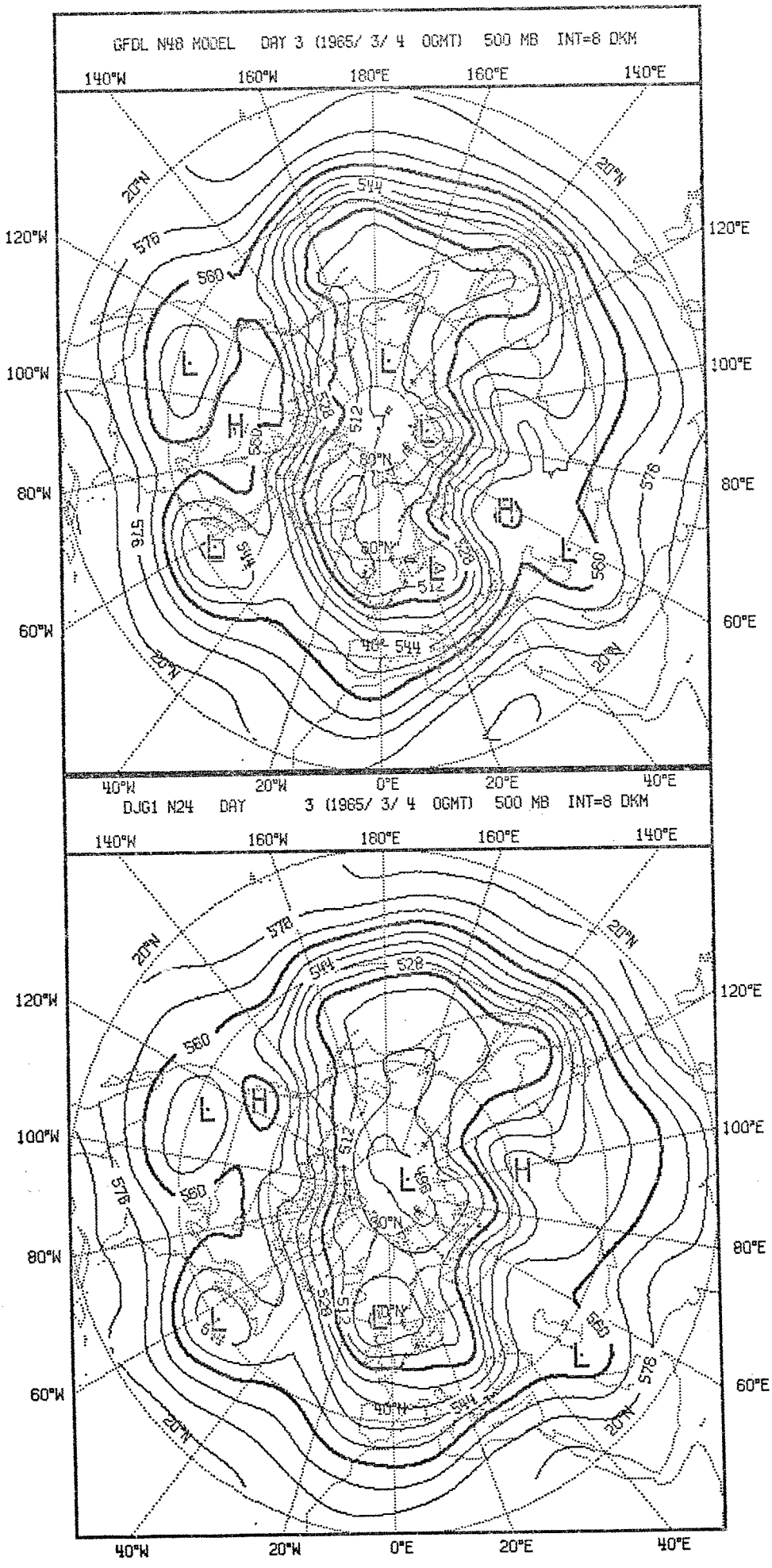

Fig. 3.1.4: Observed (top left) and predicted fields of 500 mb geopotential height, day 3.

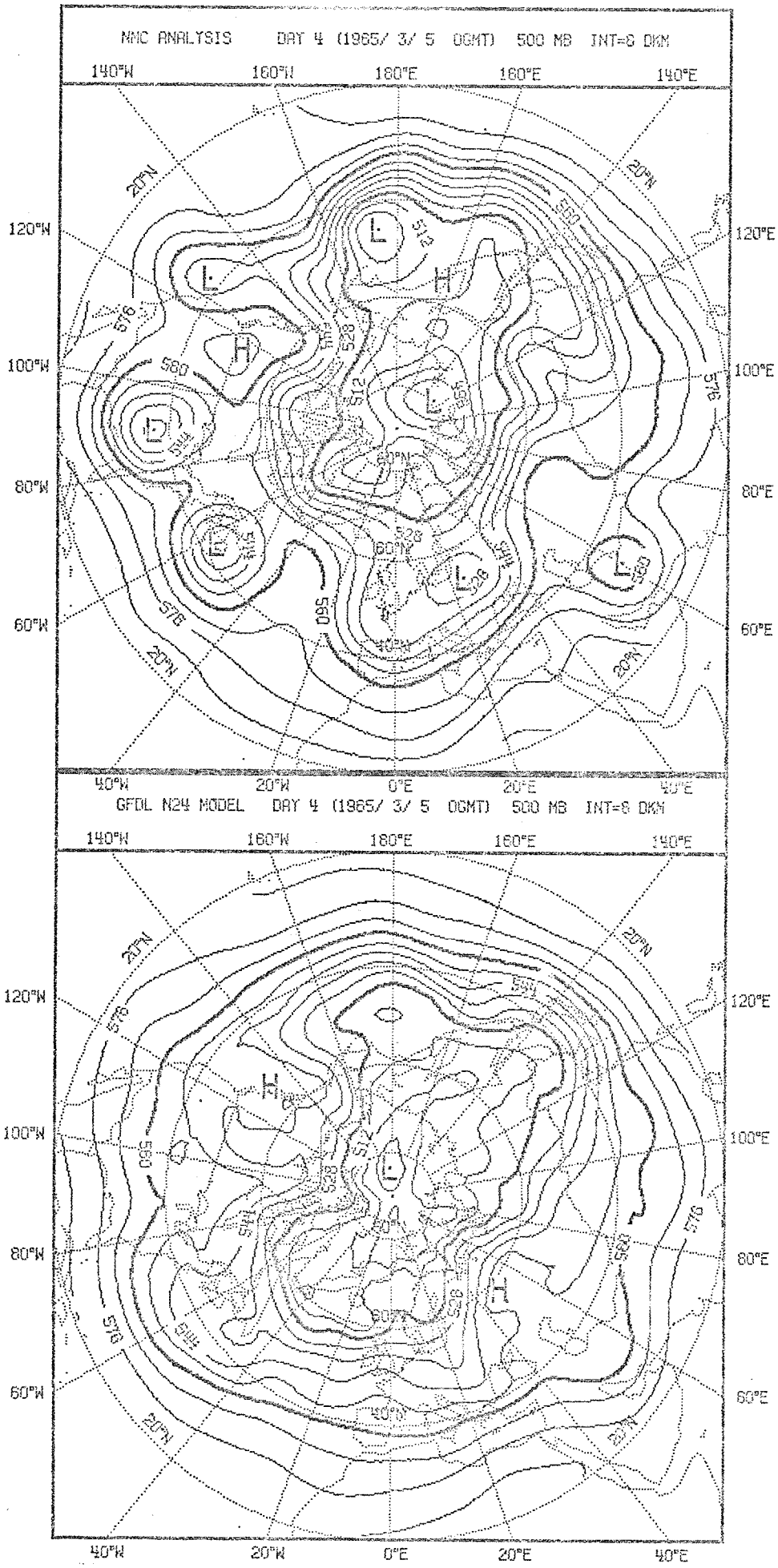
NMC ANALYSIS DAY 4 (1965/ 3/ 5 0GMT) 500 MB INT=8 DKM
140°W
160°W
180°E
160°E
140°E
120°W
100°W
80°W
60°W
120°E
100°E
80°E
60°E
20°N
40°W
20°W
0°E
20°E
40°E
GFDL N24 MODEL DAY 4 (1965/ 3/ 5 0GMT) 500 MB INT=8 DKM

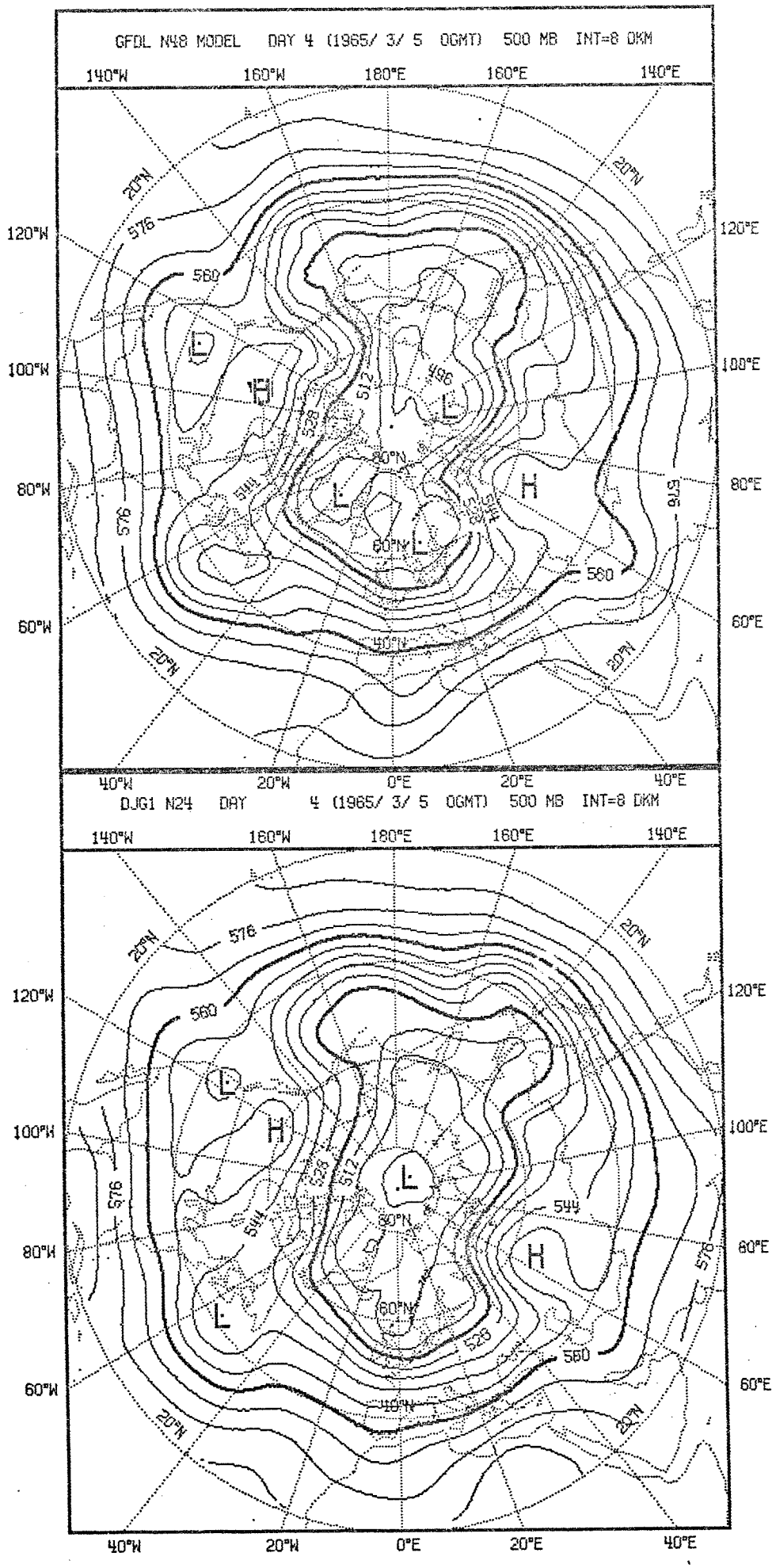

Fig. 3.1.5: Observed (top left) and predicted fields of 500 mb geopotential height, day 4.

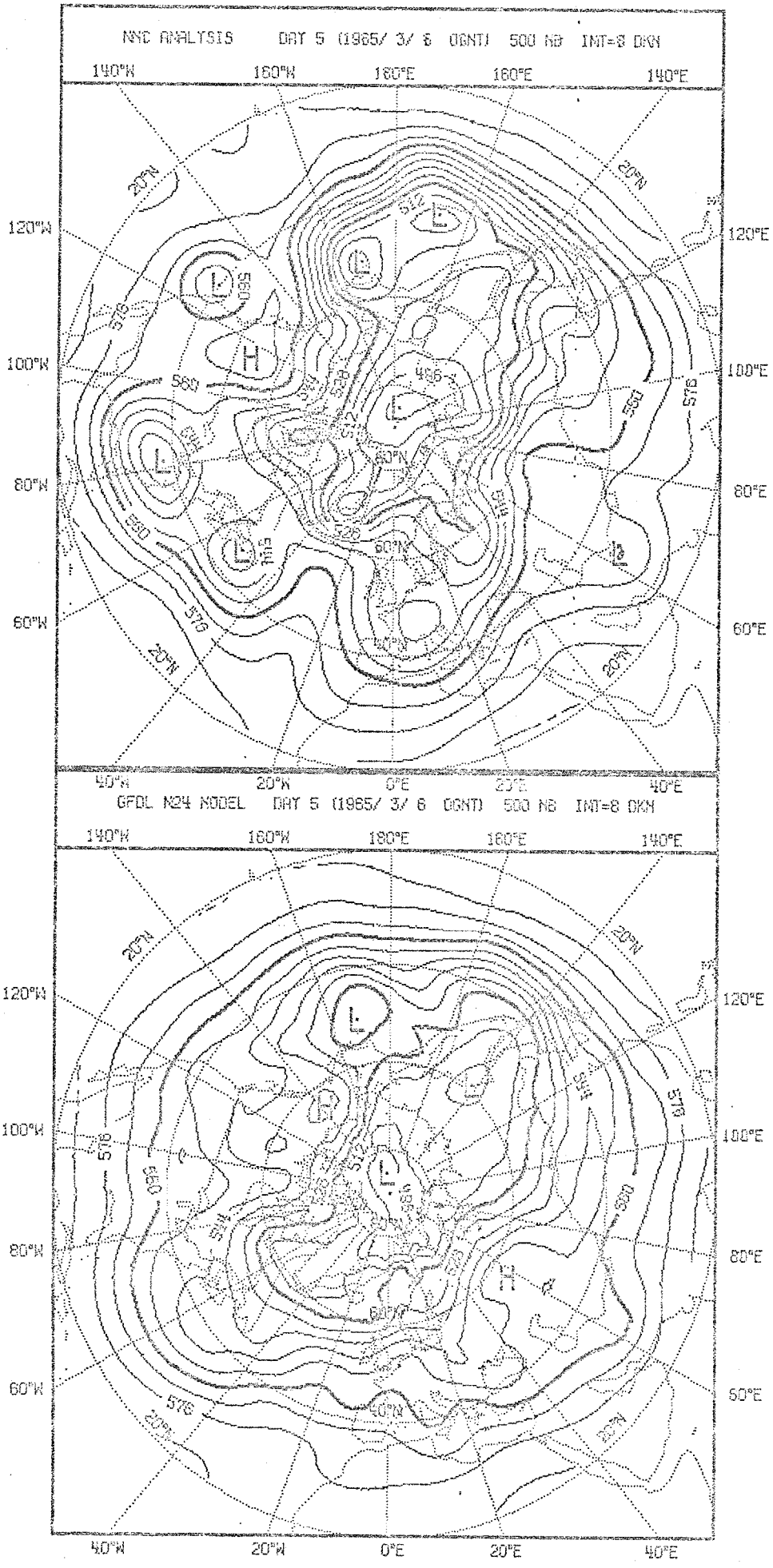
NMC ANALYSIS DAY 5 (1985/ 3/ 6 0GMT) 500 MB INT=8 DKM
140°W
160°W
180°E
160°E
140°E
120°W
120°E
100°W
100°E
80°W
80°E
60°W
60°E
40°W
20°W
0°E
20°E
40°E
20°N
60°N
H
L
576
580
584
588
592
GFDL N24 MODEL DAY 5 (1985/ 3/ 6 0GMT) 500 MB INT=8 DKM

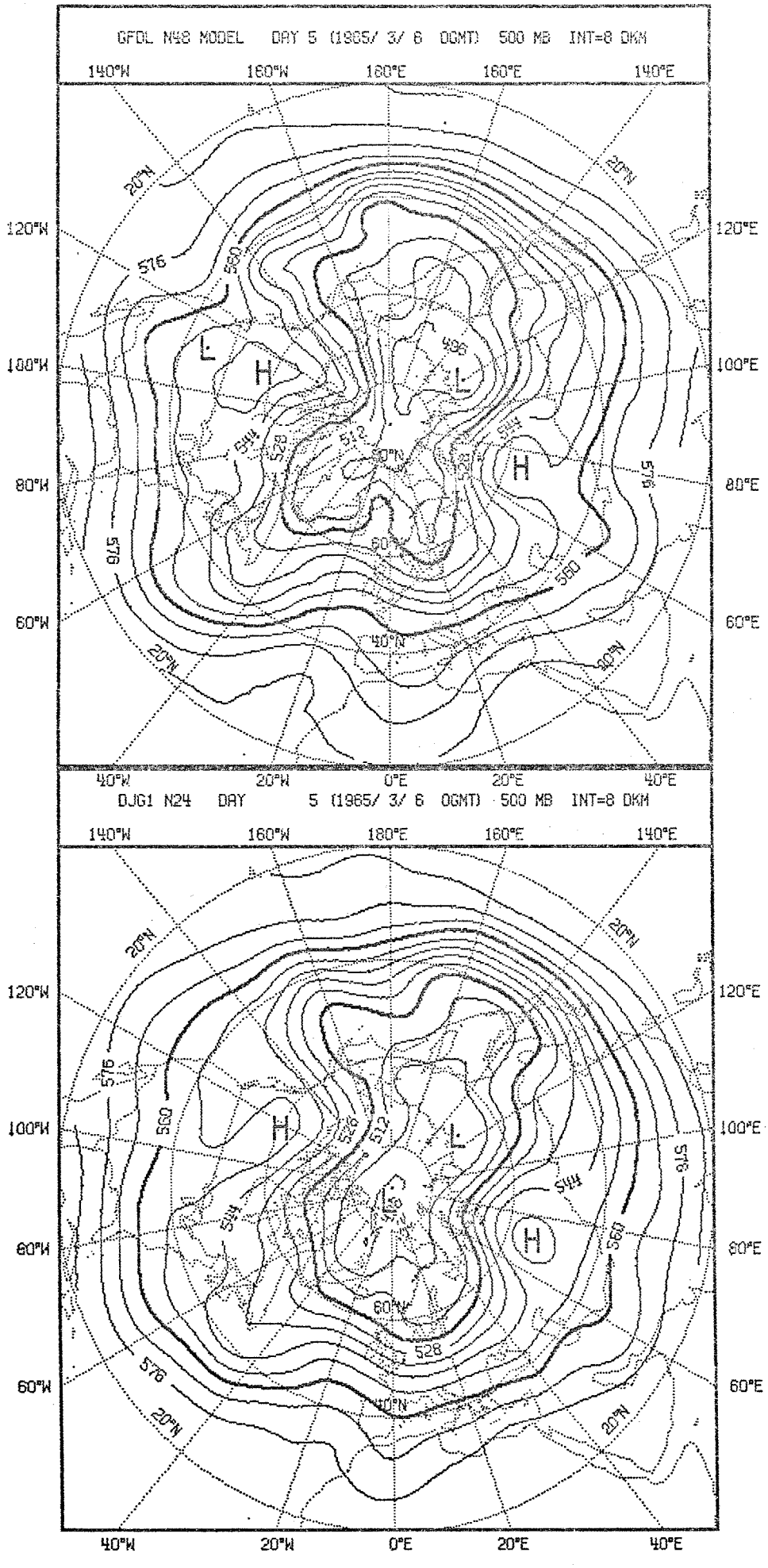

Fig. 3.1.6: Observed (top left) and predicted fields of 500 mb geopotential height, day 5.

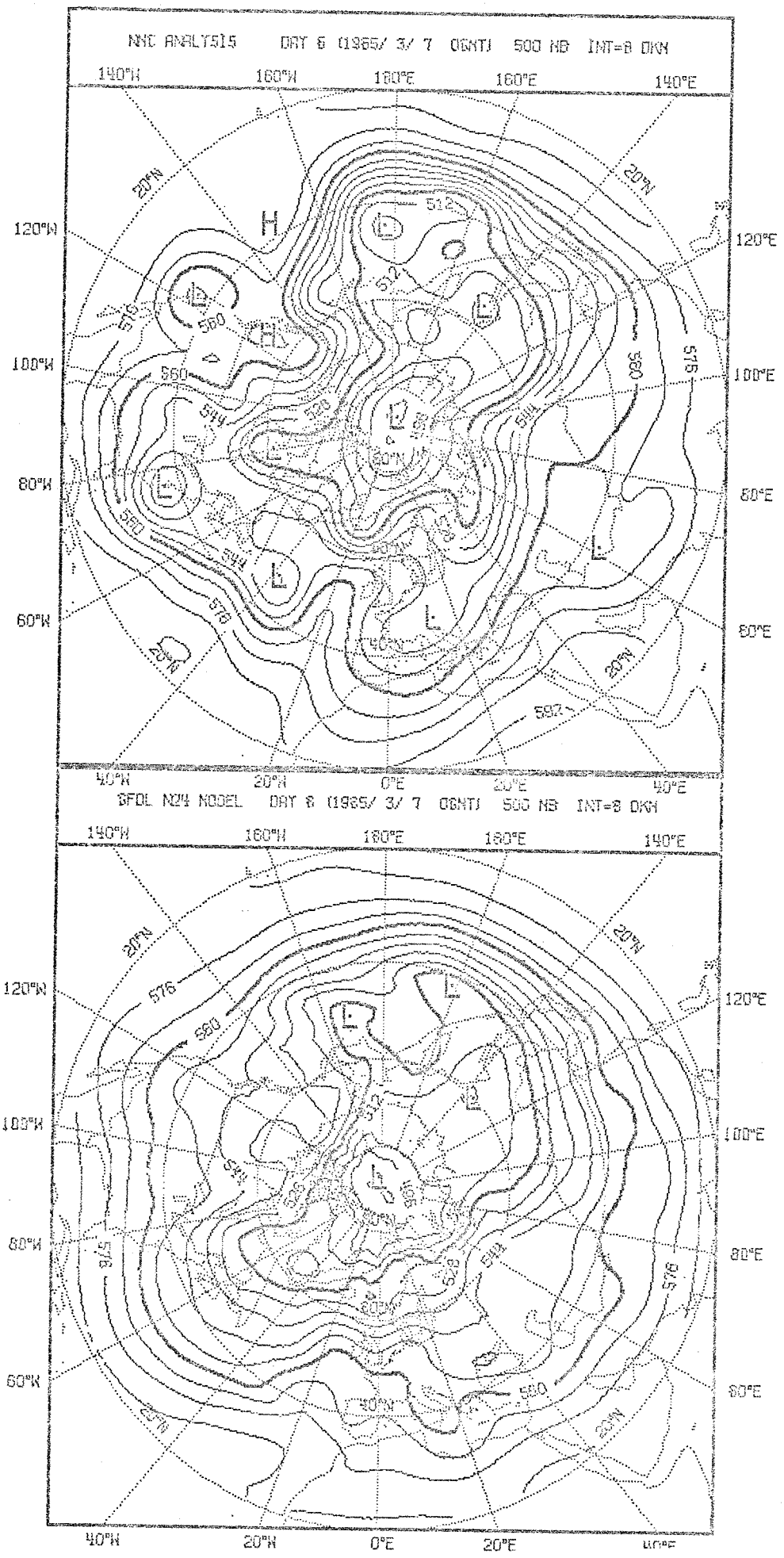
NMC ANALYSIS DAY 6 (1985/ 3/ 7 00GMT) 500 MB INT=8 DAM
140°W
160°W
180°E
160°E
140°E
20°N
120°W
120°E
100°W
100°E
80°W
80°E
60°W
60°E
40°N
20°N
0°E
20°E
40°E
H
L
512
516
520
524
528
532
536
540
544
548
552
556
560
564
568
572
576
580
584
588
592
596
NGFDL N24 MODEL DAY 6 (1985/ 3/ 7 00GMT) 500 MB INT=8 DAM
140°W
160°W
180°E
160°E
140°E
20°N
120°W
120°E
100°W
100°E
80°W
80°E
60°W
60°E
40°N
20°N
0°E
20°E
L
540
544
548
552
556
560
564
568
572
576
580
584
588
592
596

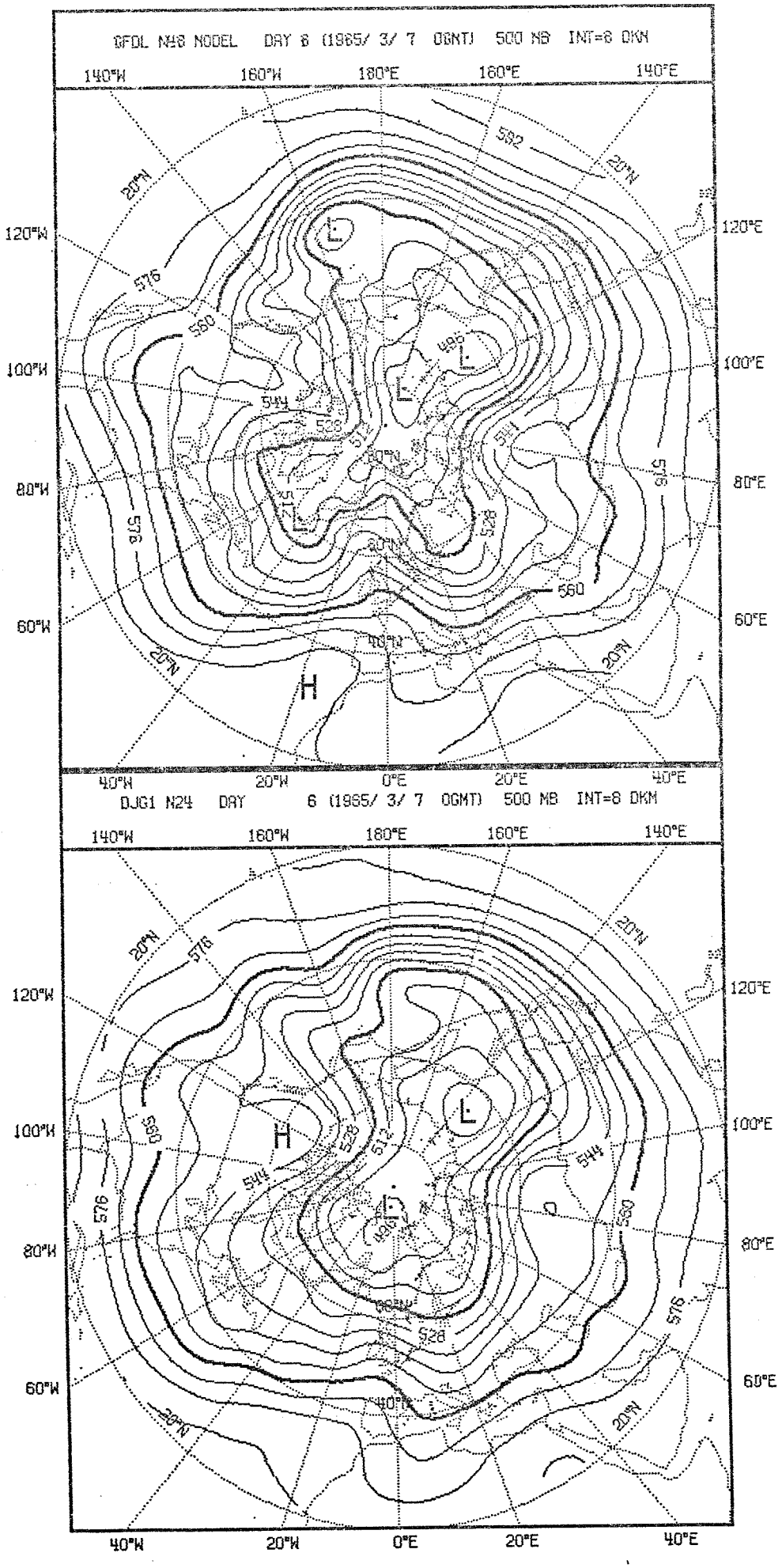

Fig. 3.1.7: Observed (top left) and predicted fields of 500 mb geopotential height, day 6.

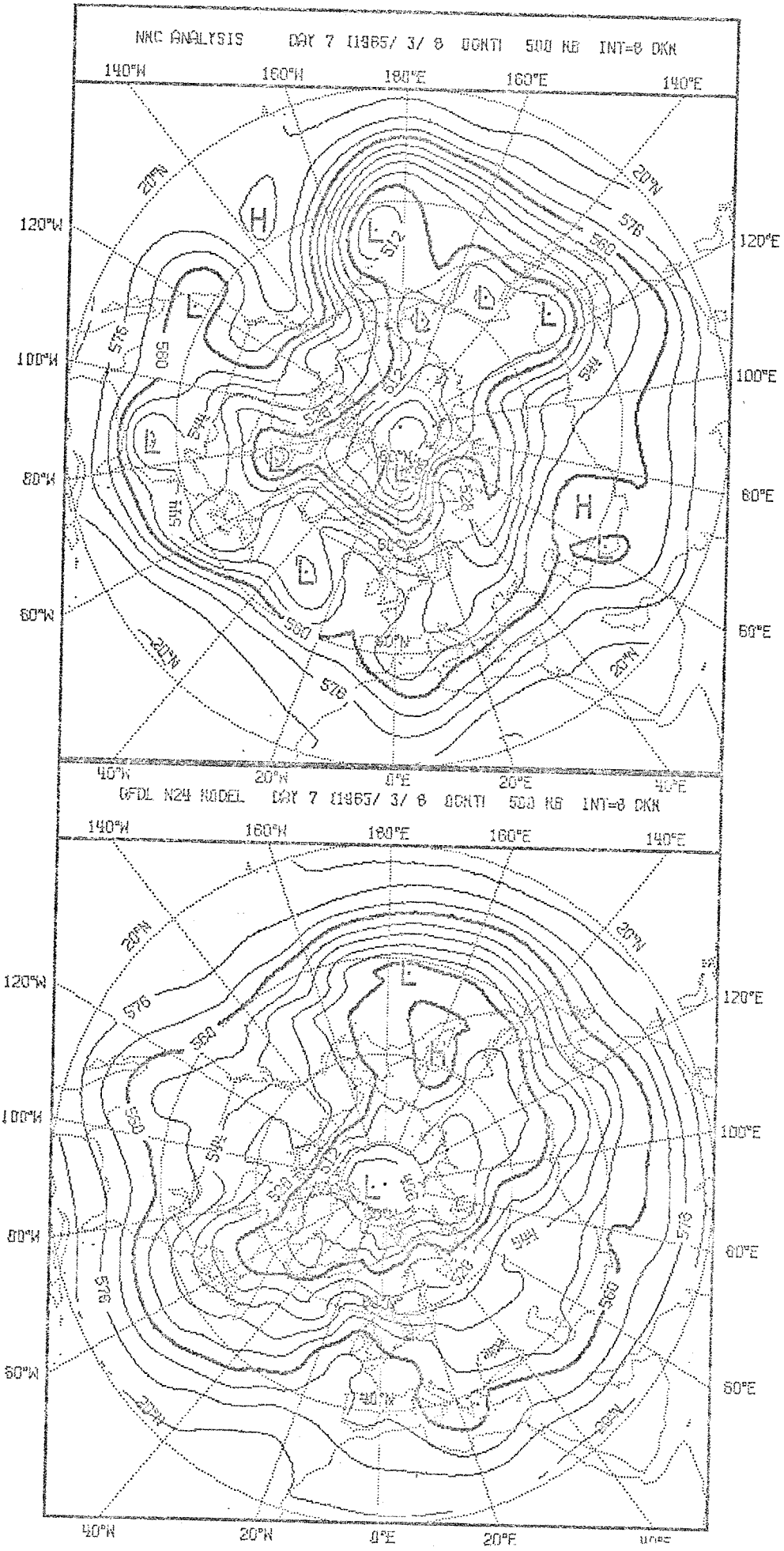
NMC ANALYSIS DAY 7 [1985/ 3/ 6 0GMT 500 MB INT=6 DKM
140°W
160°W
180°E
160°E
140°E
120°W
100°W
80°W
60°W
120°E
100°E
80°E
60°E
40°N
20°N
0°E
20°E
40°E
H
L
576
564
552
540
528
516
504
492
480
GFDL N24 MODEL DAY 7 [1985/ 3/ 6 0GMT 500 MB INT=6 DKM

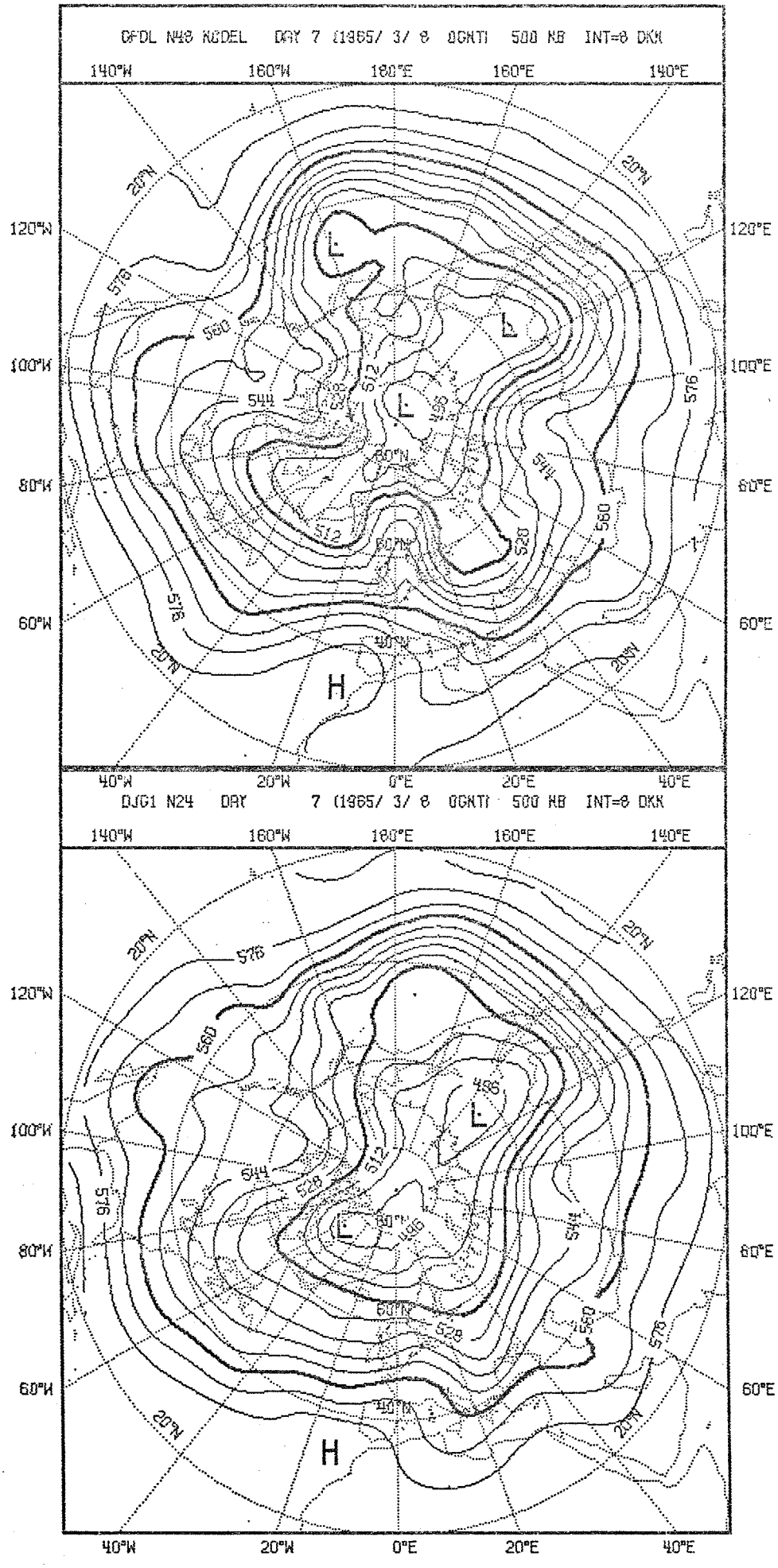

Fig. 3.1.8: Observed (top left) and predicted fields of 500 mb geopotential height, day 7.

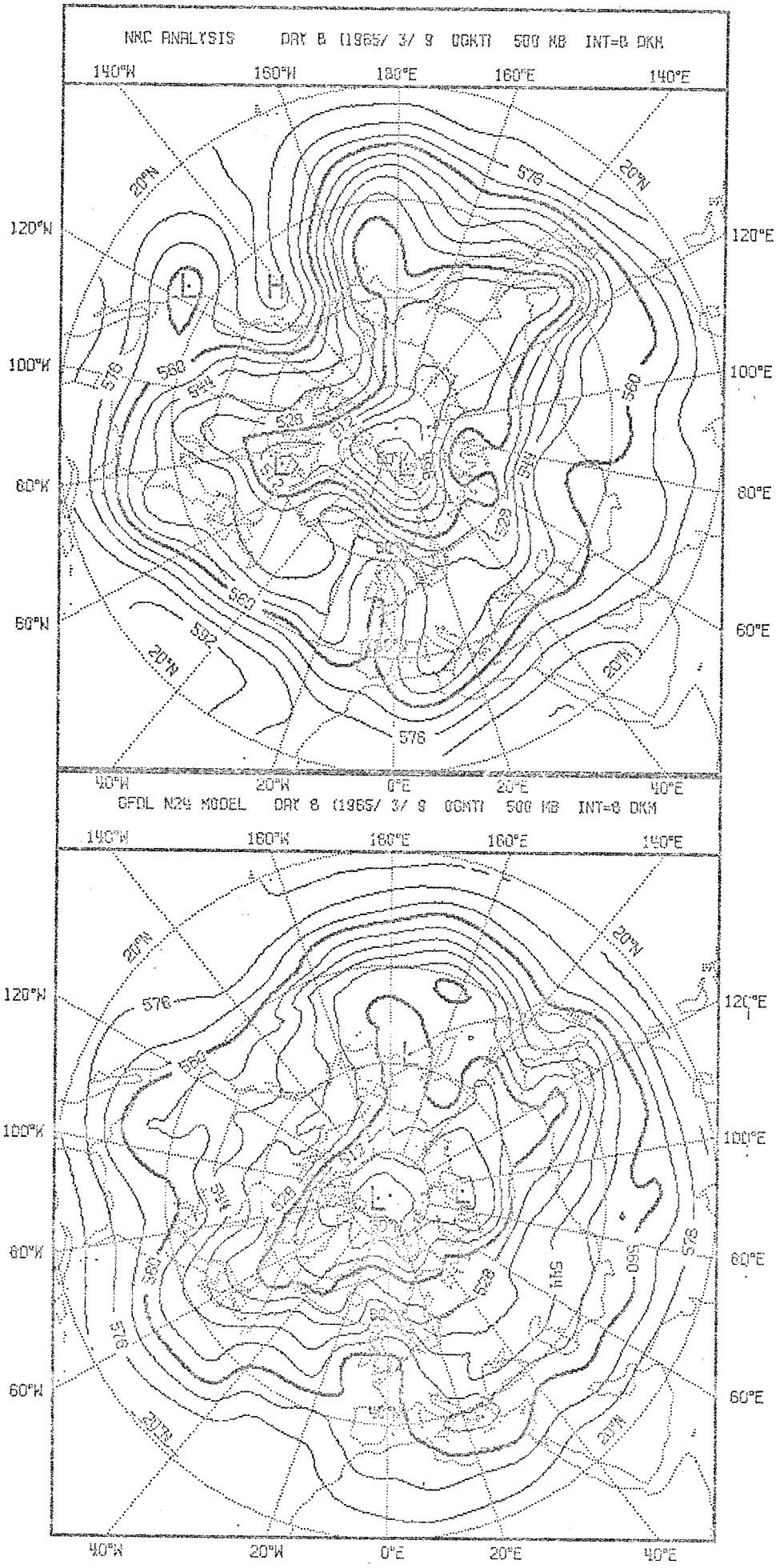
NMC ANALYSIS DAY 8 (1985/ 3/ 9 00GMT 500 MB INT=8 DAM
140°W
160°W
180°E
160°E
140°E
120°W
100°W
80°W
60°W
120°E
100°E
80°E
60°E
40°W
20°W
0°E
20°E
40°E
20°N
576
552
528
504
560
592
588
584
580
564
568
572
GFDL N24 MODEL DAY 8 (1985/ 3/ 9 00GMT 500 MB INT=8 DAM
140°W
160°W
180°E
160°E
140°E
120°W
100°W
80°W
60°W
120°E
100°E
80°E
60°E
40°W
20°W
0°E
20°E
40°E
20°N
576
552
528
504
560
592
588
584
580
564
568
572

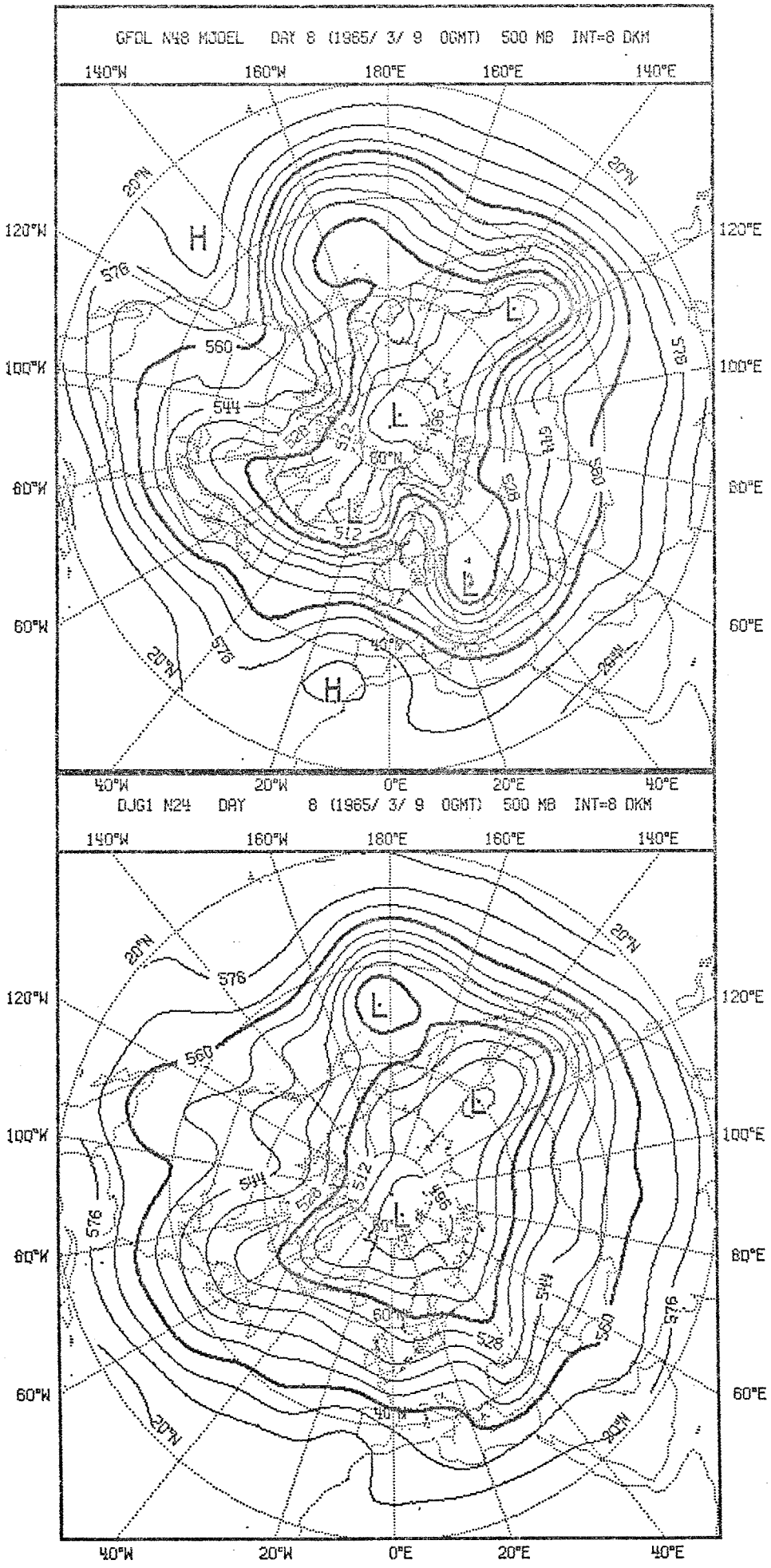

Fig. 3.1.9: Observed (top left) and predicted fields of 500 mb geopotential height, day 8.

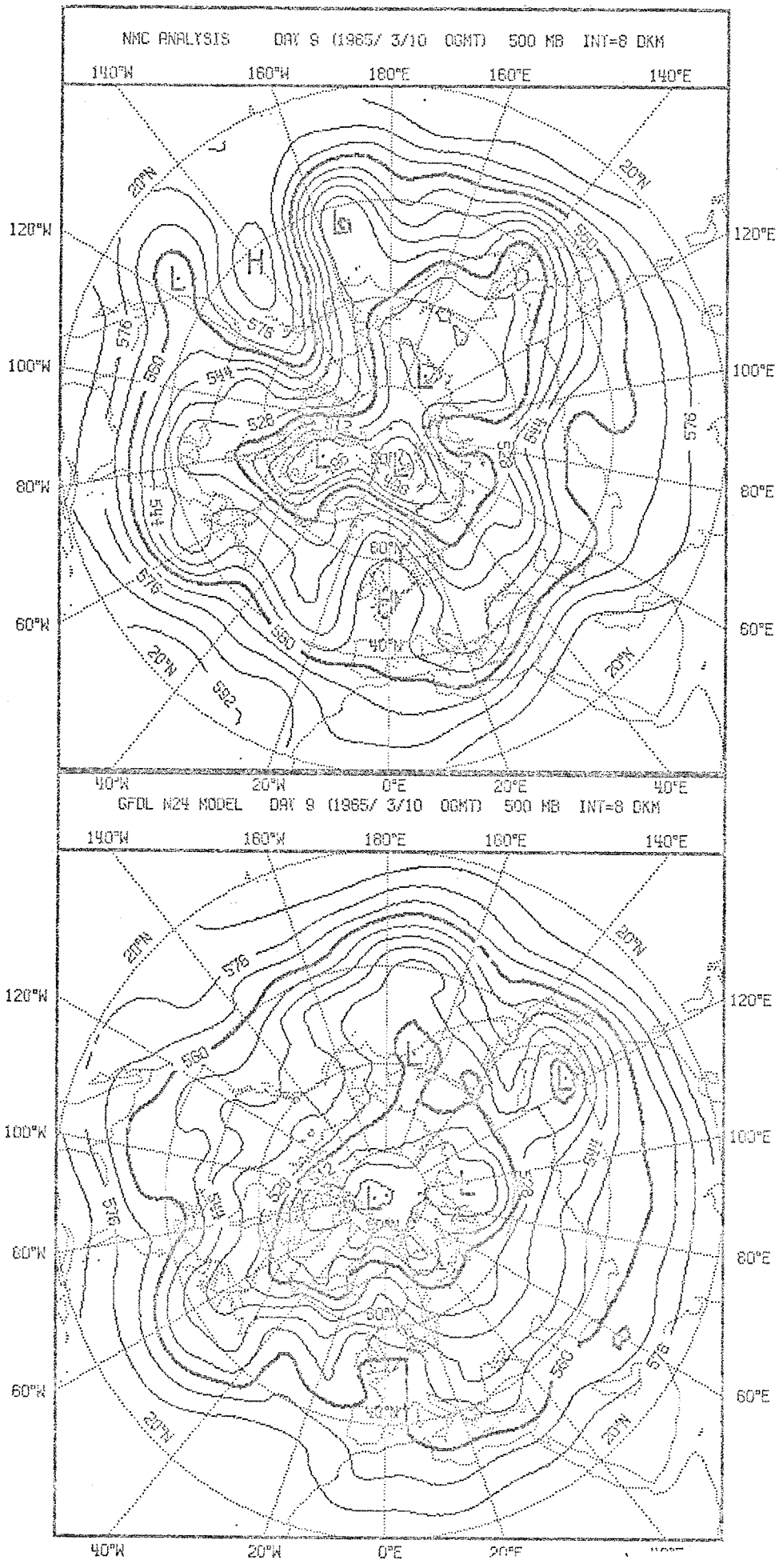
NMC ANALYSIS DAY 9 (1985/ 3/10 00GMT) 500 MB INT=8 DKM
140°W
160°W
180°E
160°E
140°E
120°W
120°E
100°W
100°E
80°W
80°E
60°W
60°E
40°W
20°W
0°E
20°E
40°E
20°N
40°N
60°N
576
550
544
528
592
GFDL N24 MODEL DAY 9 (1985/ 3/10 00GMT) 500 MB INT=8 DKM
140°W
160°W
180°E
160°E
140°E
120°W
120°E
100°W
100°E
80°W
80°E
60°W
60°E
40°W
20°W
0°E
20°E
20°N
40°N
60°N
576
560
544
528

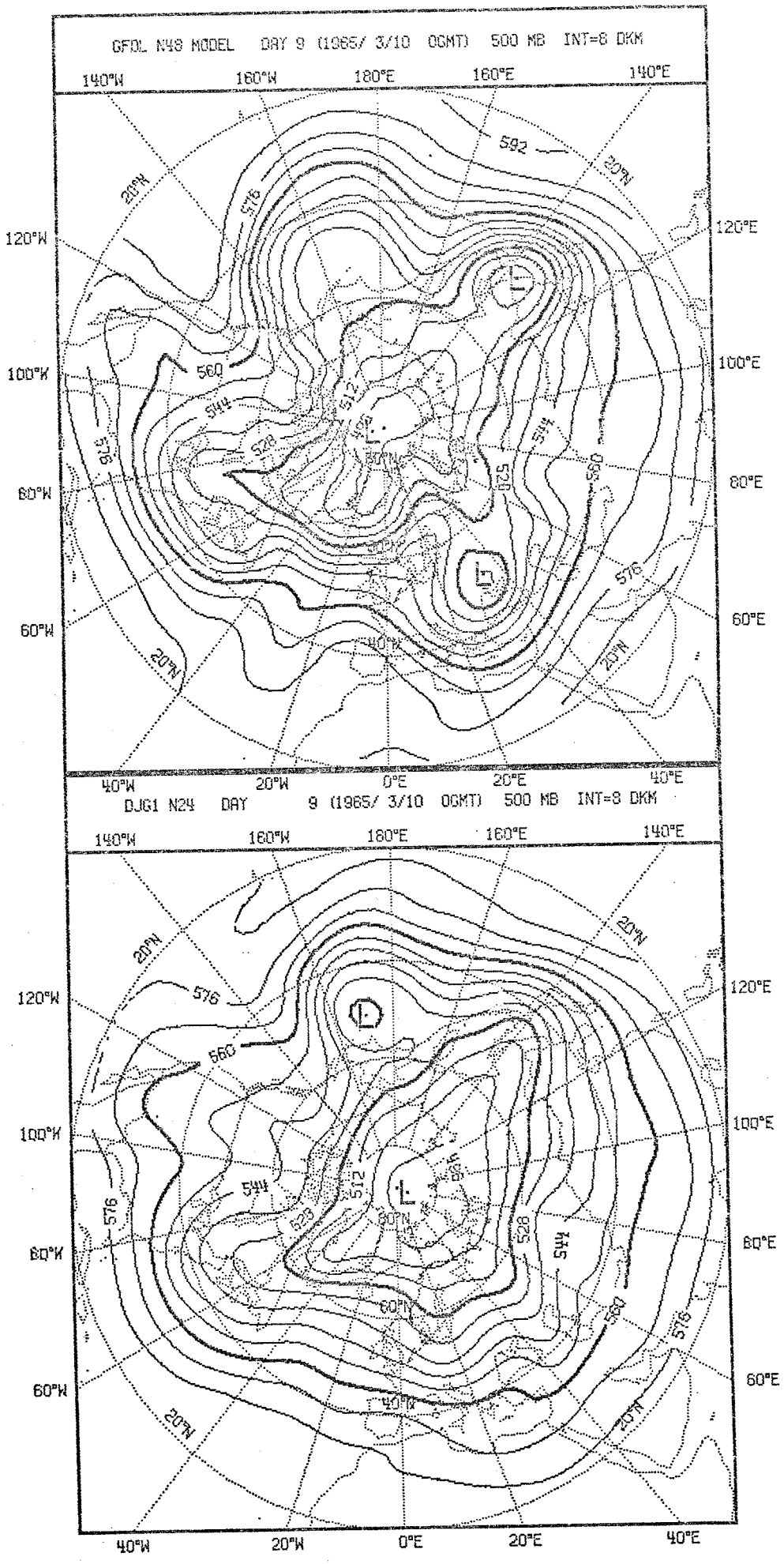

Fig. 3.1.10: Observed (top left) and predicted fields of 500 mb geopotential height, day 9.

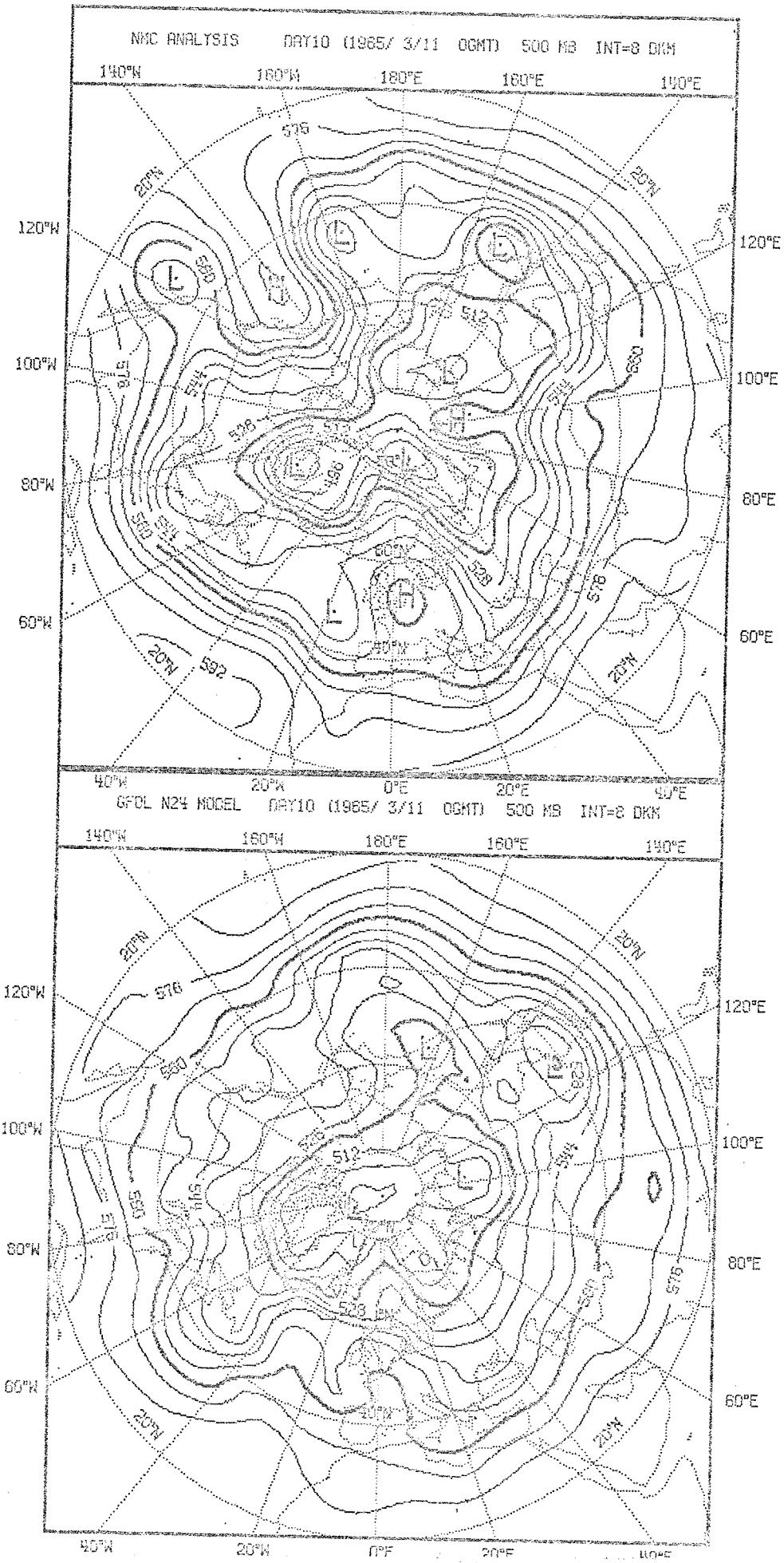
NMC ANALYSIS DAY10 (1965/ 3/11 0GMT) 500 MB INT=8 DKM
140°W
160°W
180°
160°E
140°E
120°W
100°W
80°W
60°W
120°E
100°E
80°E
60°E
40°W
20°W
0°E
20°E
40°E
20°N
576
592
GFDL N24 MODEL DAY10 (1965/ 3/11 0GMT) 500 MB INT=8 DKM

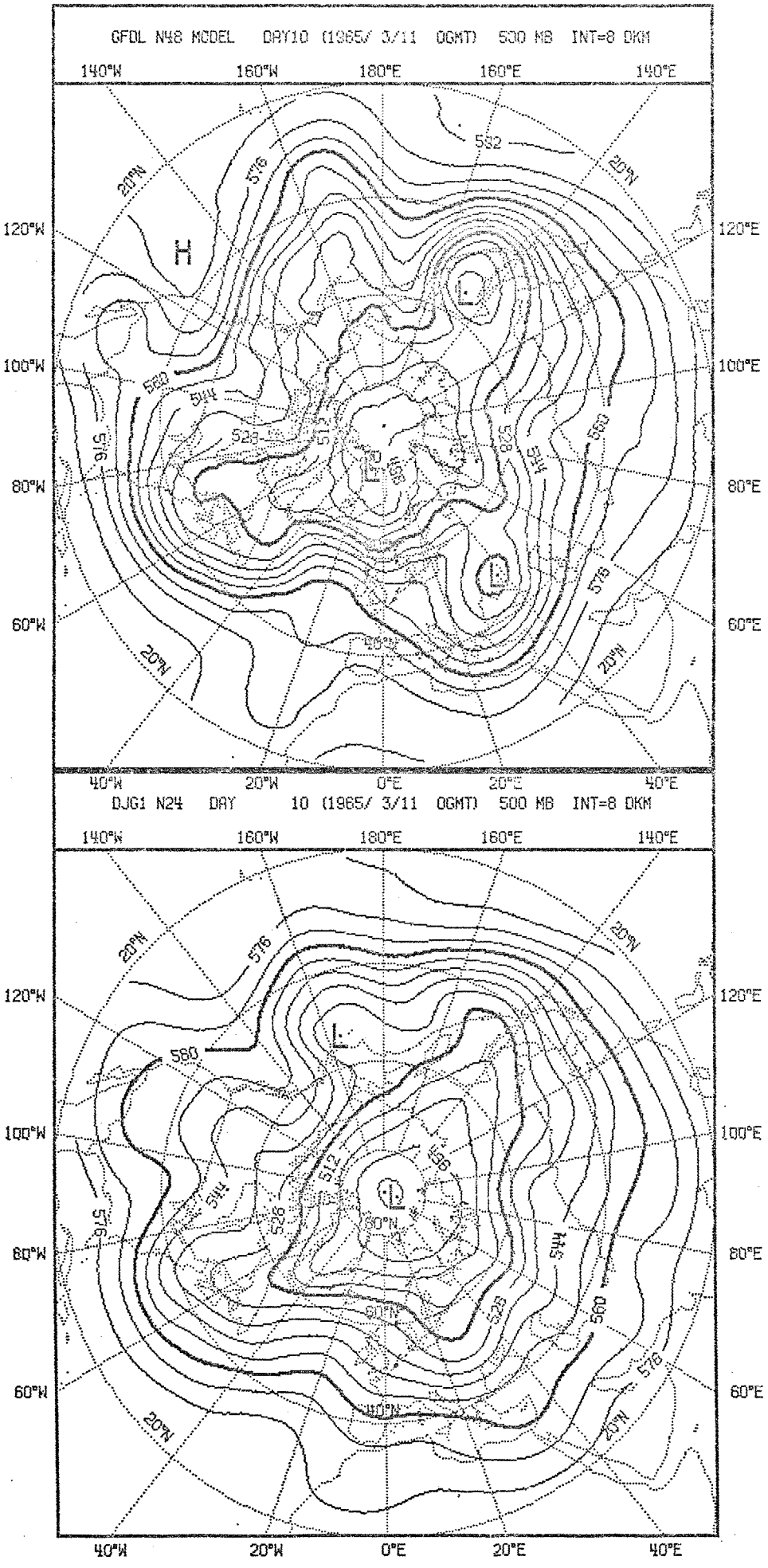

Fig. 3.1.11: Observed (top left) and predicted fields of 500 mb geopotential height, day 10.

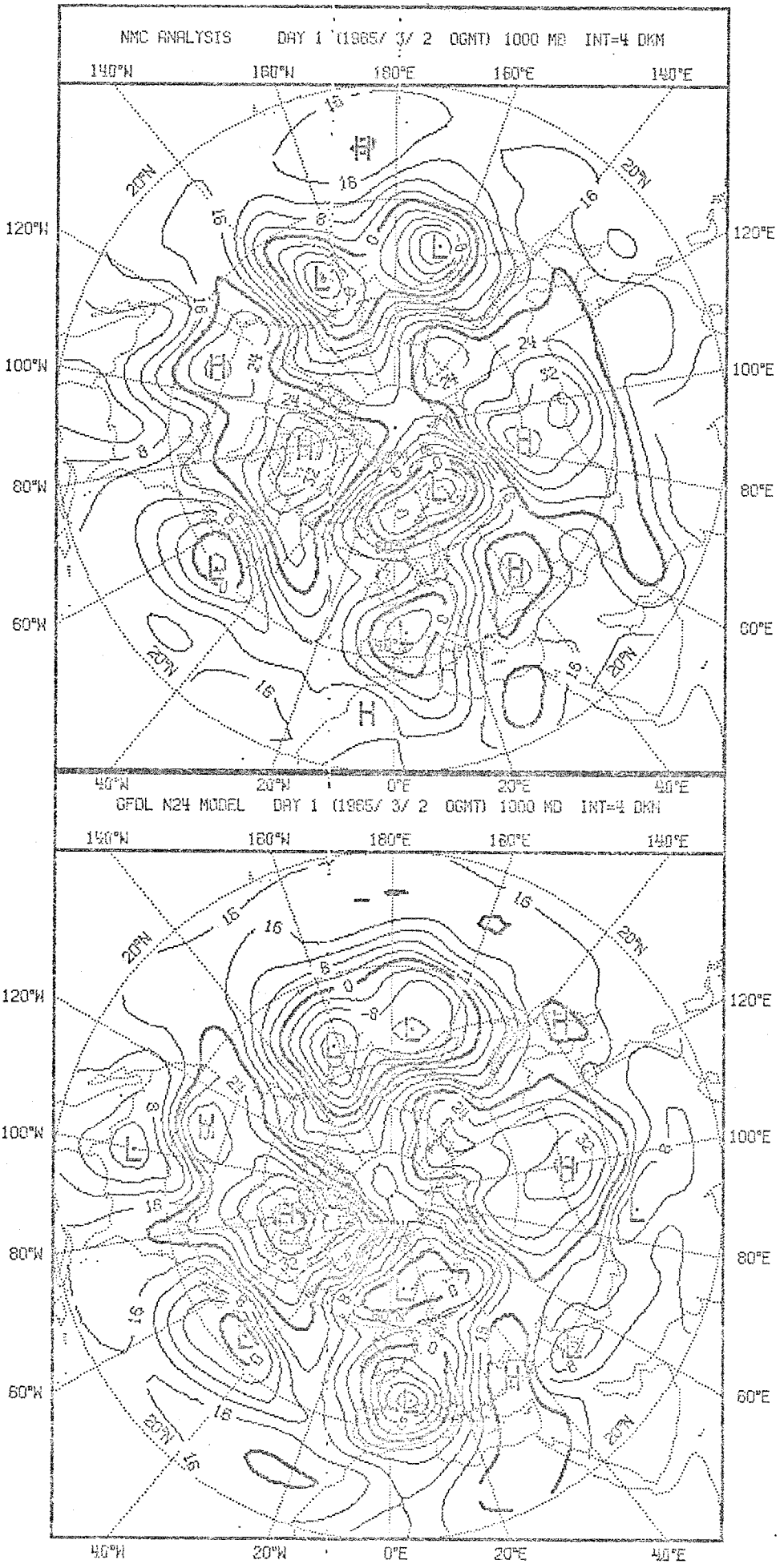
NMC ANALYSIS DAY 1 (1985/ 3/ 2 00GMT) 1000 MB INT=4 DKM
140°W
160°W
180°E
160°E
140°E
120°W
120°E
100°W
100°E
80°W
80°E
60°W
60°E
40°W
20°W
0°E
20°E
40°E
GFDL N24 MODEL DAY 1 (1985/ 3/ 2 00GMT) 1000 MB INT=4 DKM

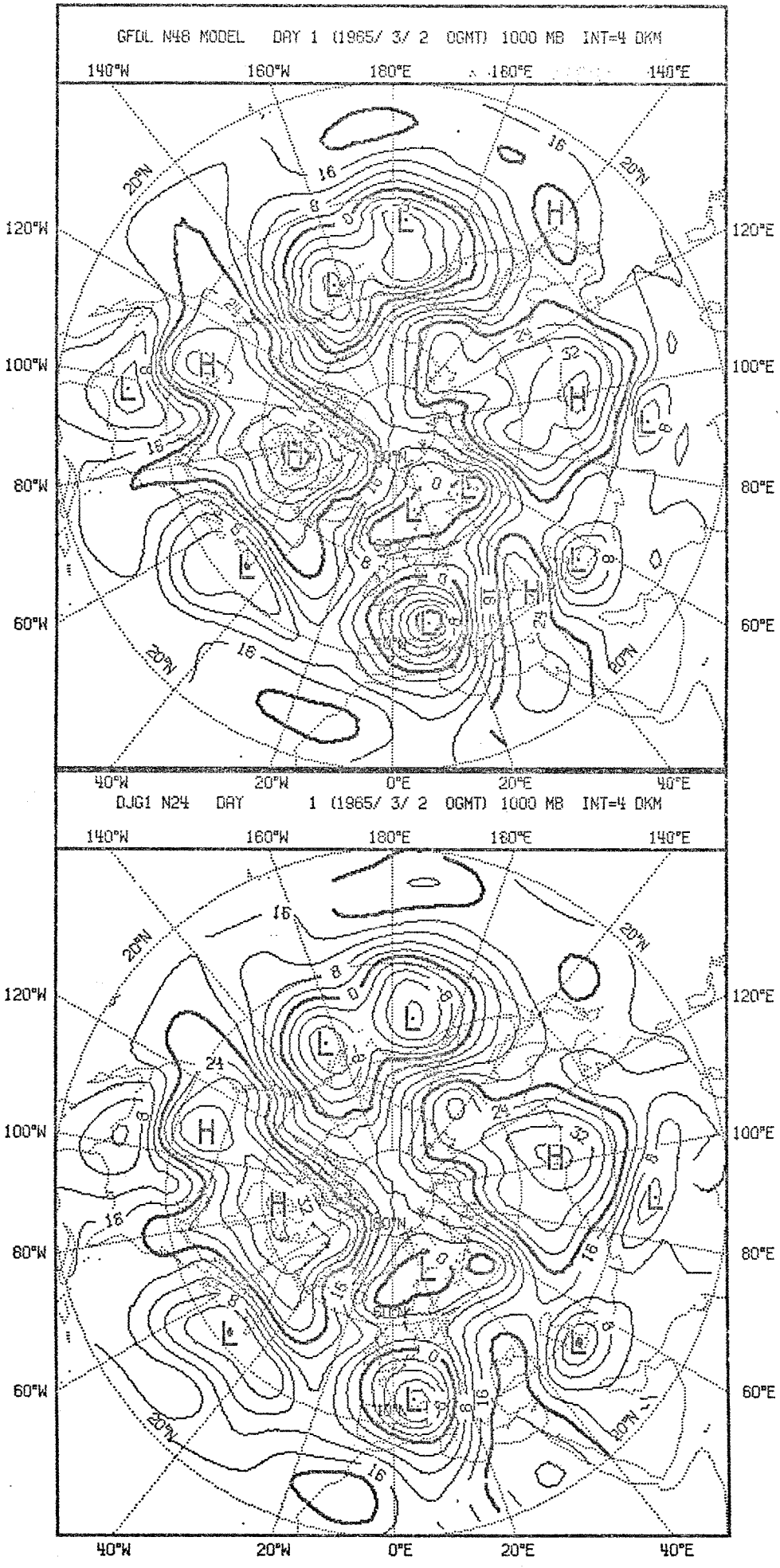

Fig. 3.1.12: Observed (top left) and predicted fields of 1000 mb geopotential height, day 1.

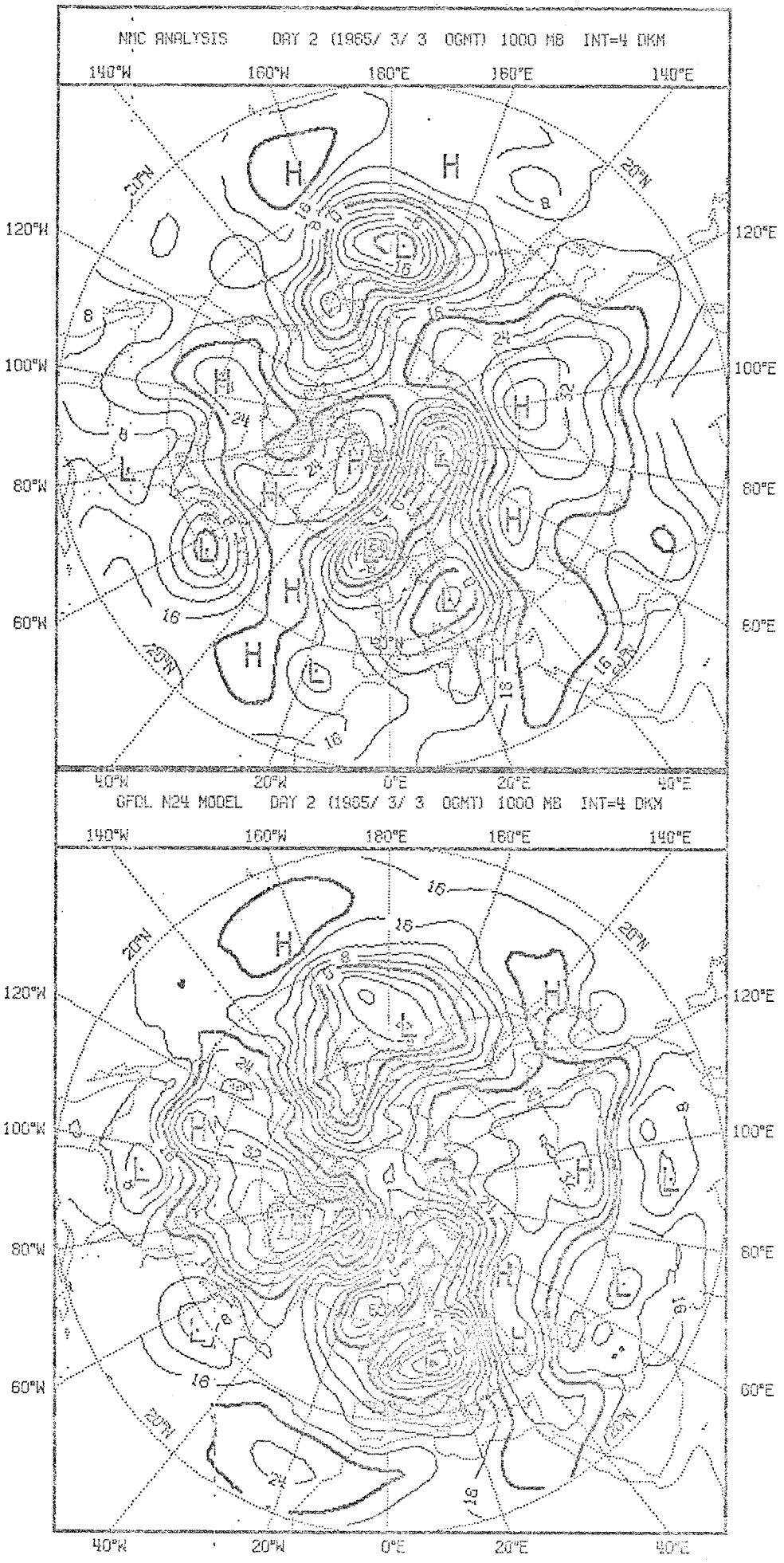
NMC ANALYSIS DAY 2 (1985/ 3/ 3 00GMT) 1000 MB INT=4 DKM
140°W
160°W
180°E
160°E
140°E
120°W
100°W
80°W
60°W
120°E
100°E
80°E
60°E
20°N
40°W
20°W
0°E
20°E
40°E
GFDL N24 MODEL DAY 2 (1985/ 3/ 3 00GMT) 1000 MB INT=4 DKM

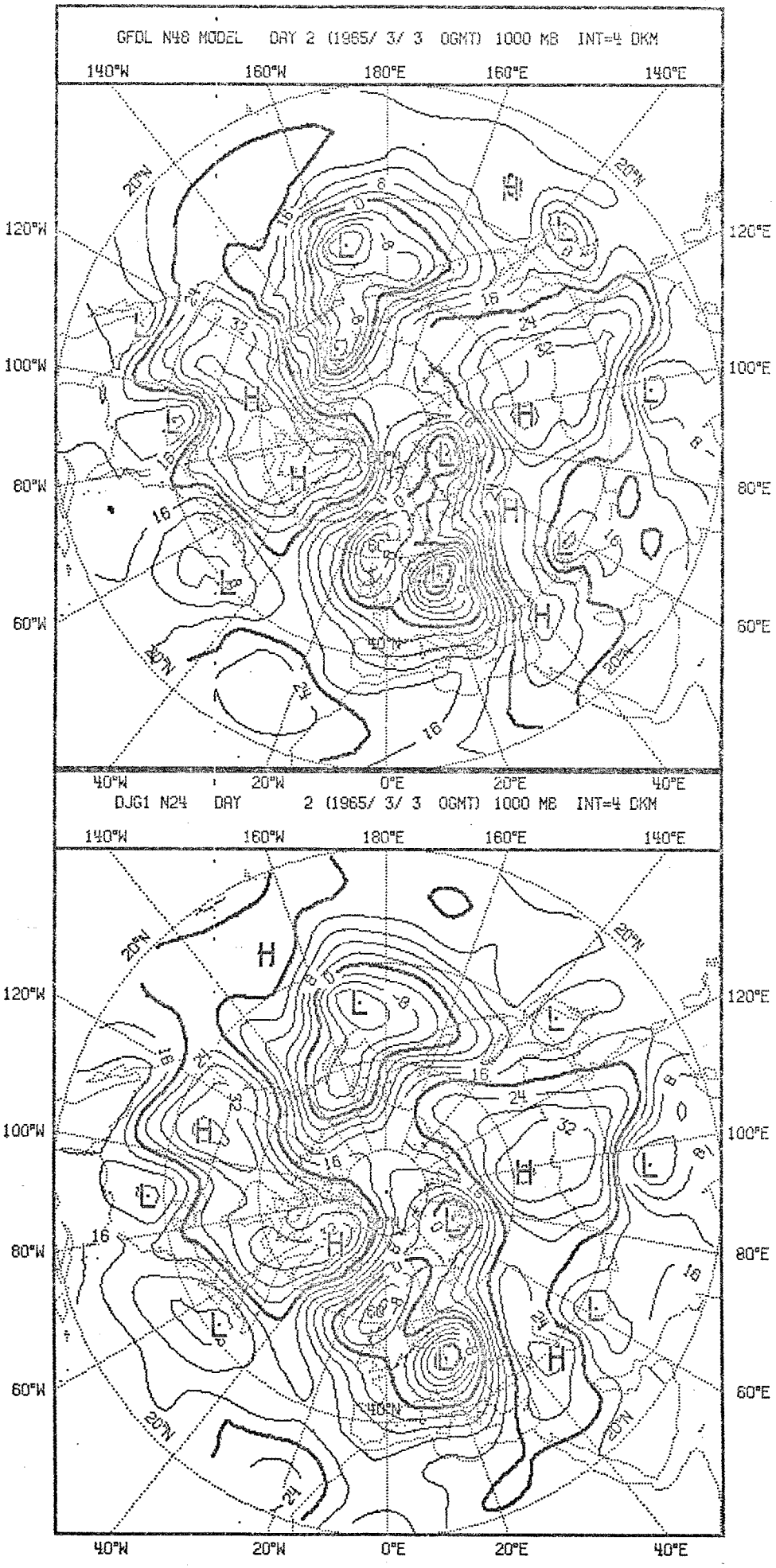

Fig. 3.1.13: Observed (top left) and predicted fields of 1000 mb geopotential height, day 2.

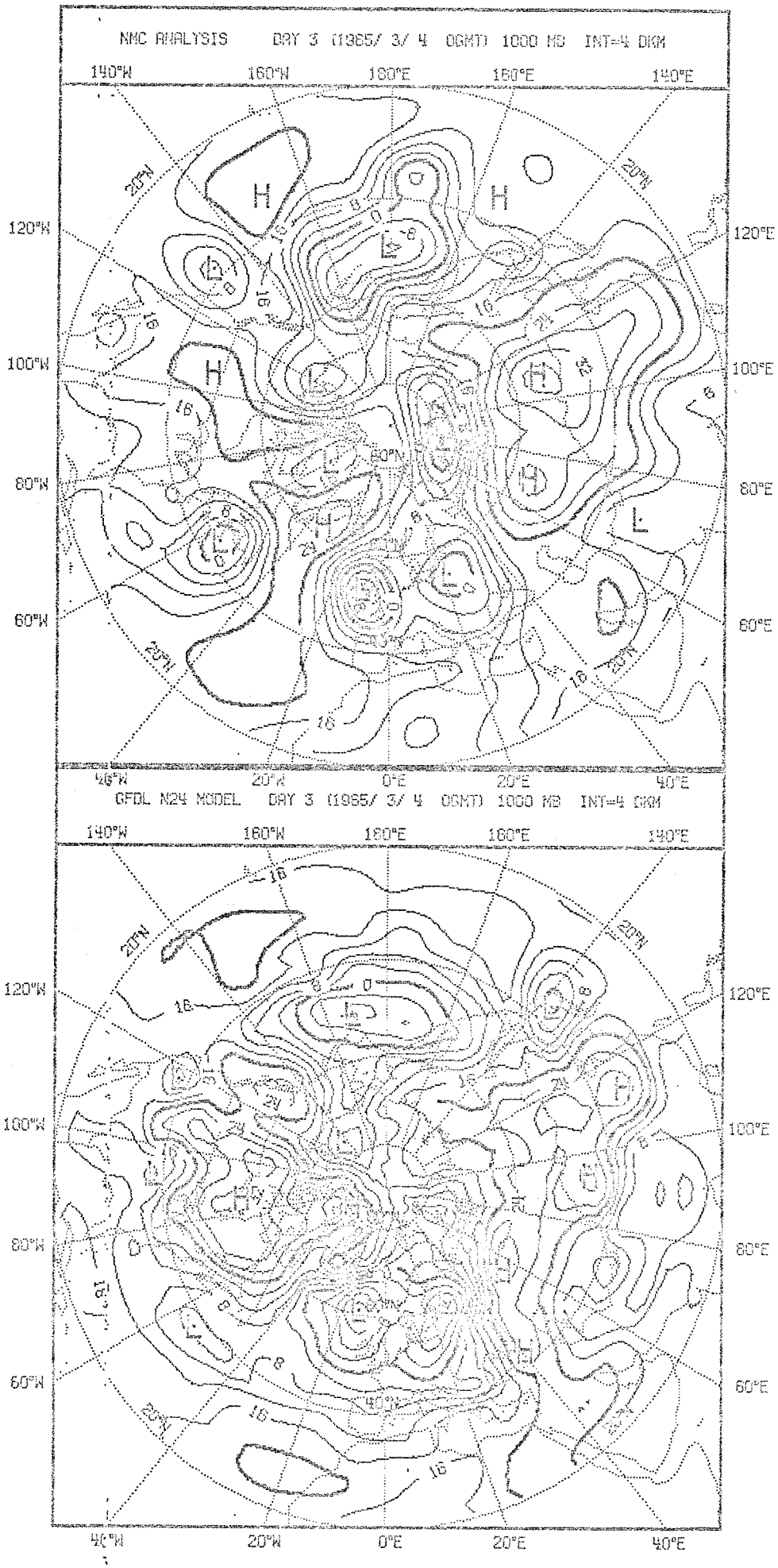
NMC ANALYSIS DAY 3 (1985/ 3/ 4 00GMT) 1000 MB INT=4 DKM
140°W
160°W
180°E
160°E
140°E
120°W
120°E
100°W
100°E
80°W
80°E
60°W
60°E
40°W
20°W
0°E
20°E
40°E
20°N
80°N
GFDL N24 MODEL DAY 3 (1985/ 3/ 4 00GMT) 1000 MB INT=4 DKM

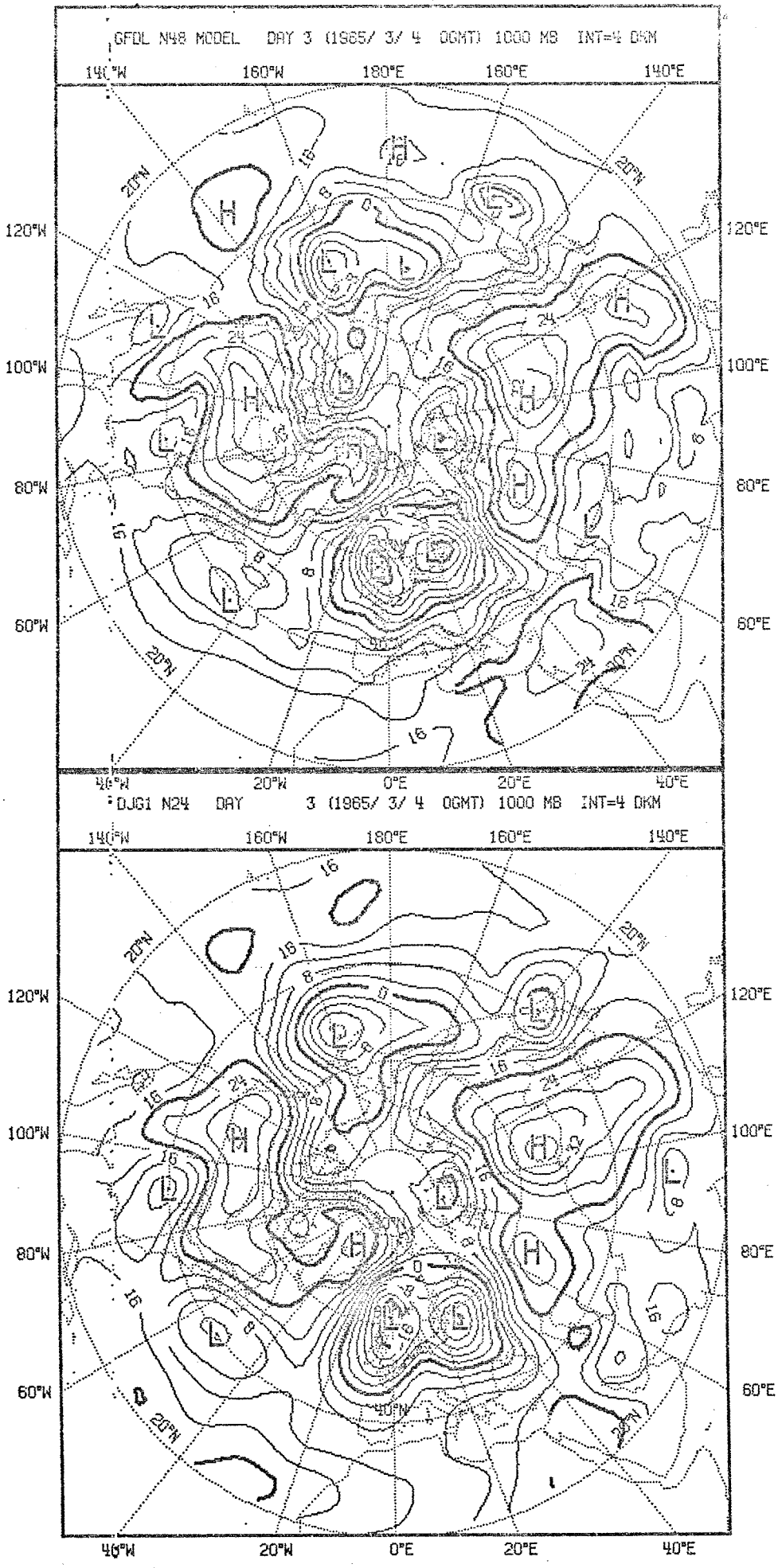

Fig. 3.1.14 : Observed (top left) and predicted fields of 1000 mb geopotential height, day 3.

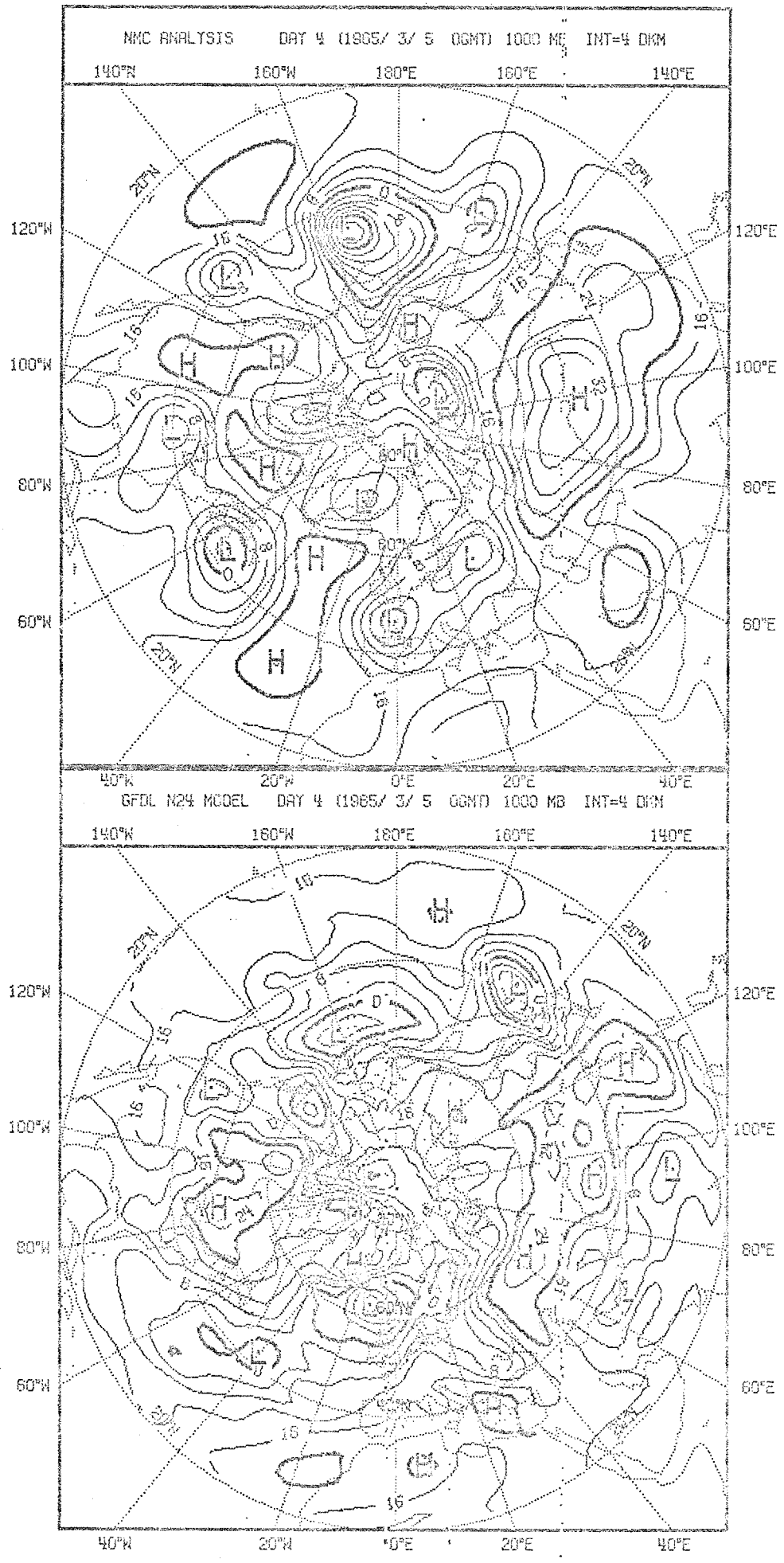
NMC ANALYSIS DAY 4 (1985/ 3/ 5 0GMT) 1000 MB INT=4 DKM
140°W
160°W
180°E
160°E
140°E
120°W
120°E
100°W
100°E
80°W
80°E
60°W
60°E
40°W
20°W
0°E
20°E
40°E
20°N
GFDL N24 MODEL DAY 4 (1985/ 3/ 5 0GMT) 1000 MB INT=4 DKM

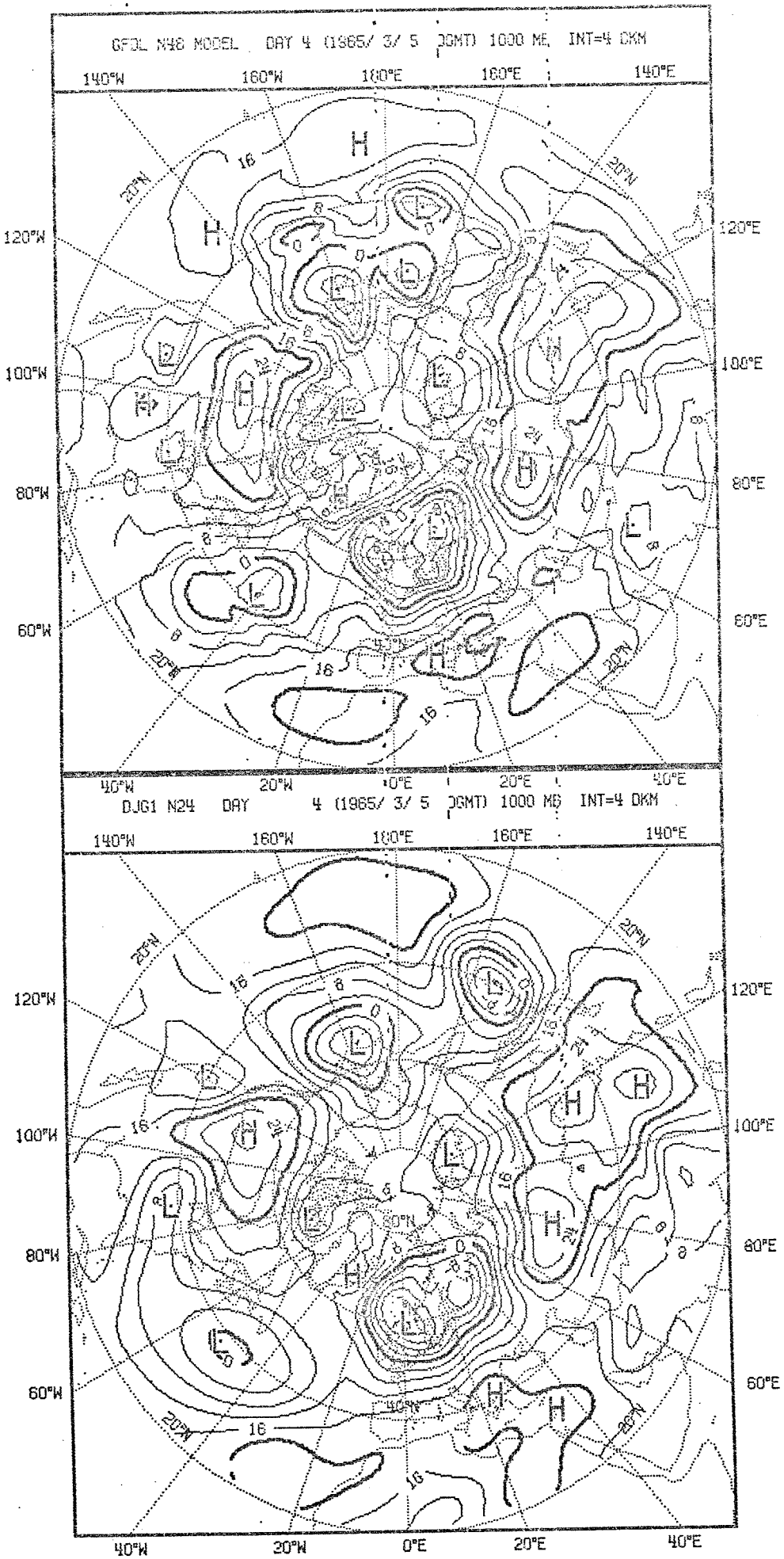

Fig. 3.1.15: Observed (top left) and predicted fields of 1000 mb geopotential height, day 4.

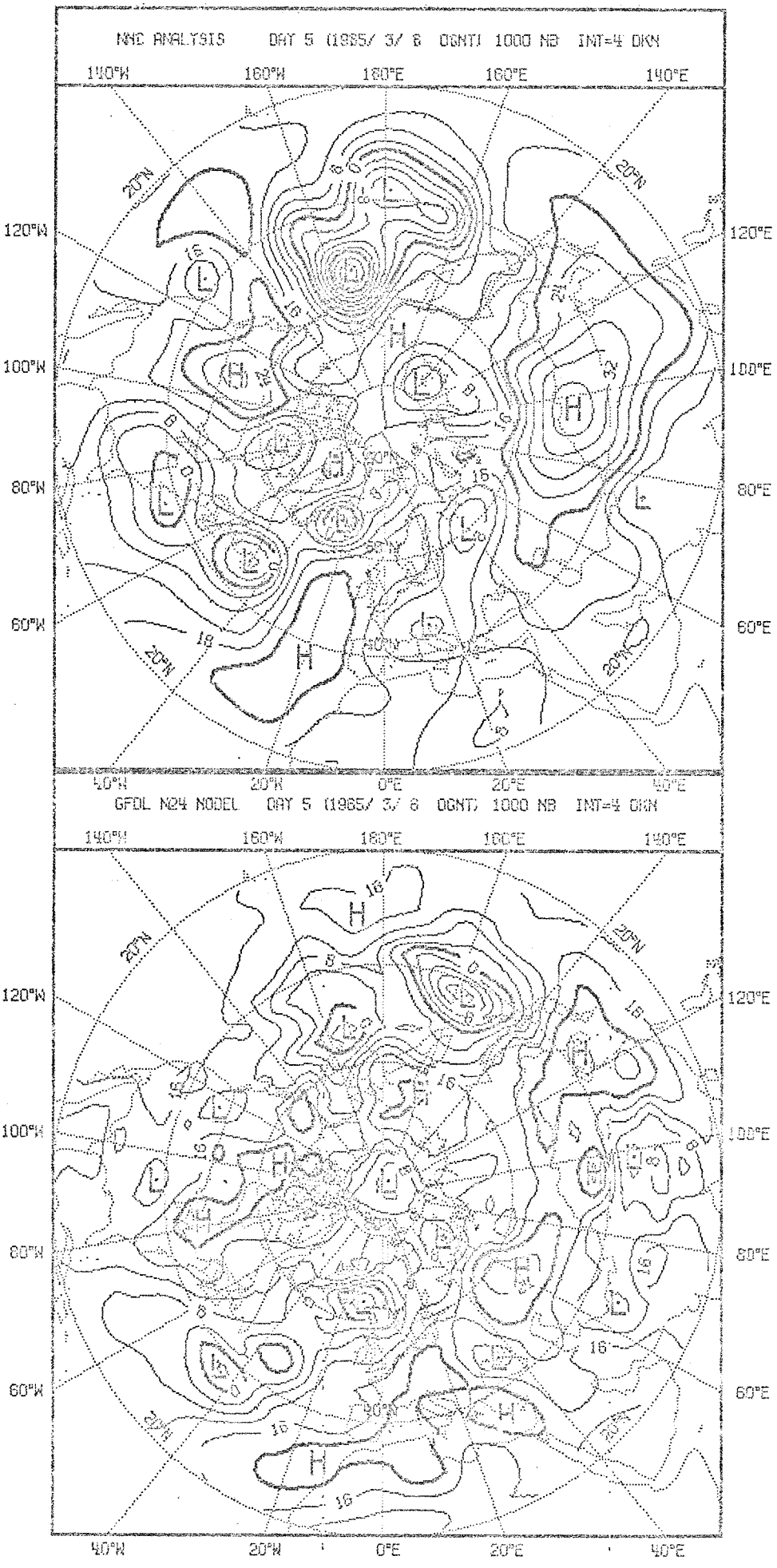
NMC ANALYSIS DAY 5 (1985/ 3/ 6 0GMT) 1000 MB INT=4 DKM
140°W
160°W
180°E
160°E
140°E
120°W
100°W
80°W
60°W
120°E
100°E
80°E
60°E
20°N
40°W
20°W
0°E
20°E
40°E
GFDL N24 MODEL DAY 5 (1985/ 3/ 6 0GMT) 1000 MB INT=4 DKM

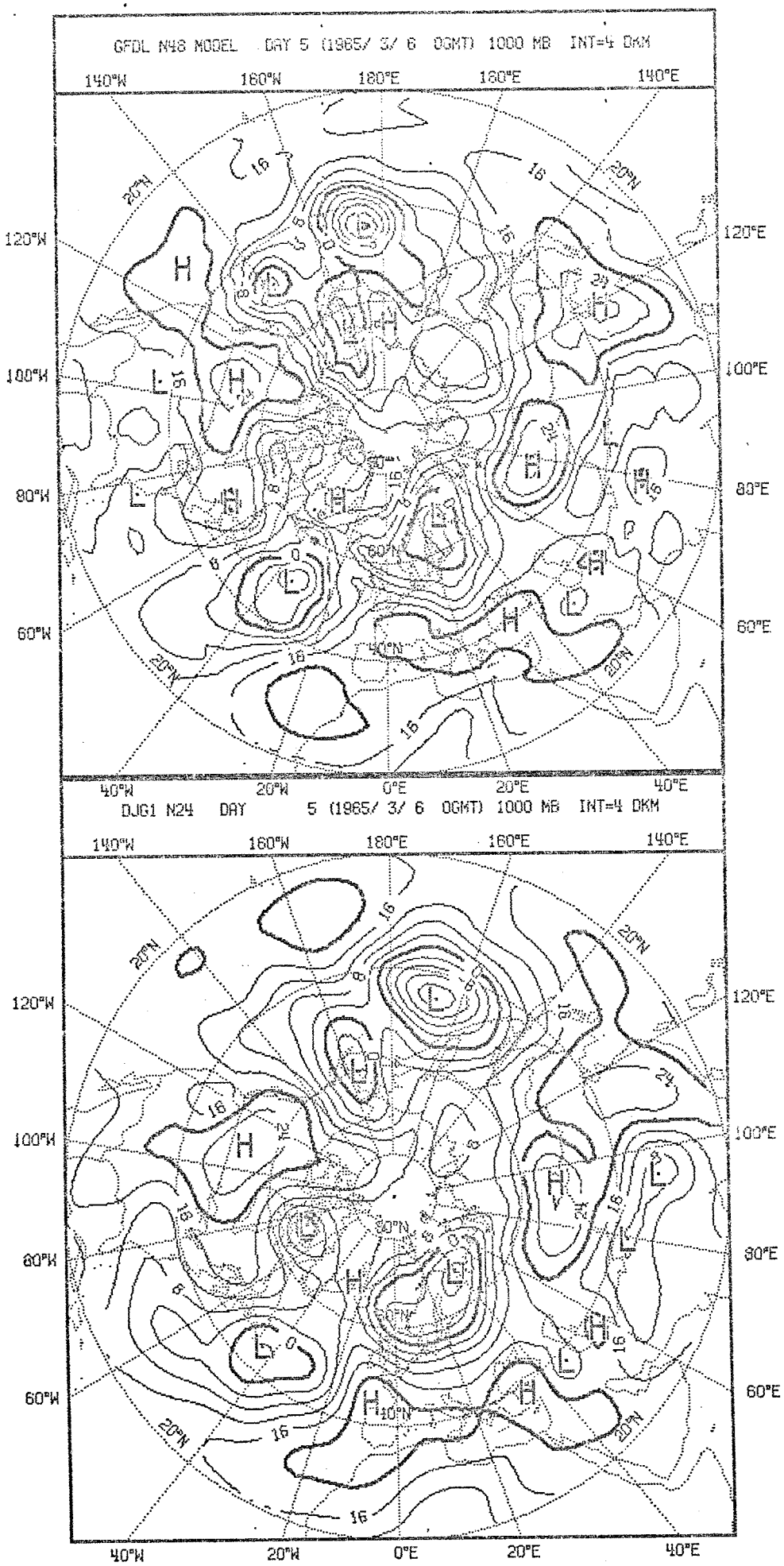

Fig. 3.1.16: Observed (top left) and predicted fields of 1000 mb geopotential height, day 5.

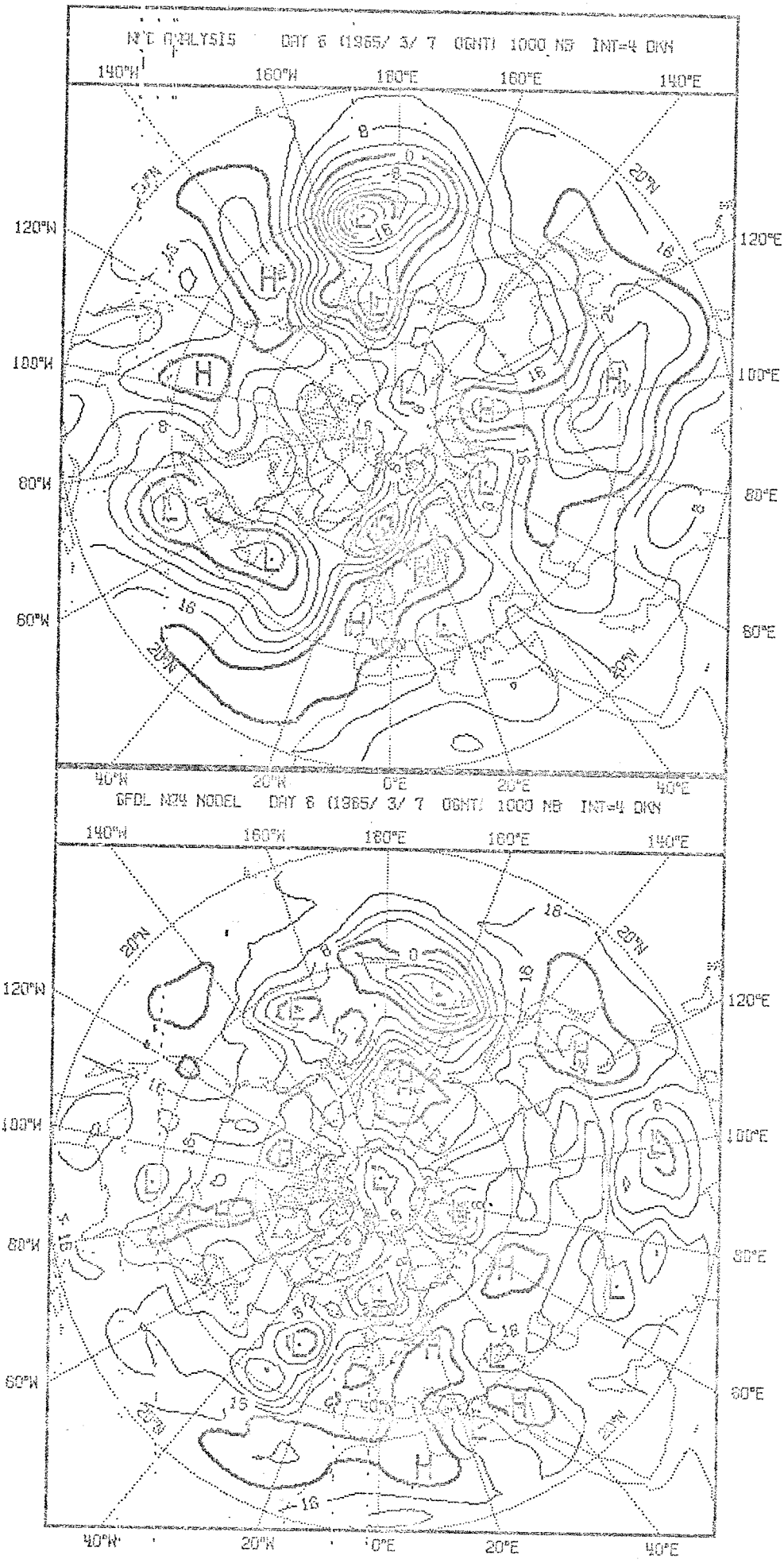
NMC ANALYSIS DAY 6 (1985/ 3/ 7 0GMT) 1000 MB INT=4 DAM
140°W
160°W
180°E
160°E
140°E
120°W
100°W
80°W
60°W
120°E
100°E
80°E
60°E
40°N
20°N
0°E
20°E
40°E
GFDL N24 MODEL DAY 6 (1985/ 3/ 7 0GMT) 1000 MB INT=4 DAM

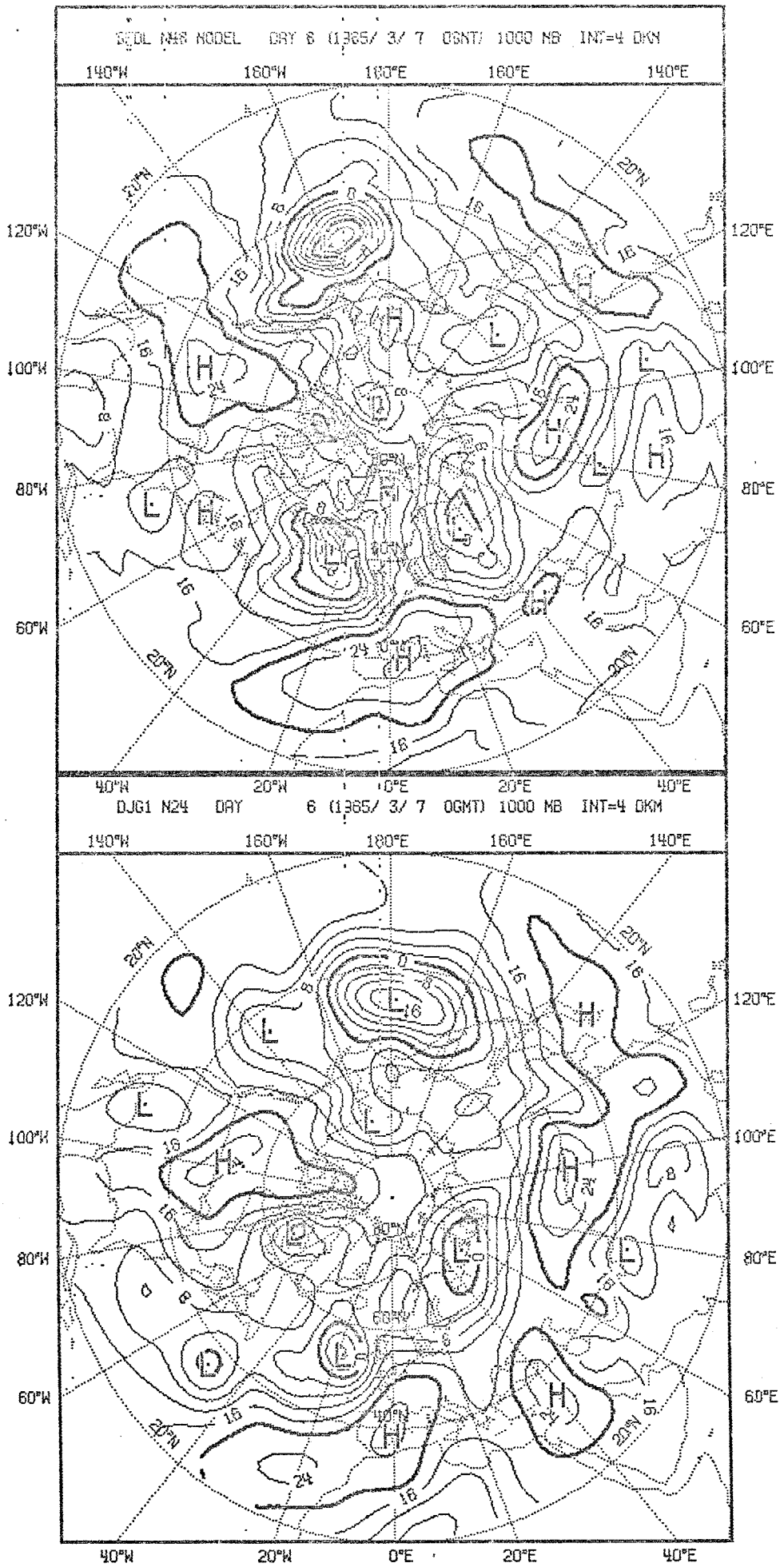

Fig. 3.1.17: Observed (top left) and predicted fields of 1000 mb geopotential height, day 6.

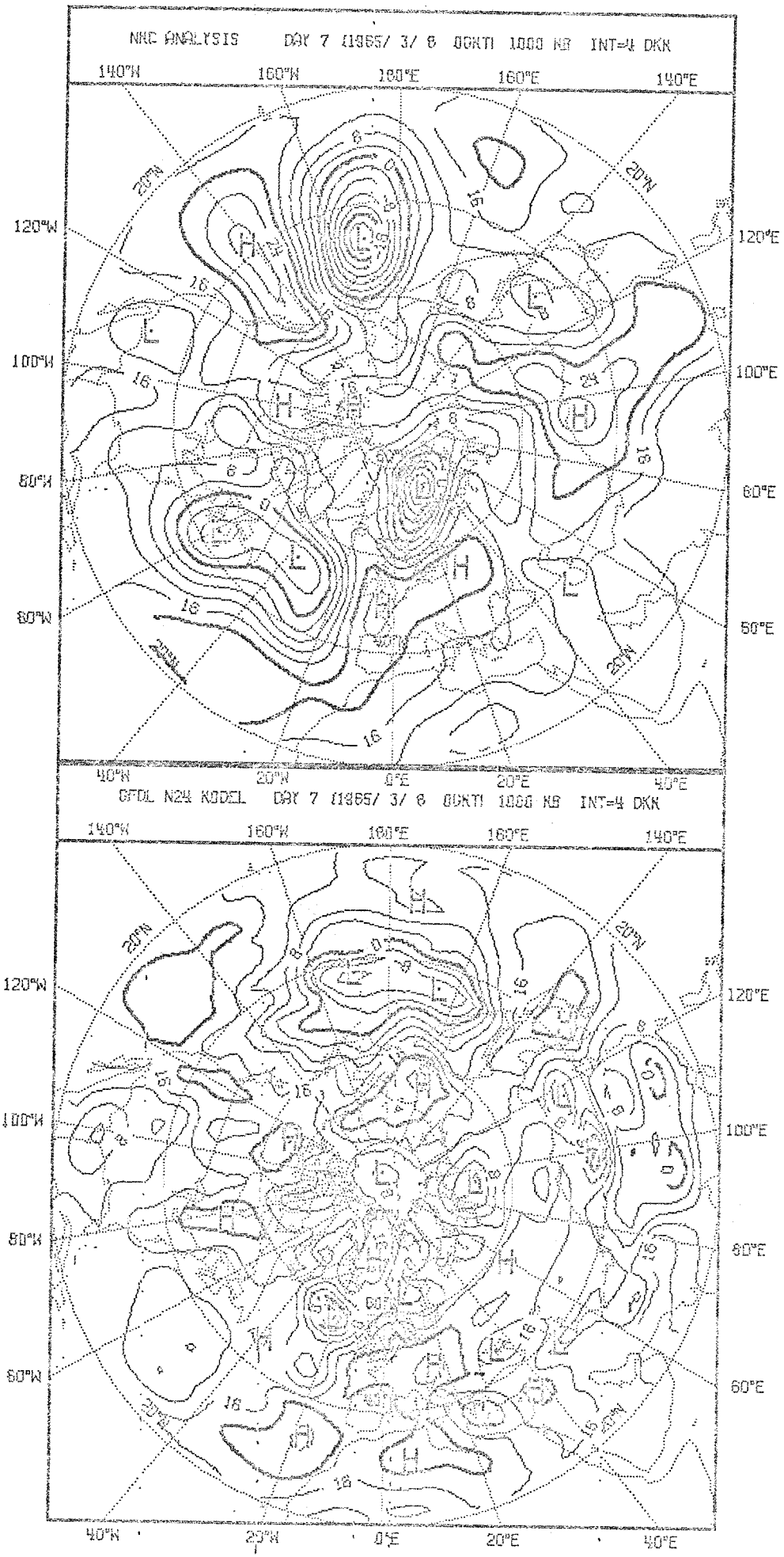
NMC ANALYSIS DAY 7 (1985/ 3/ 6 00GMT) 1000 MB INT=4 DKM
140°W
160°W
180°E
160°E
140°E
120°W
100°W
80°W
60°E
40°W
20°W
0°E
20°E
40°E
GFDL N24 MODEL DAY 7 (1985/ 3/ 6 00GMT) 1000 MB INT=4 DKM

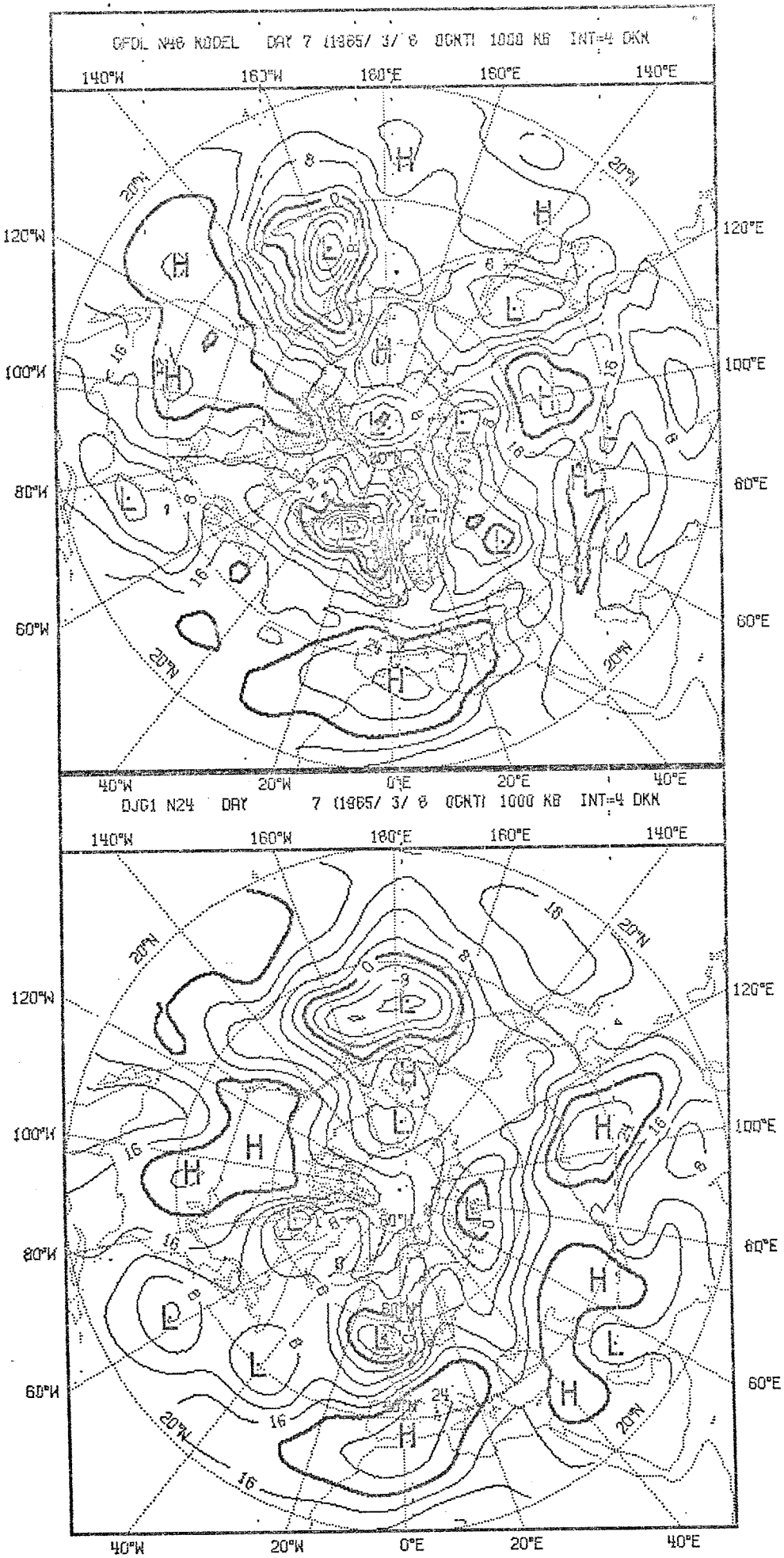

Fig. 3.1.18 : Observed (top left) and predicted fields of 1000 mb geopotential height, day 7.

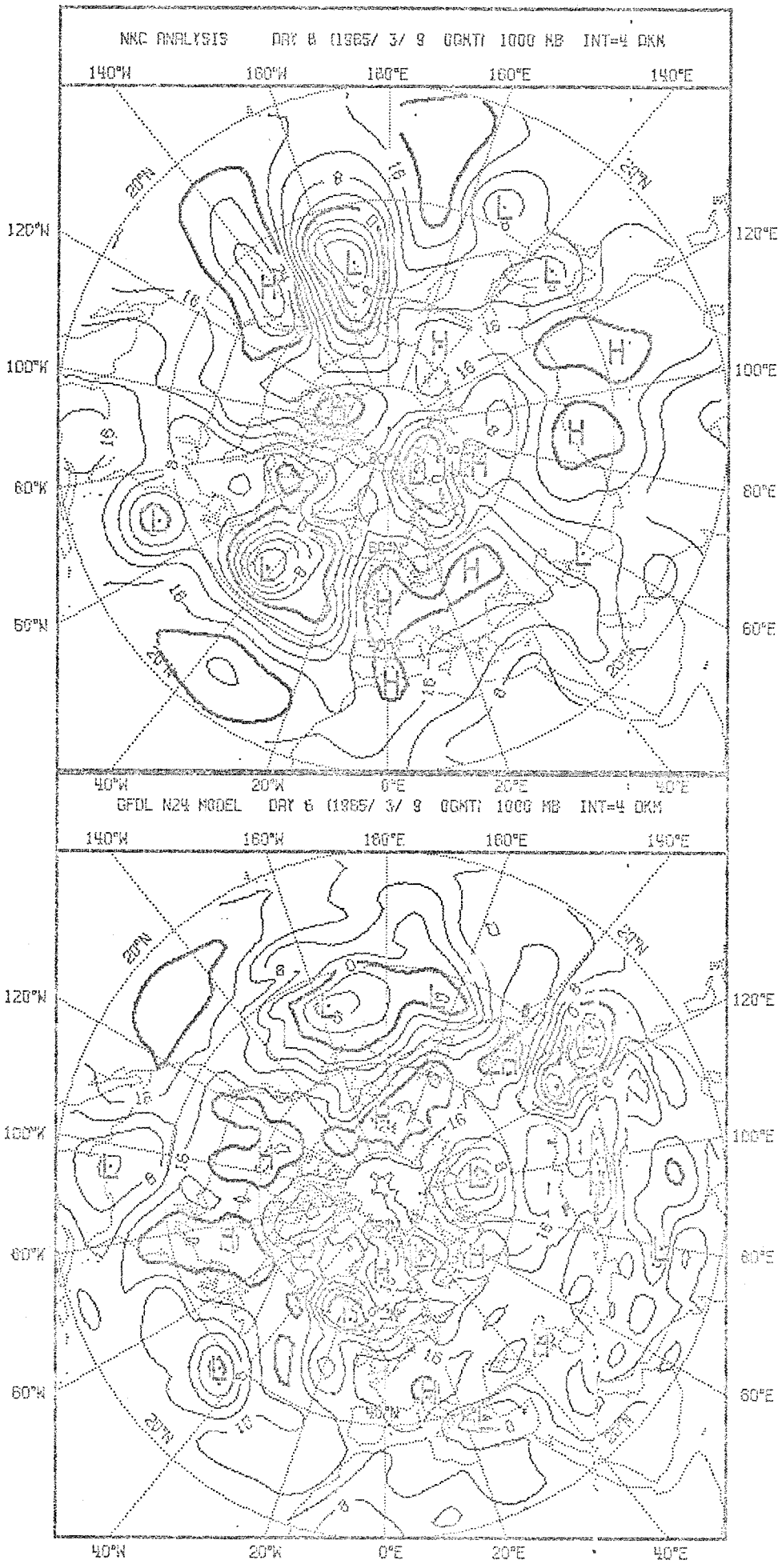
NMC ANALYSIS DAY 6 (1985/ 3/ 9 0GMT) 1000 MB INT=4 DAM
140°W
160°W
180°E
160°E
140°E
120°W
100°W
80°W
60°W
120°E
100°E
80°E
60°E
40°W
20°W
0°E
20°E
40°E
GFDL N24 MODEL DAY 6 (1985/ 3/ 9 0GMT) 1000 MB INT=4 DAM

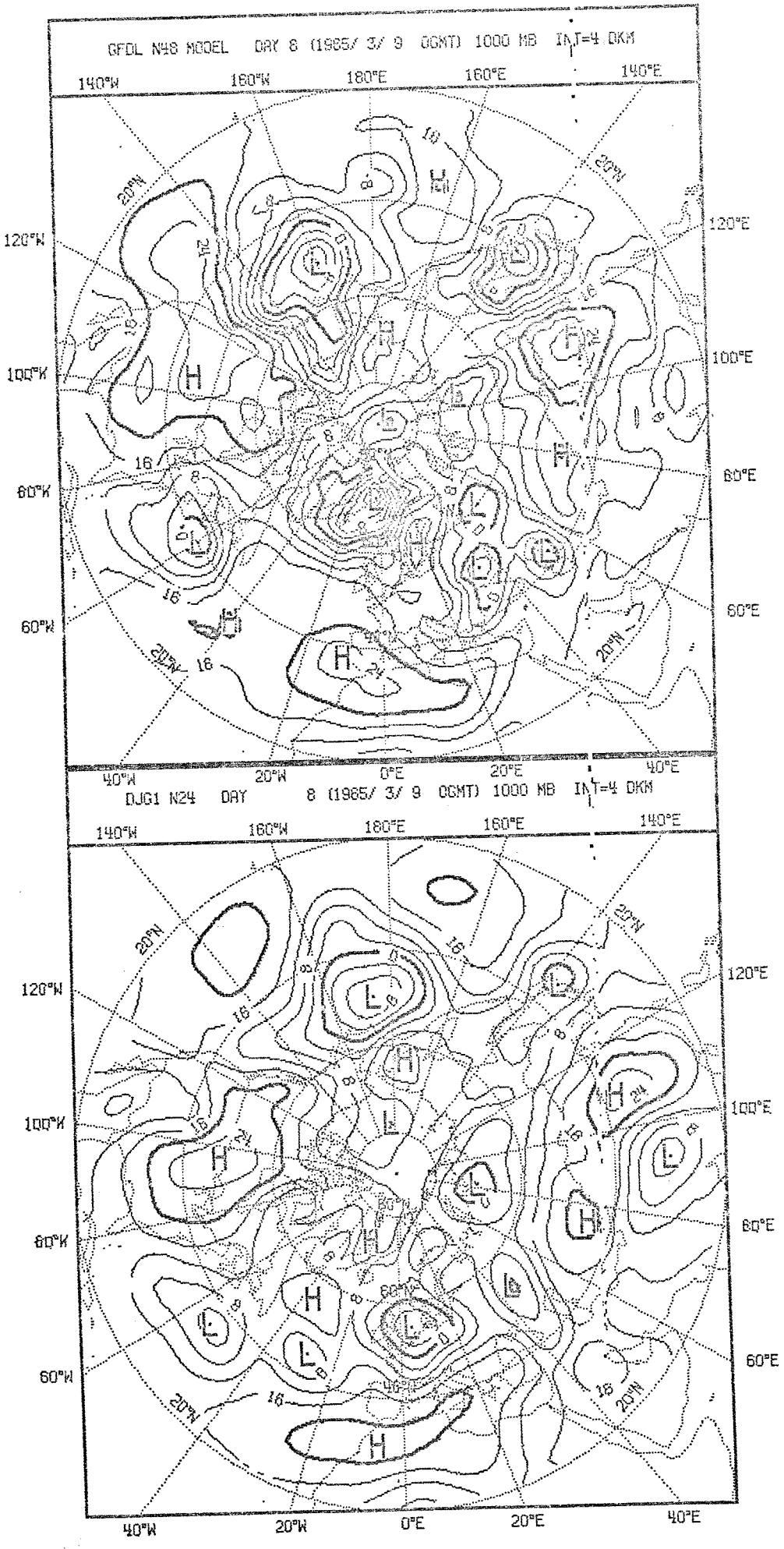

Fig. 3.1.19: Observed (top left) and predicted fields of 1000 mb geopotential height, day 8.

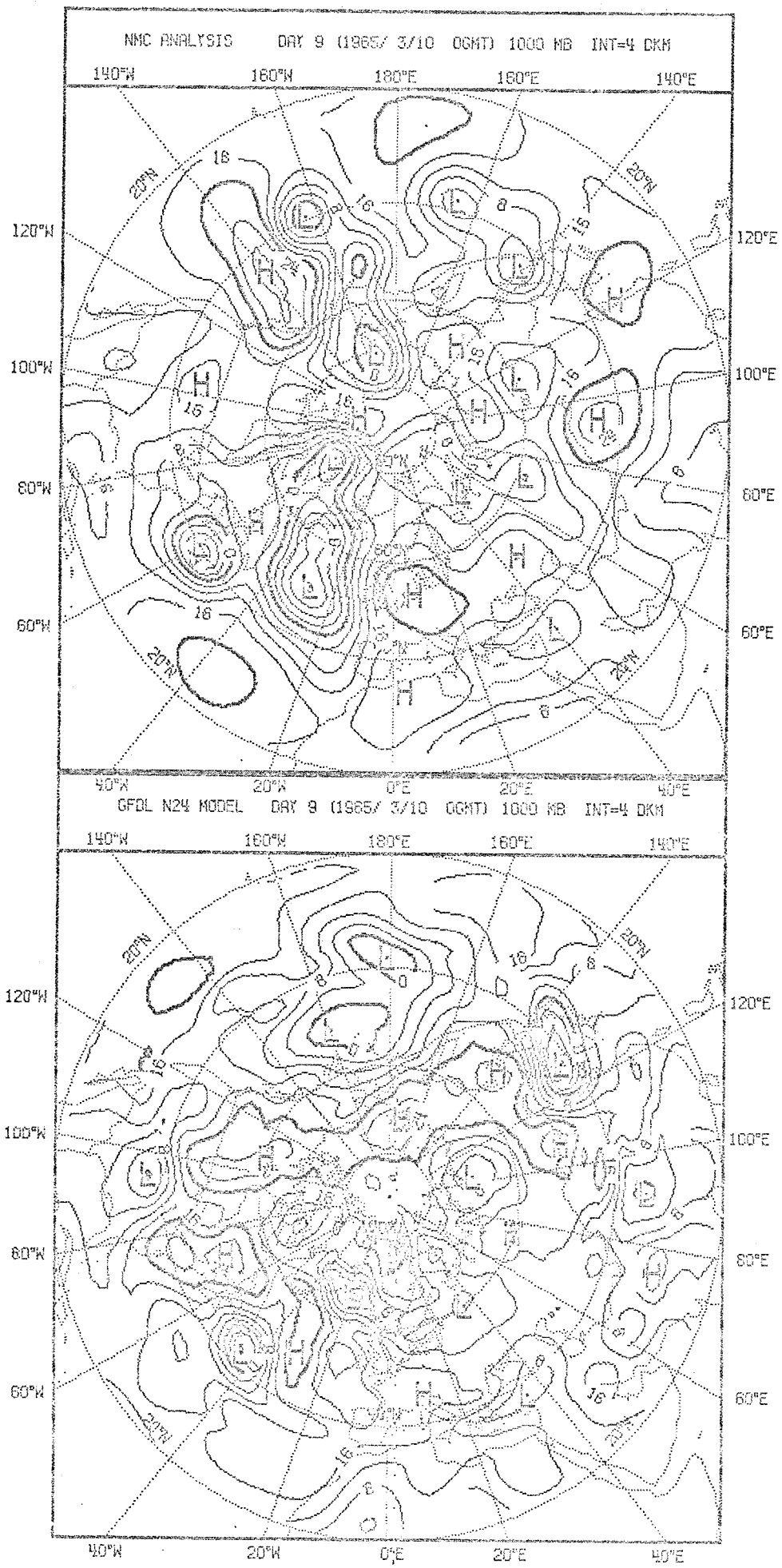
NMC ANALYSIS DAY 9 (1985/ 3/10 0GMT) 1000 MB INT=4 DKM
140°W
160°W
180°E
160°E
140°E
120°W
100°W
80°W
60°W
120°E
100°E
80°E
60°E
40°W
20°W
0°E
20°E
40°E
20°N
16
8
GFDL N24 MODEL DAY 9 (1985/ 3/10 0GMT) 1000 MB INT=4 DKM

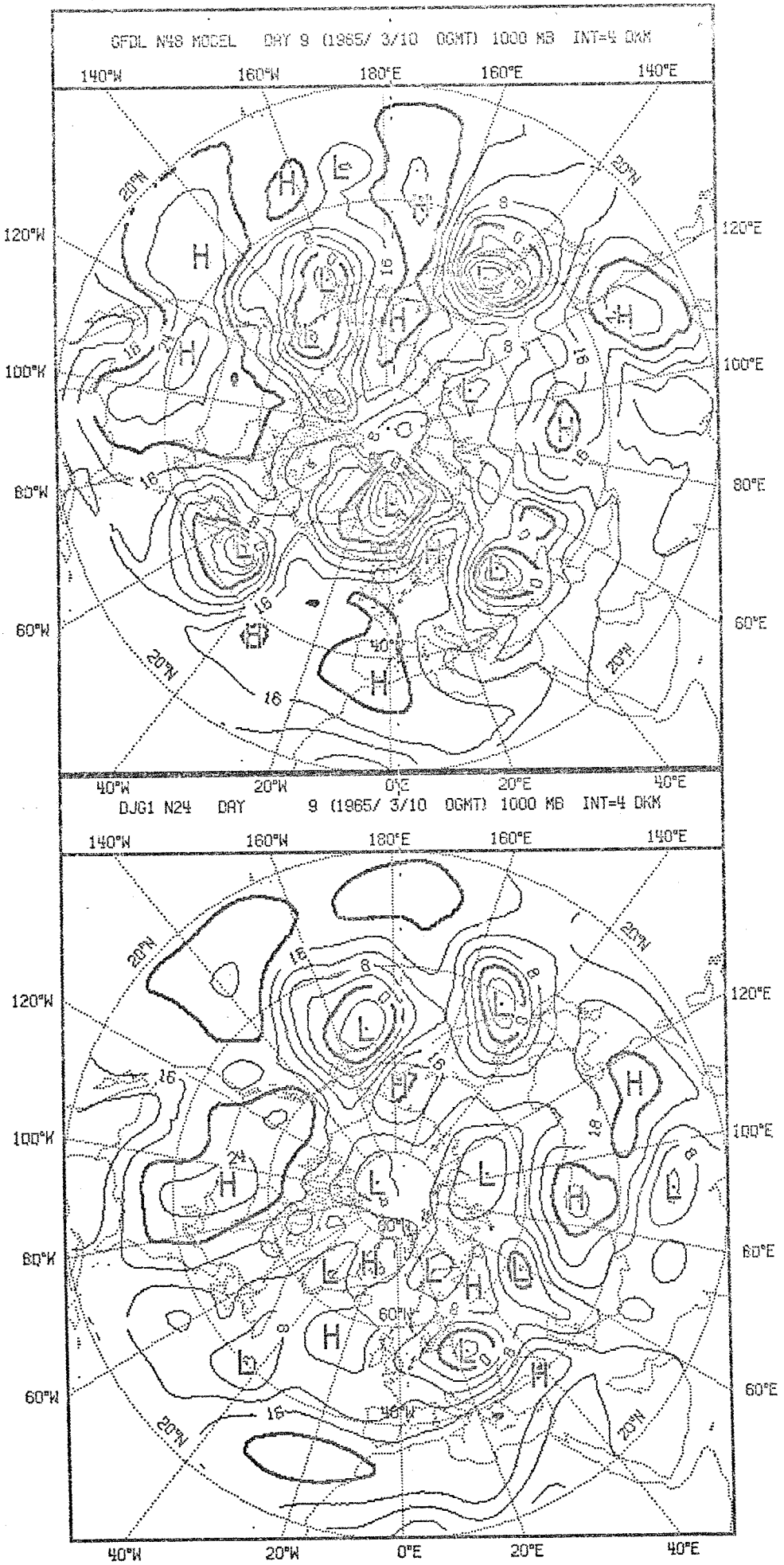

Fig. 3.1.20: Observed (top left) and predicted fields of 1000 mb geopotential height, day 9.

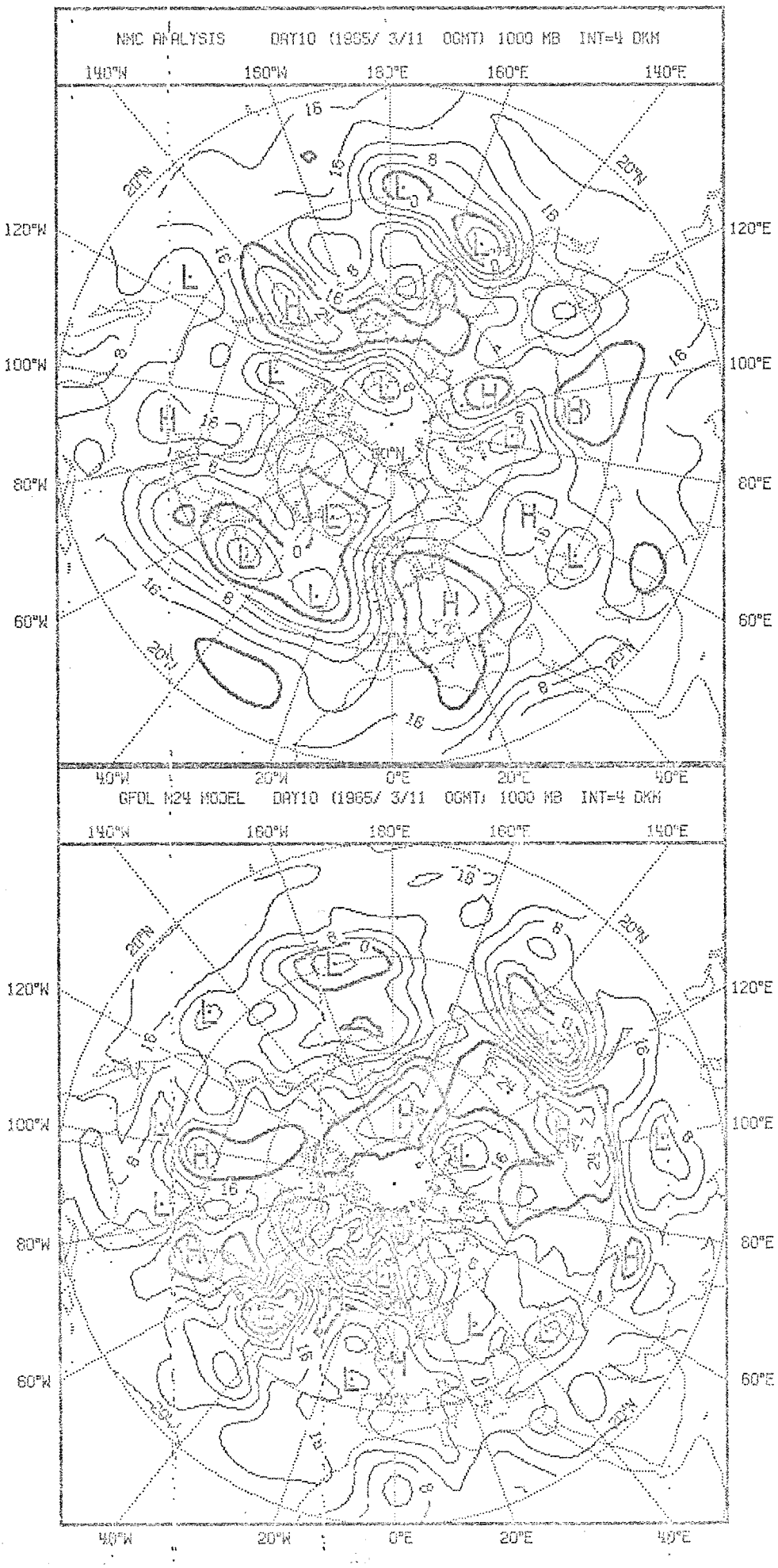
NMC ANALYSIS DAY10 (1985/ 3/11 00GMT) 1000 MB INT=4 DKM
140°W
160°W
180°E
160°E
140°E
120°W
100°W
80°W
60°W
120°E
100°E
80°E
60°E
20°N
40°W
20°W
0°E
20°E
40°E
GFDL M24 MODEL DAY10 (1985/ 3/11 00GMT) 1000 MB INT=4 DKM

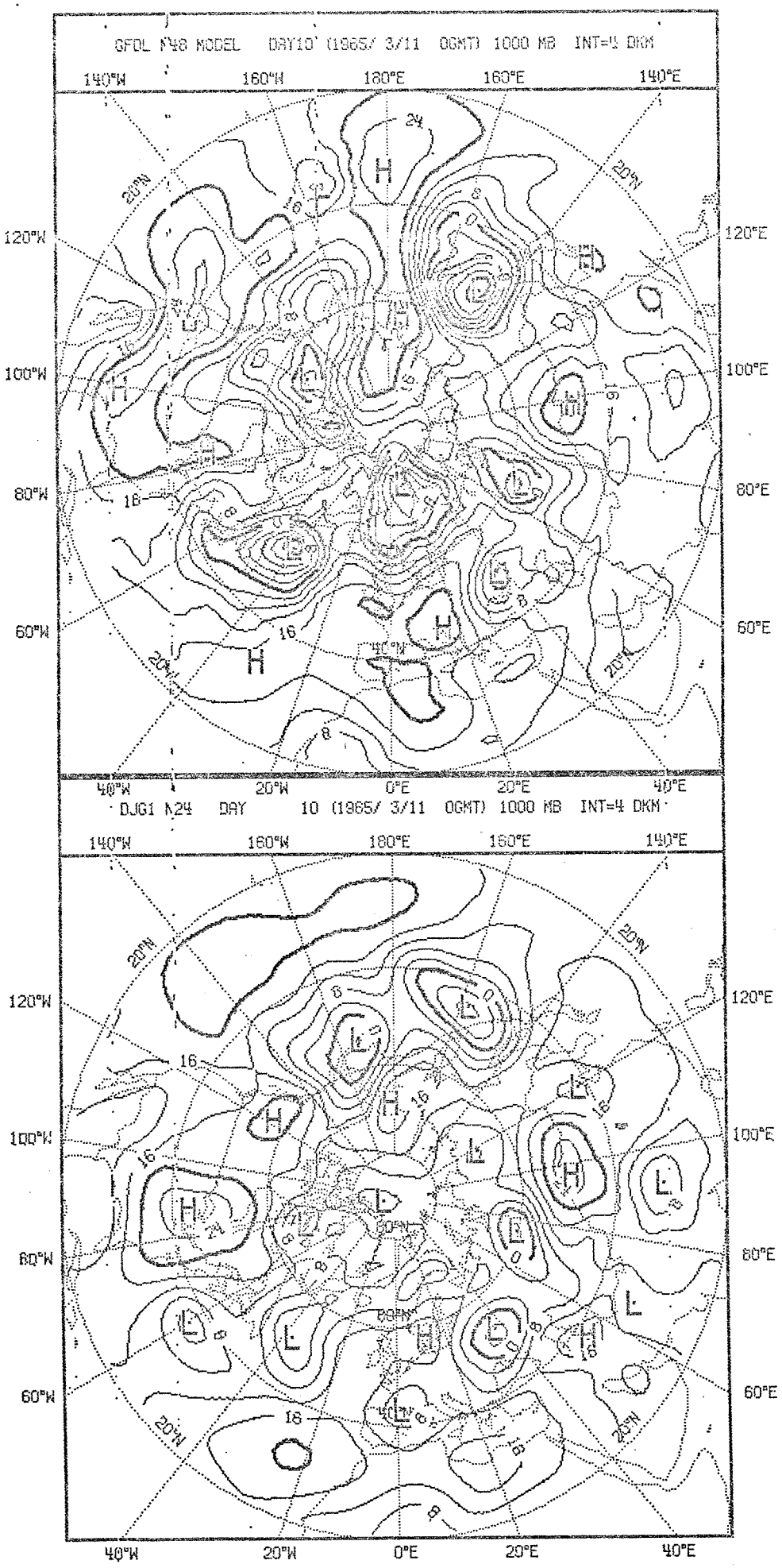

Fig. 3.1.21: Observed (top left) and predicted fields of 1000 mb geopotential height, day 10.

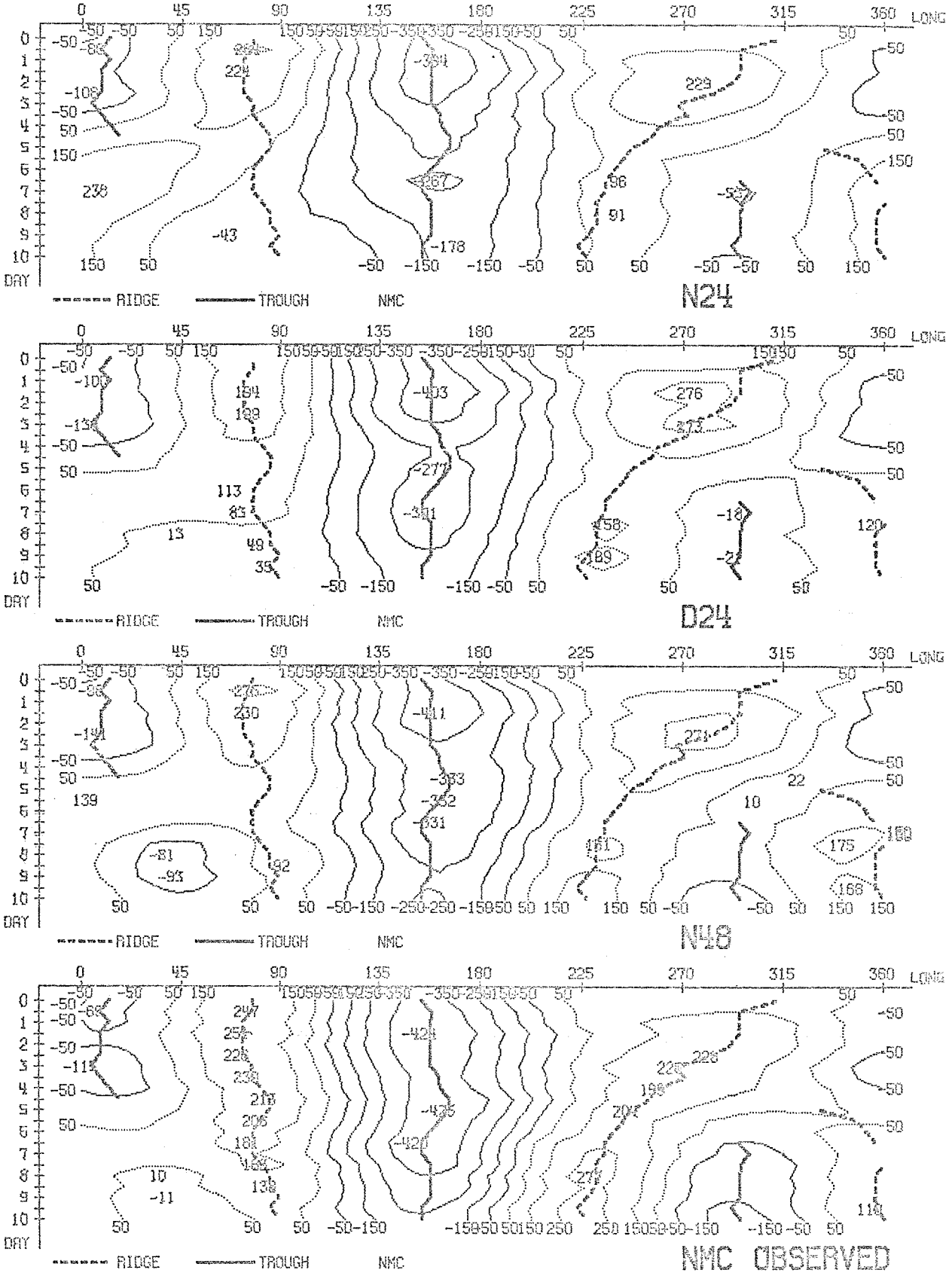

Fig. 3.1.22: Hovmöller's trough and ridge diagram, forecast and observed.

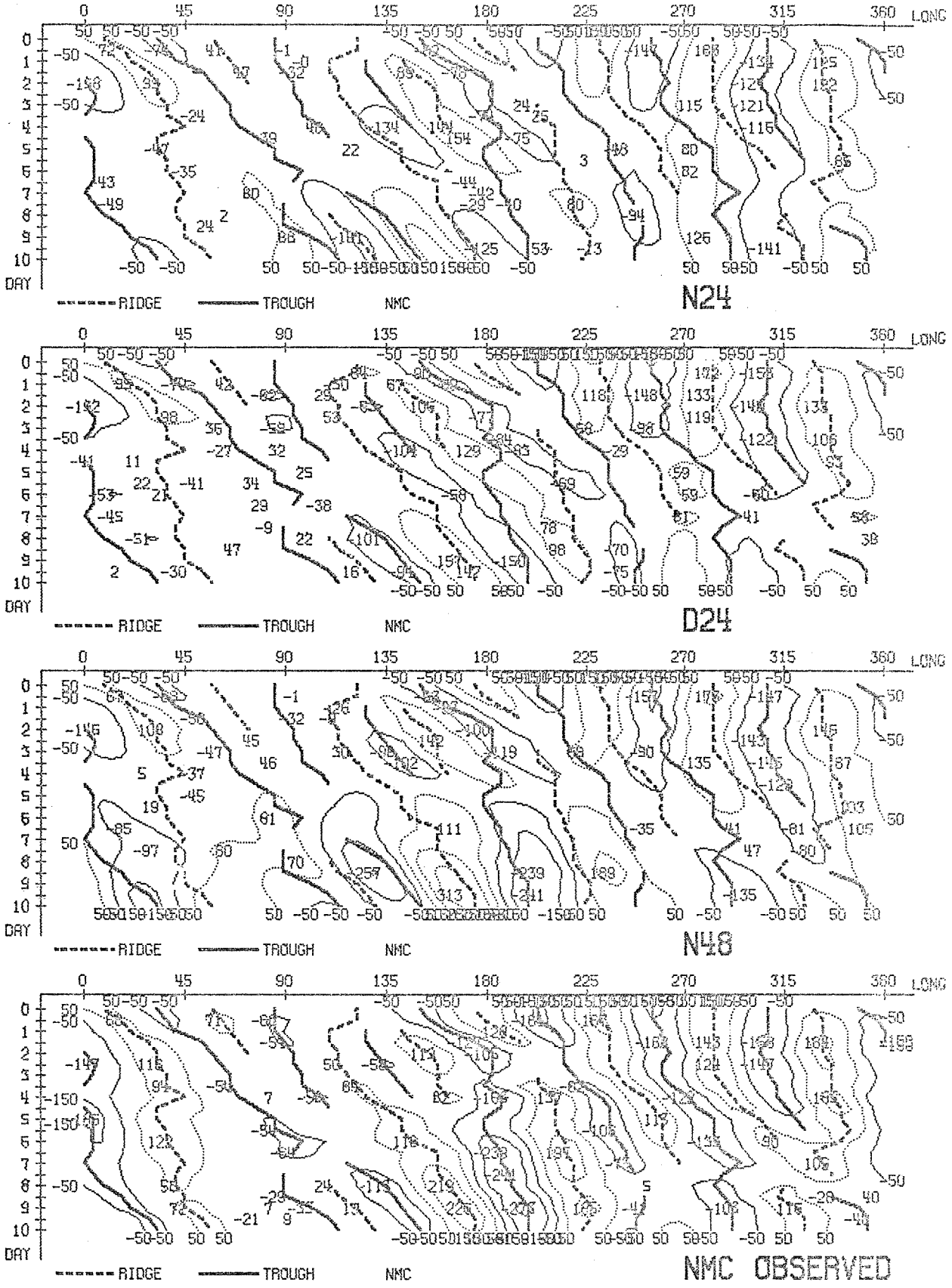

WAVENUMBER 4- 9 LATITUDE 40.0 N LEVEL 500 MB GEOP. HEIGHT

Fig. 3.1.23: Hovmöller's trough and ridge diagrams, forecast and observed.

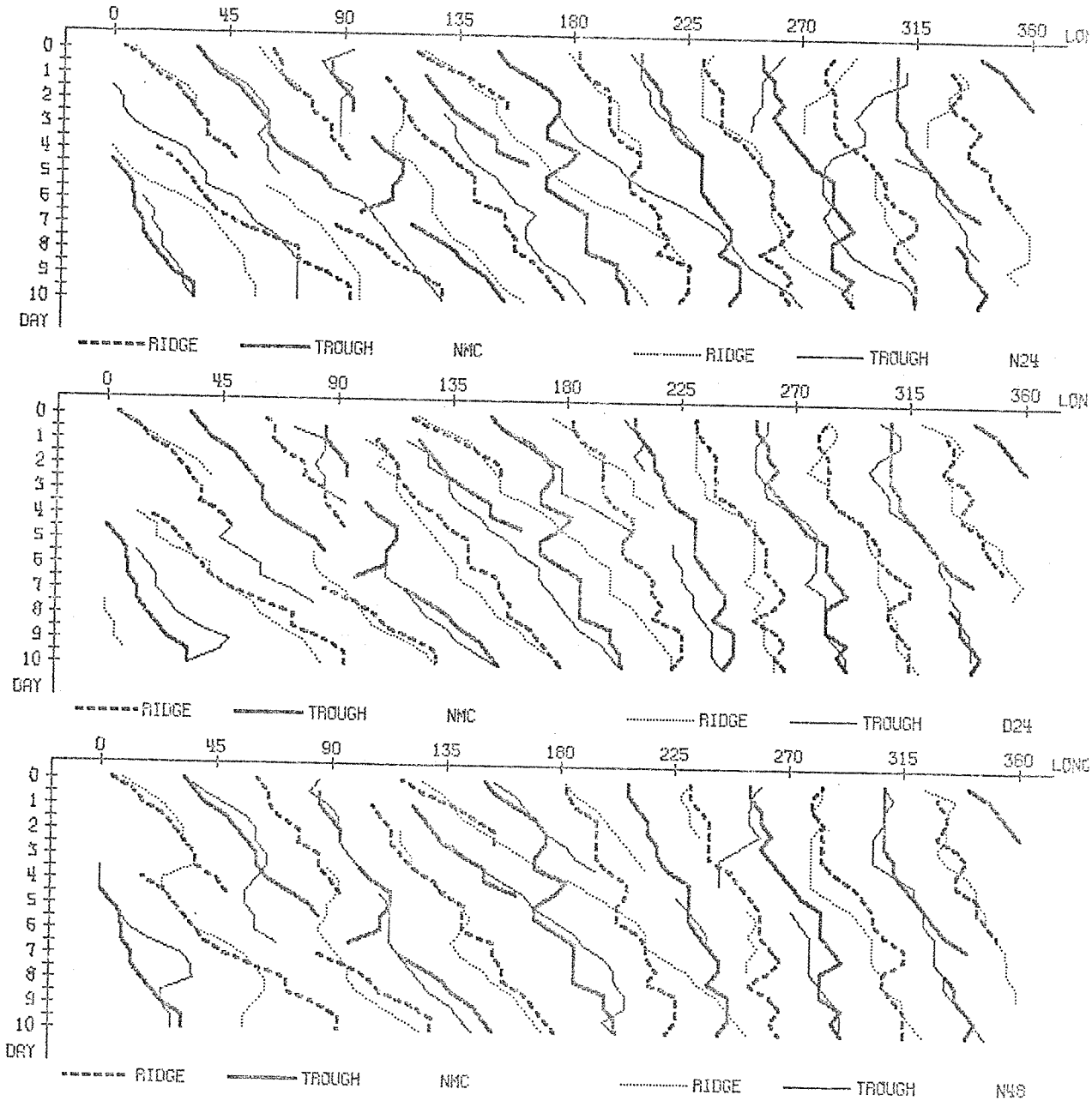

Fig. 3.1.24: Hovmöller's trough and ridge diagrams for transient waves, forecast and observed.

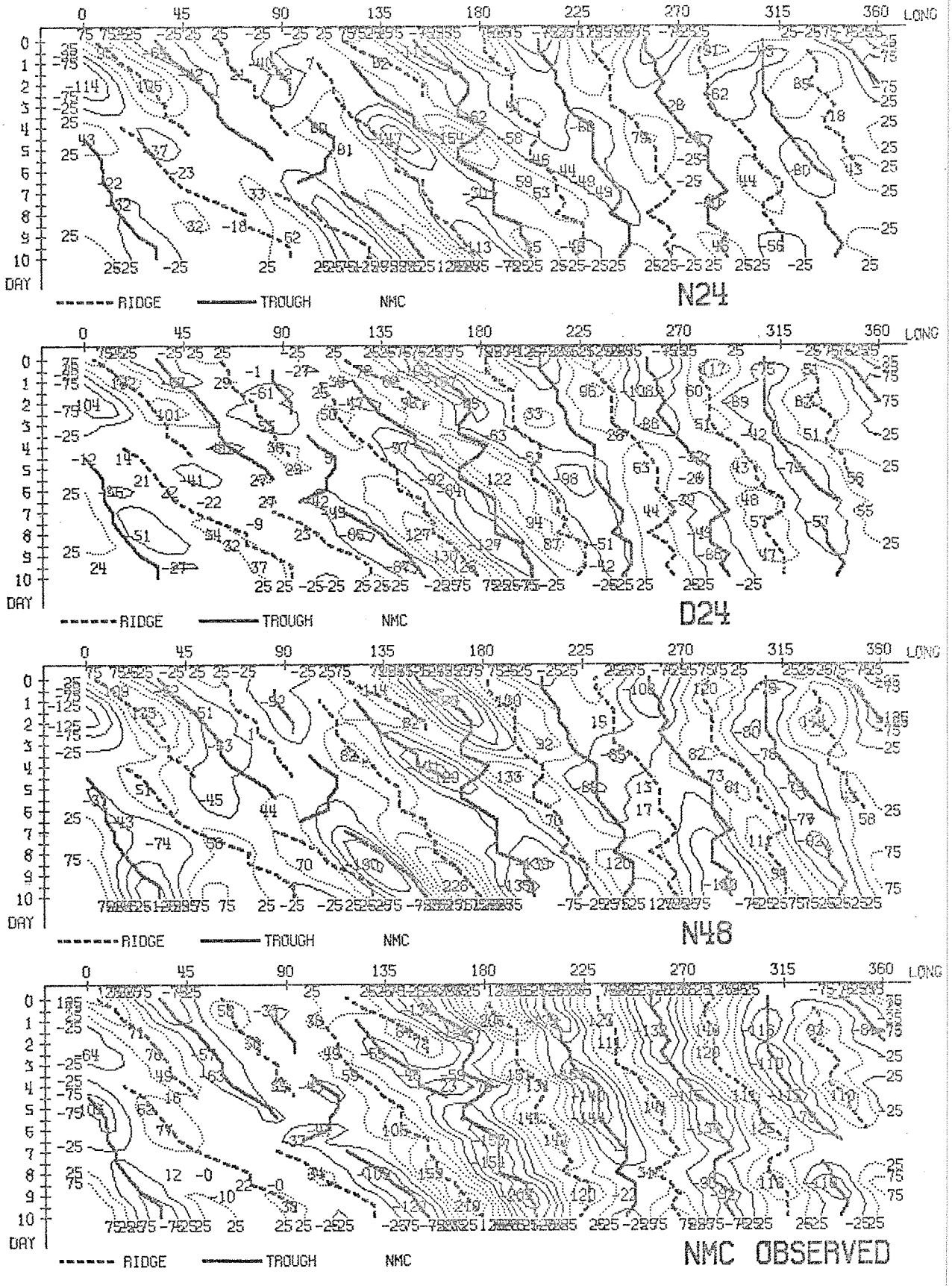

Fig. 3.1.25: Hovmöller's trough and ridge diagrams for transient waves, forecast and observed.

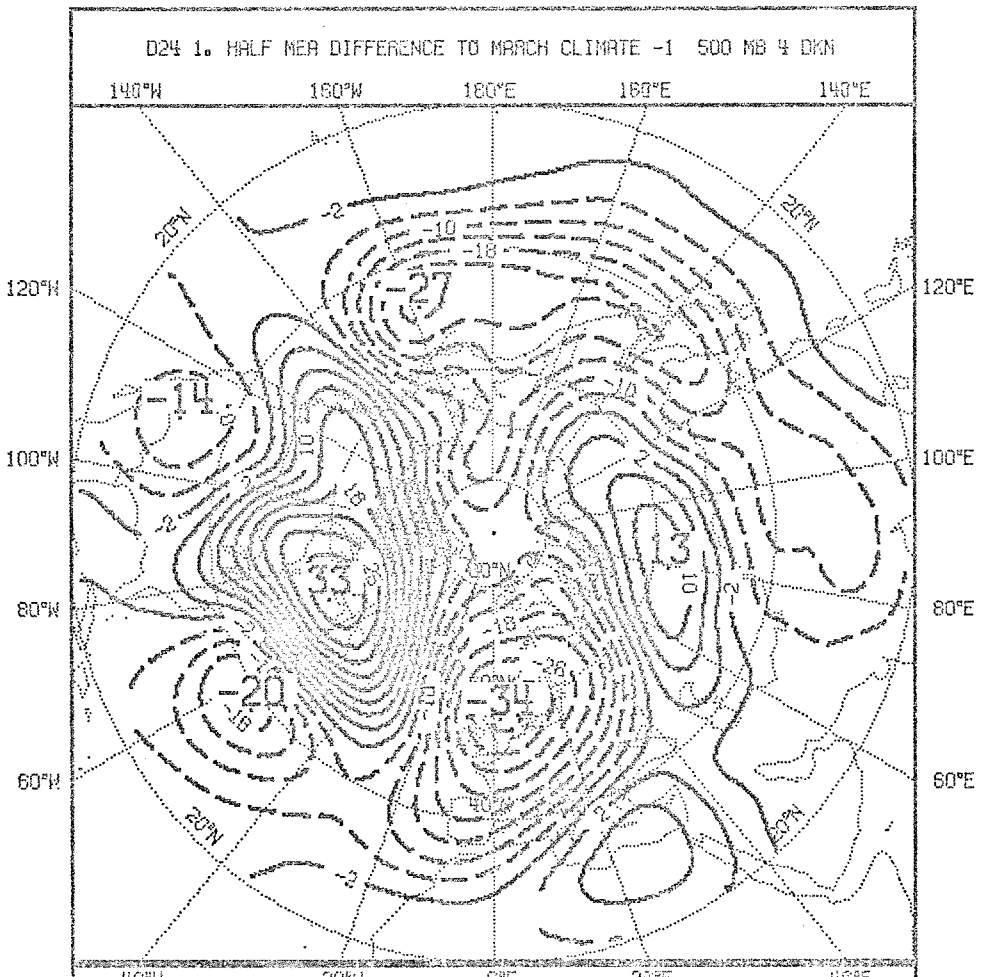
D24 1. HALF MEA DIFFERENCE TO MARCH CLIMATE -1 500 MB 4 DKN
140°W
160°W
180°E
160°E
140°E
120°W
120°E
100°W
100°E
80°W
80°E
60°W
60°E
40°W
20°W
0°E
20°E
40°E
20°N
-27
-14
-20
-30
33
13
-2
-10
-18

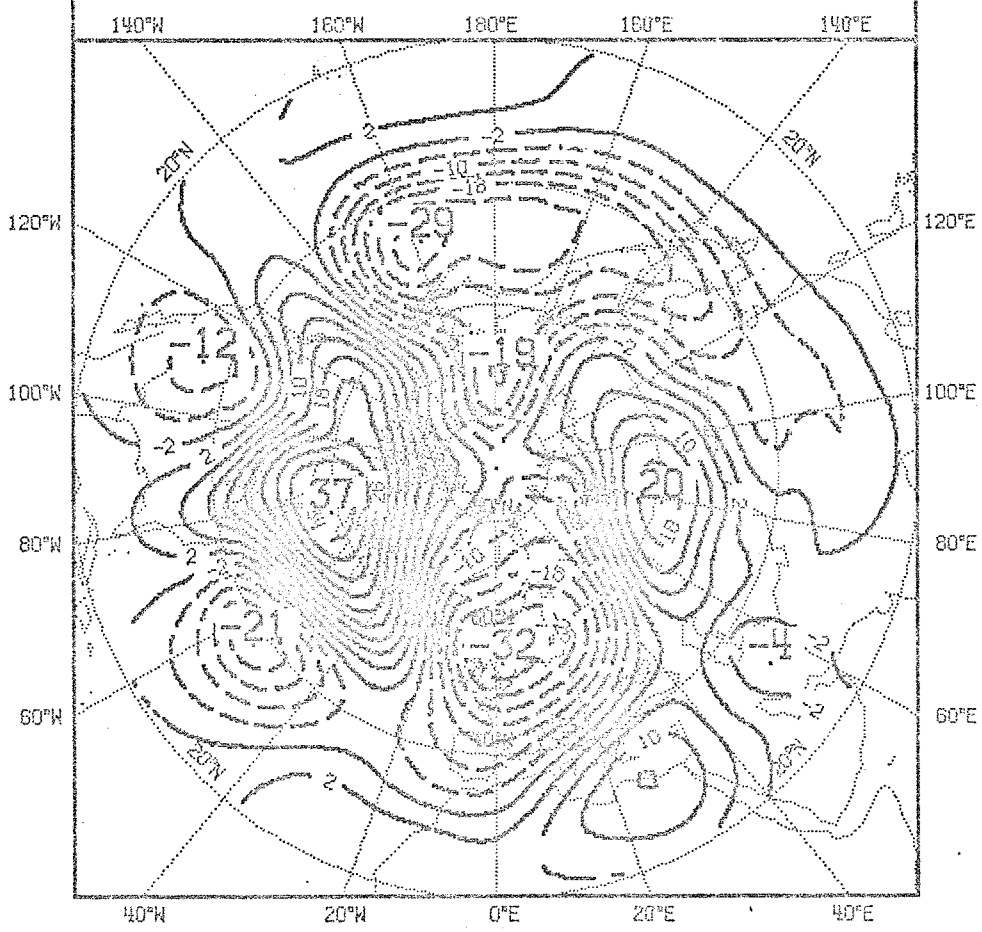
N48 1. HALF MEA DIFFERENCE TO MARCH CLIMATE -1 500 MB 4 DKN
140°W
160°W
180°E
160°E
140°E
120°W
120°E
100°W
100°E
80°W
80°E
60°W
60°E
40°W
20°W
0°E
20°E
40°E
20°N
-29
-13
-19
-21
-32
37
20
-4
2
-2
-10
-18

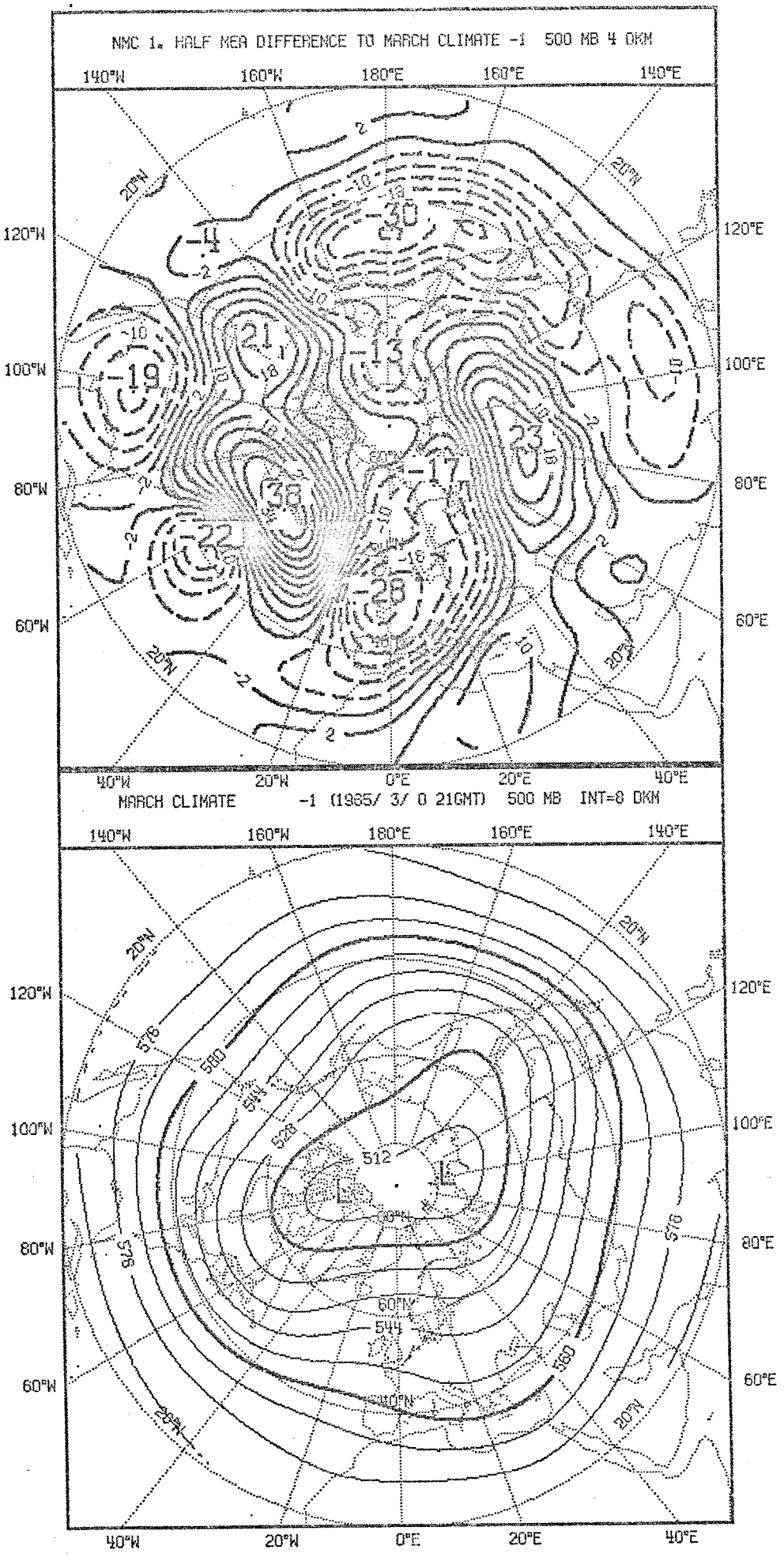

Fig. 3.1.26: Forecast and observed (top right) five day mean, 500 mb anomalies centred on day 2.5 .

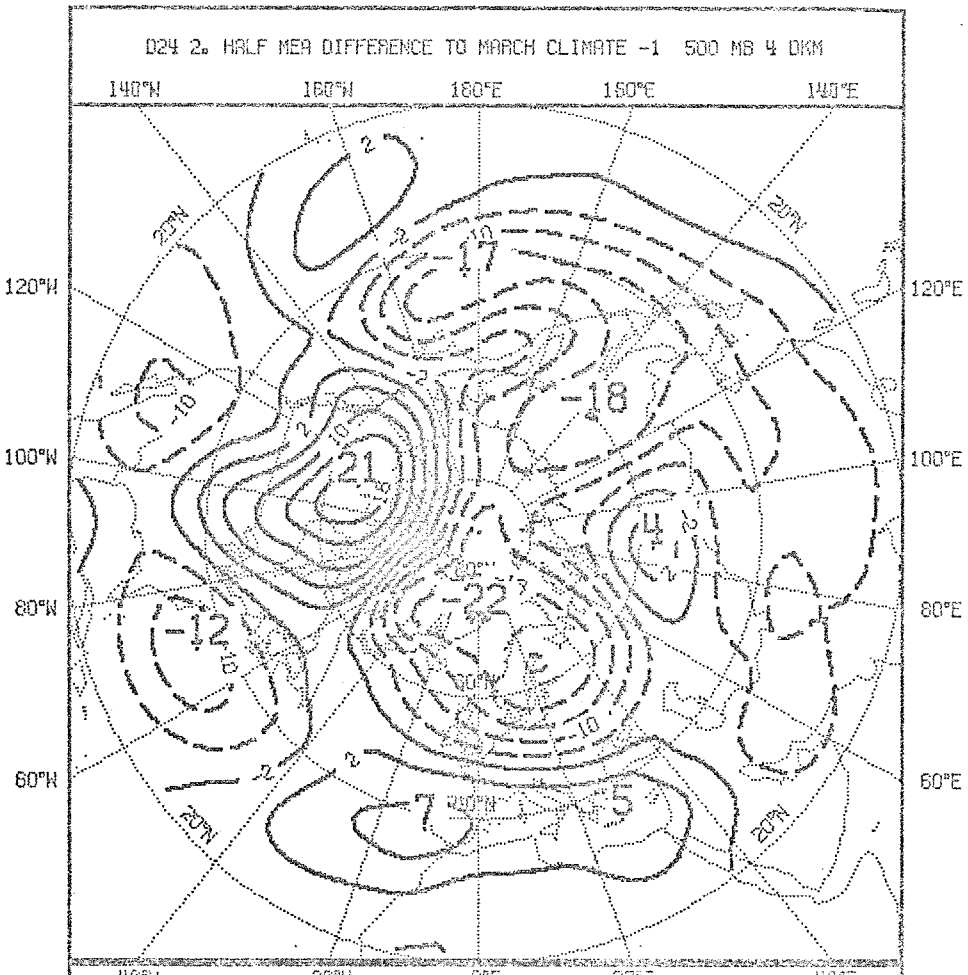
D24 2. HALF MEA DIFFERENCE TO MARCH CLIMATE -1 500 MB 4 DKM
140°W
160°W
180°E
160°E
140°E
120°W
120°E
100°W
100°E
80°W
80°E
60°W
60°E
40°W
20°W
0°E
20°E
40°E
20°N
-17
-18
-21
-22
-12
-7
-5
4

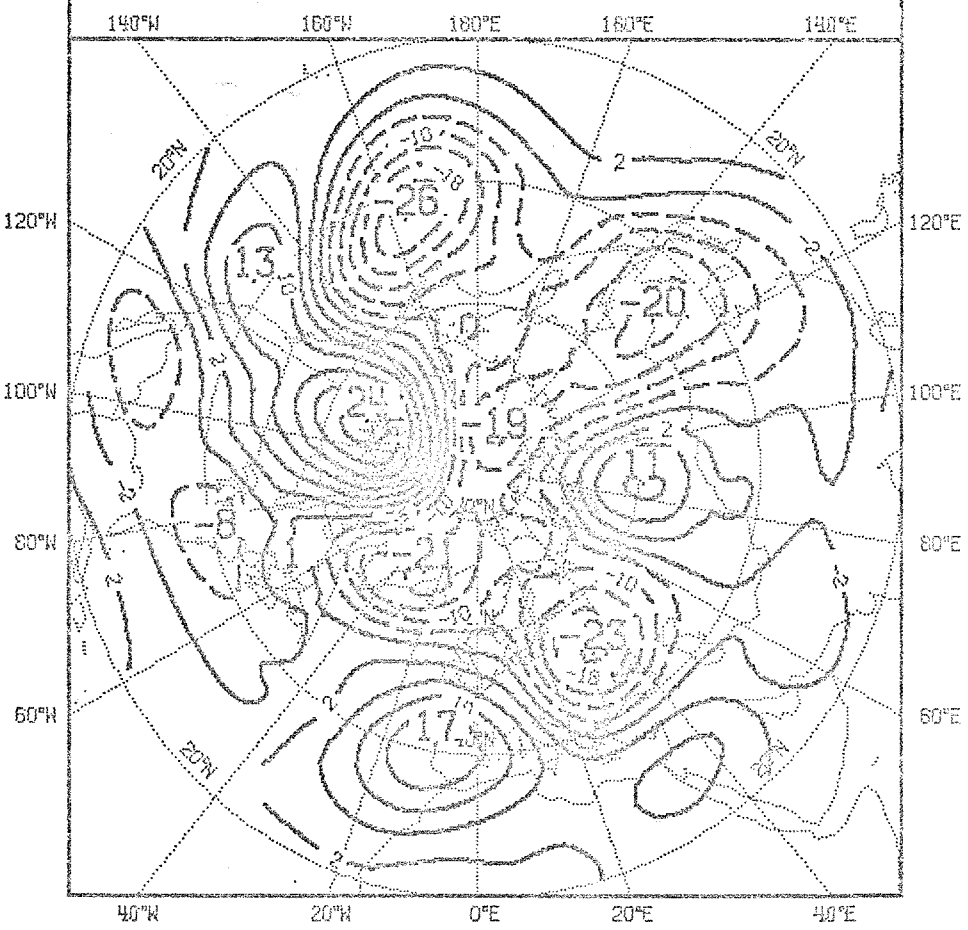
N48 2. HALF MEA DIFFERENCE TO MARCH CLIMATE -1 500 MB 4 DKM
140°W
160°W
180°E
160°E
140°E
120°W
120°E
100°W
100°E
80°W
80°E
60°W
60°E
40°W
20°W
0°E
20°E
40°E
20°N
26
13
-20
24
-19
-8
-2
-23
17
15

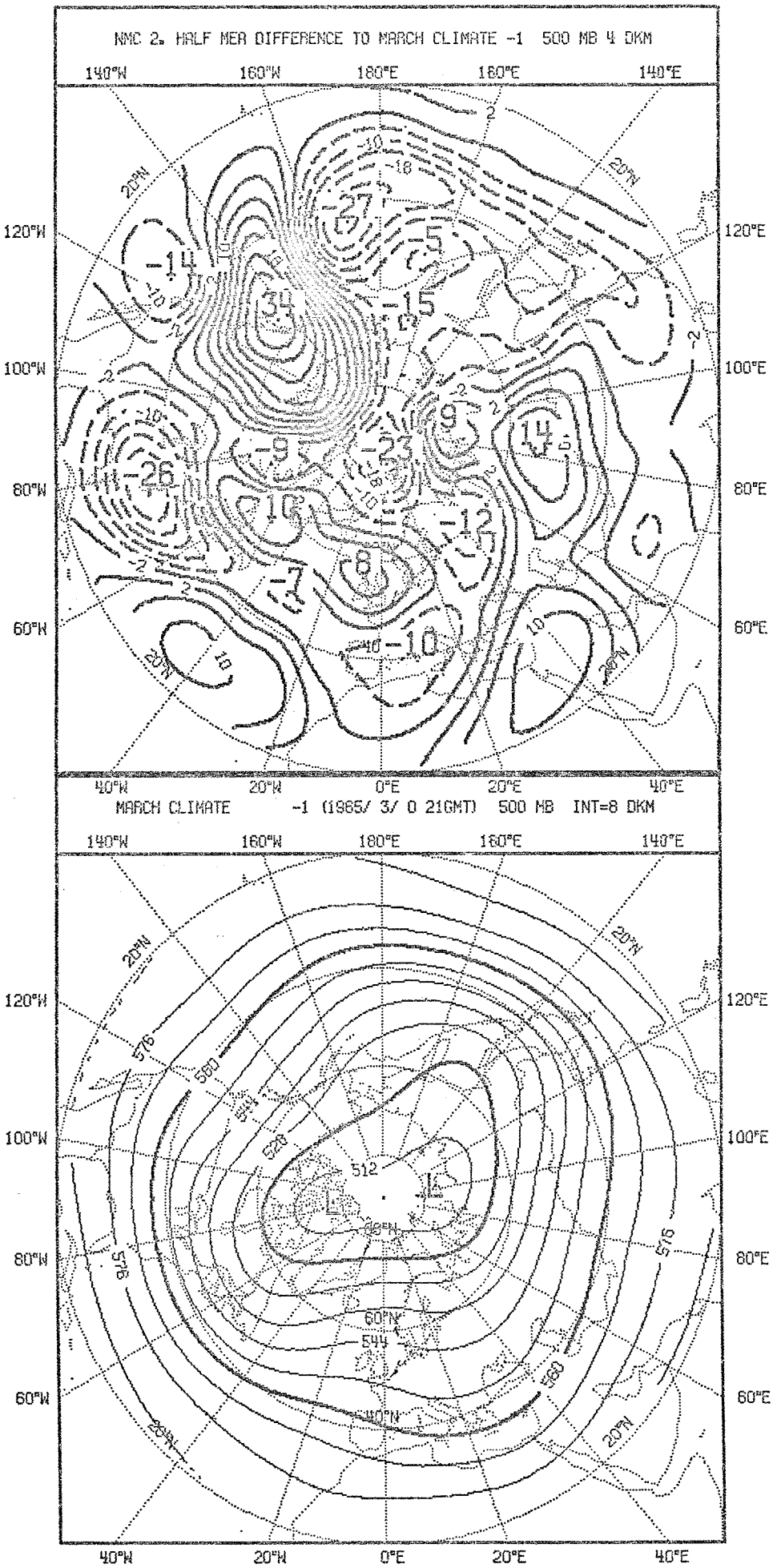

Fig. 3.1.27: Forecast and observed (top right) five day mean, 500 mb anomalies centred on day 7.5.

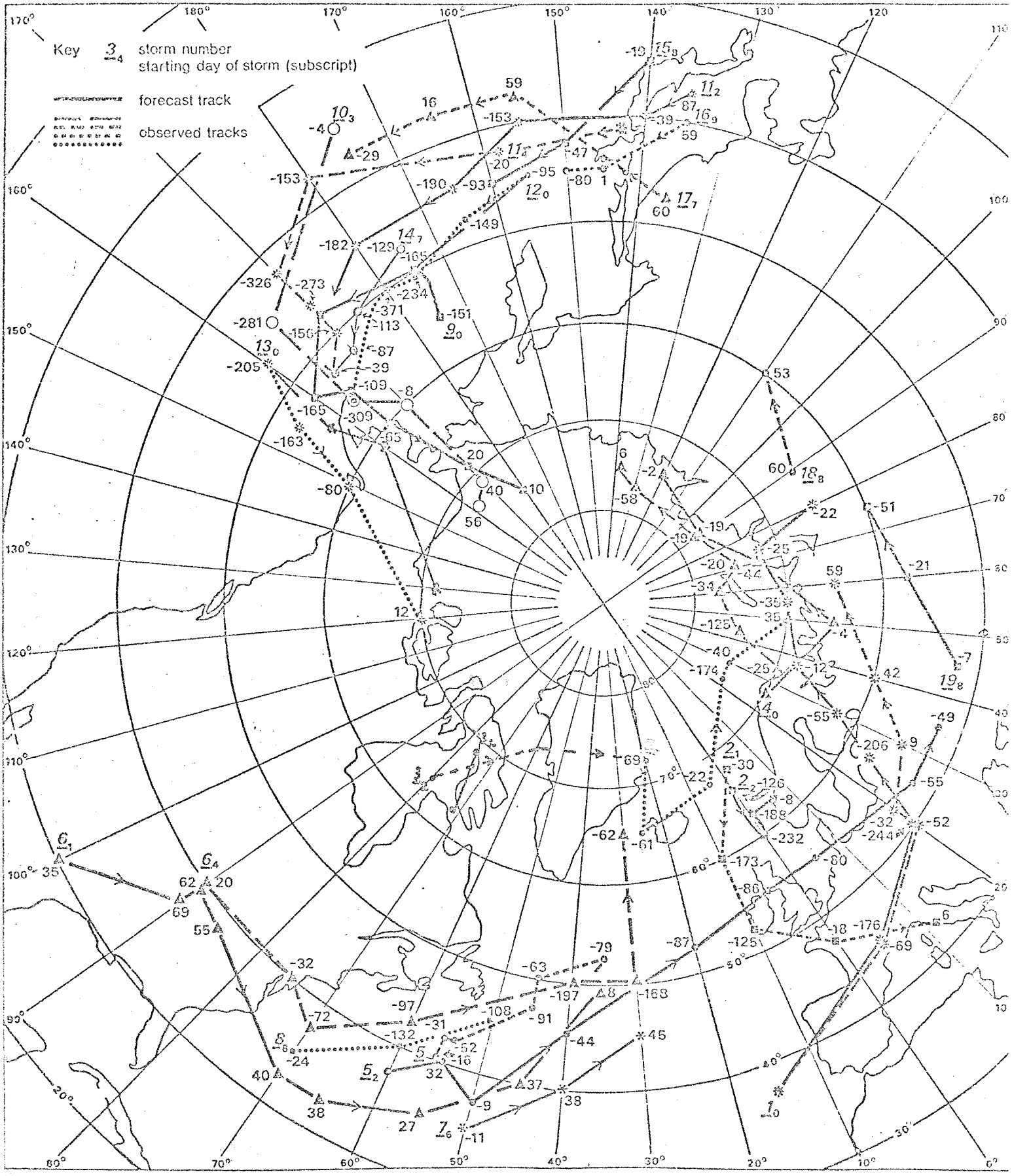

Fig. 3.1.28 : Forecast trajectories by the D24 model of major 1000 mb cyclone centres compared with the observed (NMC).

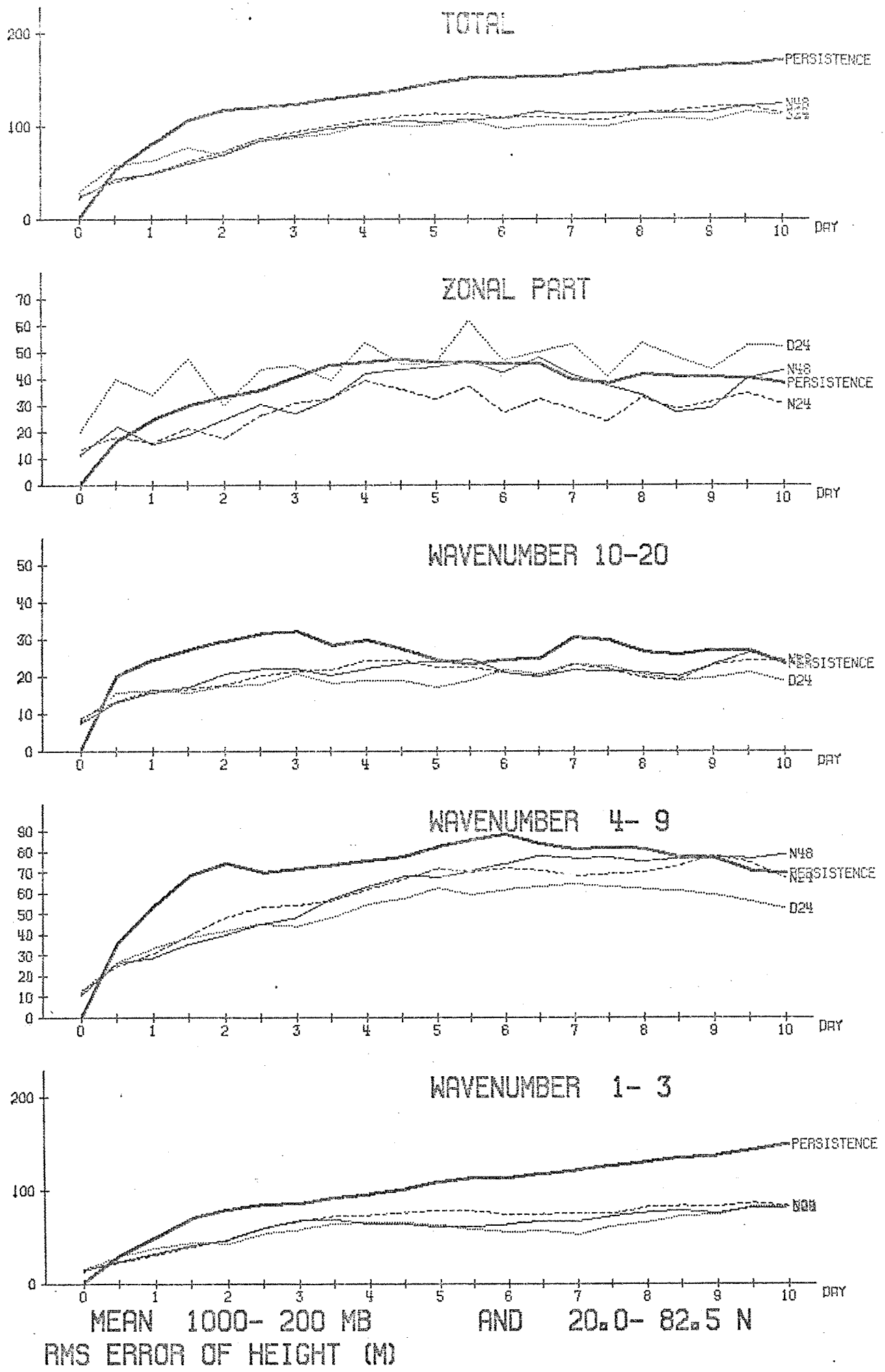
TOTAL
PERSISTENCE
N48
N24
D24
DAY
ZONAL PART
D24
N48
PERSISTENCE
N24
DAY
WAVENUMBER 10-20
N48
PERSISTENCE
D24
DAY
WAVENUMBER 4- 9
N48
PERSISTENCE
N24
D24
DAY
WAVENUMBER 1- 3
PERSISTENCE
N48
DAY
MEAN 1000- 200 MB AND 20.0- 82.5 N
RMS ERROR OF HEIGHT (M)

Fig. 3.2.1

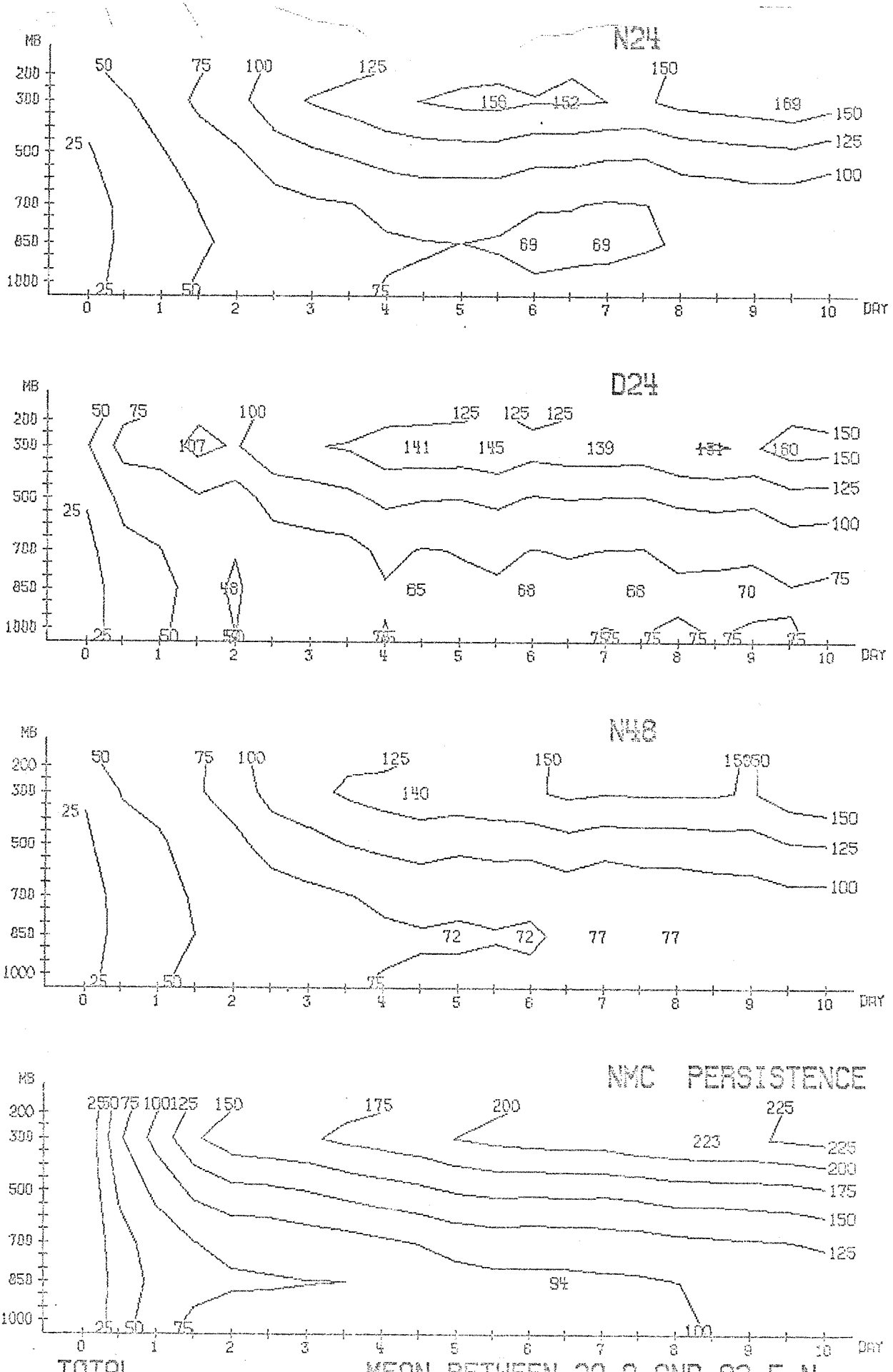
N24
D24
N48
NMC PERSISTENCE
MB
DAY
TOTAL RMS-ERROR OF HEIGHT (M)
MEAN BETWEEN 20.0 AND 82.5 N

Fig. 3.2.2

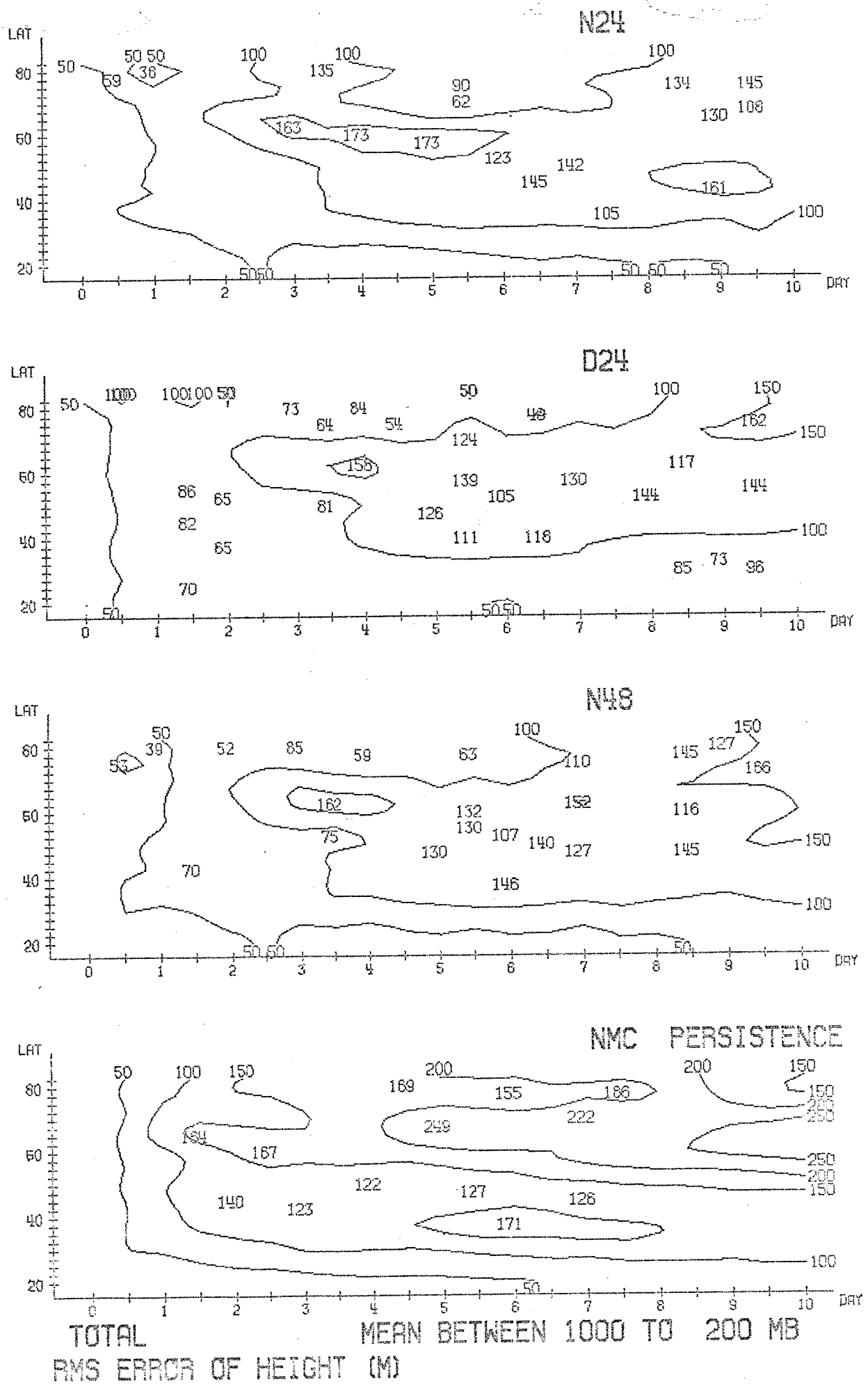
N24
D24
N48
NMC PERSISTENCE
LAT
DAY
TOTAL
MEAN BETWEEN 1000 TO 200 MB
RMS ERROR OF HEIGHT (M)

Fig. 3.2.3

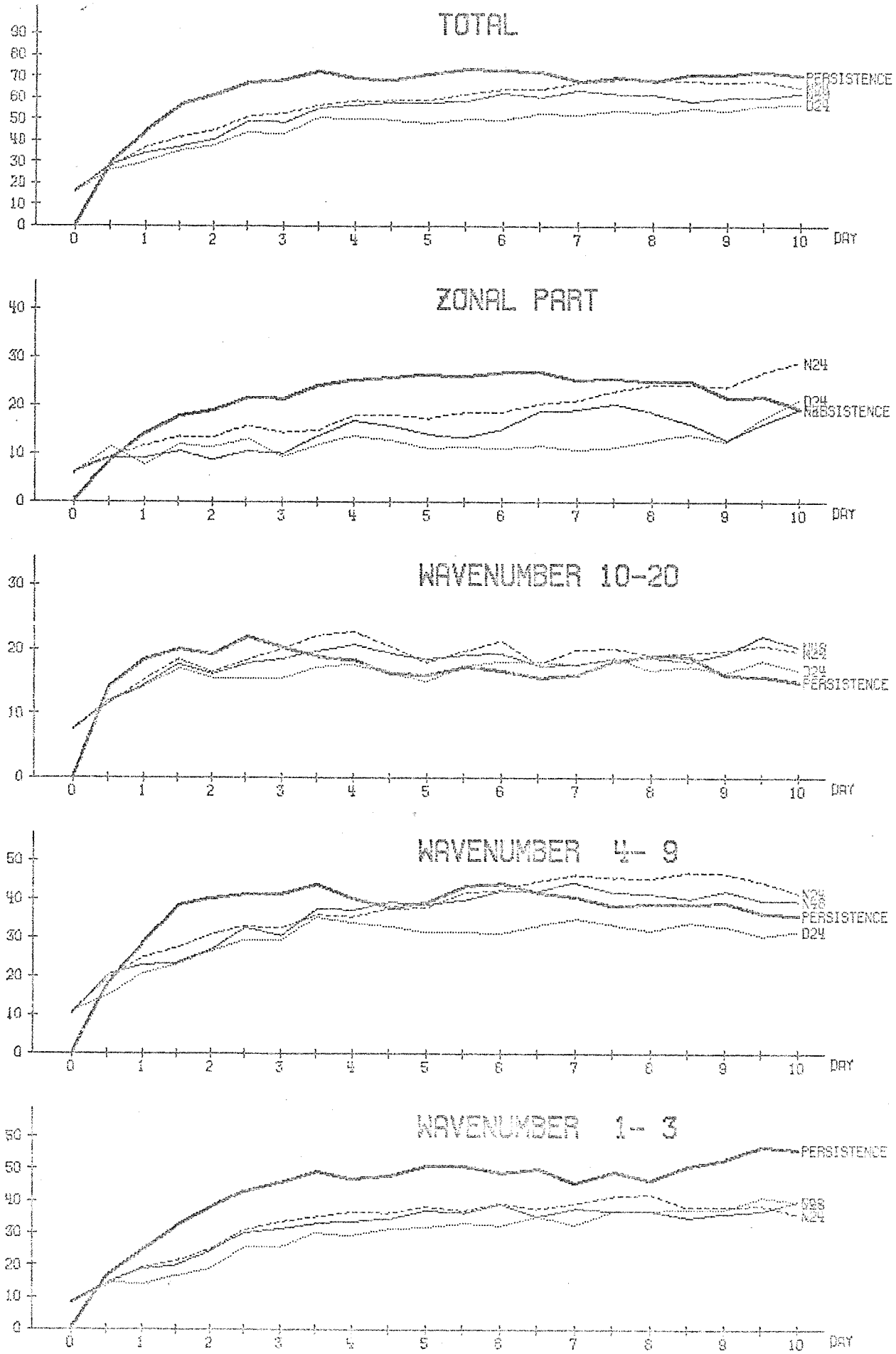
TOTAL
PERSISTENCE
D24
ZONAL PART
N24
D24
PERSISTENCE
WAVENUMBER 10-20
N24
D24
PERSISTENCE
WAVENUMBER 4- 9
N24
PERSISTENCE
D24
WAVENUMBER 1- 3
PERSISTENCE
D24
N24
DAY
MEAN 850- 850 MB AND 20.0- 82.5 N
RMS ERROR OF TEMPERATURE (C/10)

Fig. 3.2.4

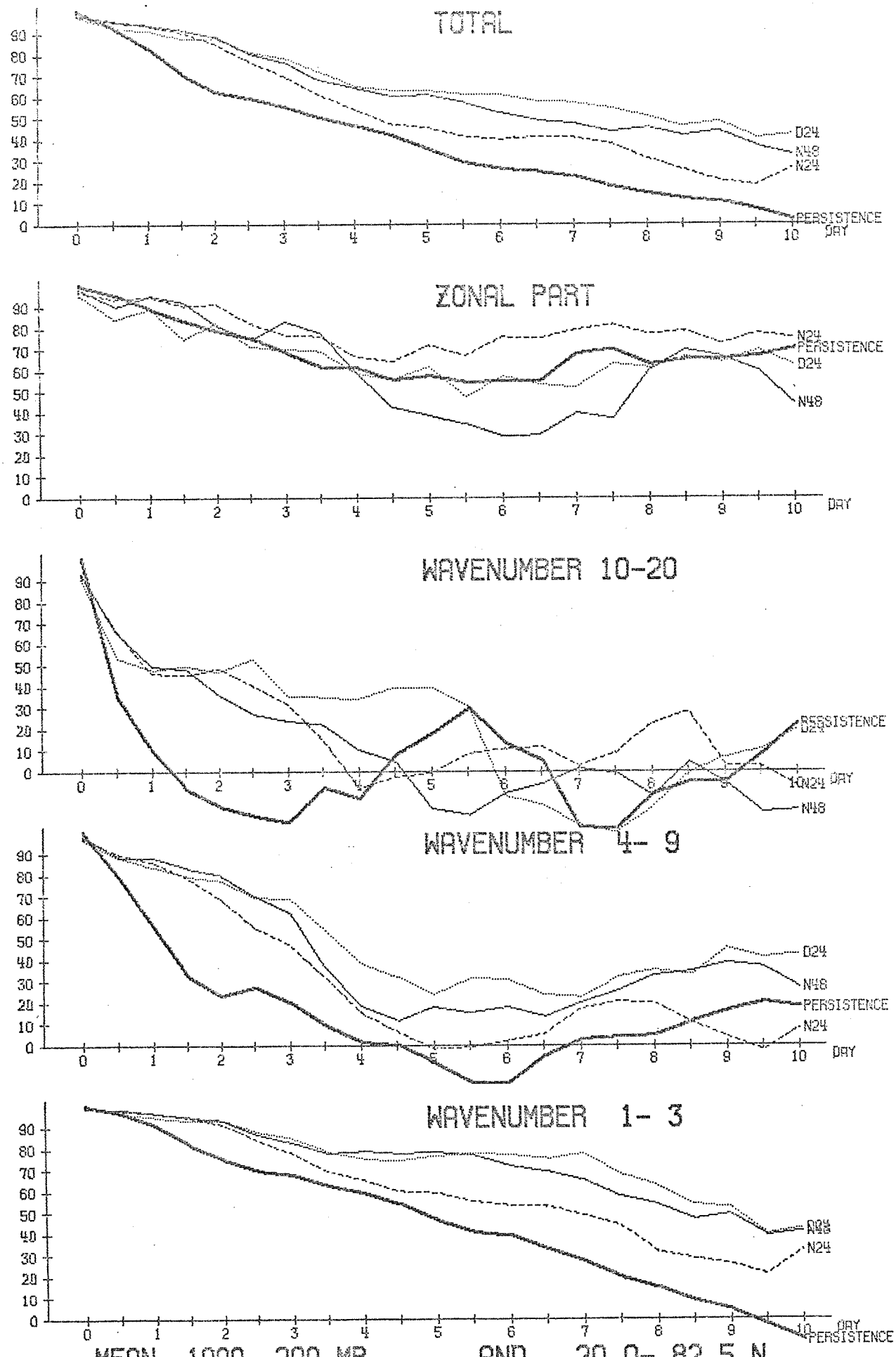
TOTAL
D24
N48
N24
PERSISTENCE
DAY
ZONAL PART
N24
PERSISTENCE
D24
N48
DAY
WAVENUMBER 10-20
PERSISTENCE
D24
N24
N48
DAY
WAVENUMBER 4- 9
D24
N48
PERSISTENCE
N24
DAY
WAVENUMBER 1- 3
D24
N48
N24
PERSISTENCE
DAY
MEAN 1000- 200 MB AND 20.0- 82.5 N
CORRELATION OF HEIGHT %

Fig. 3.2.5

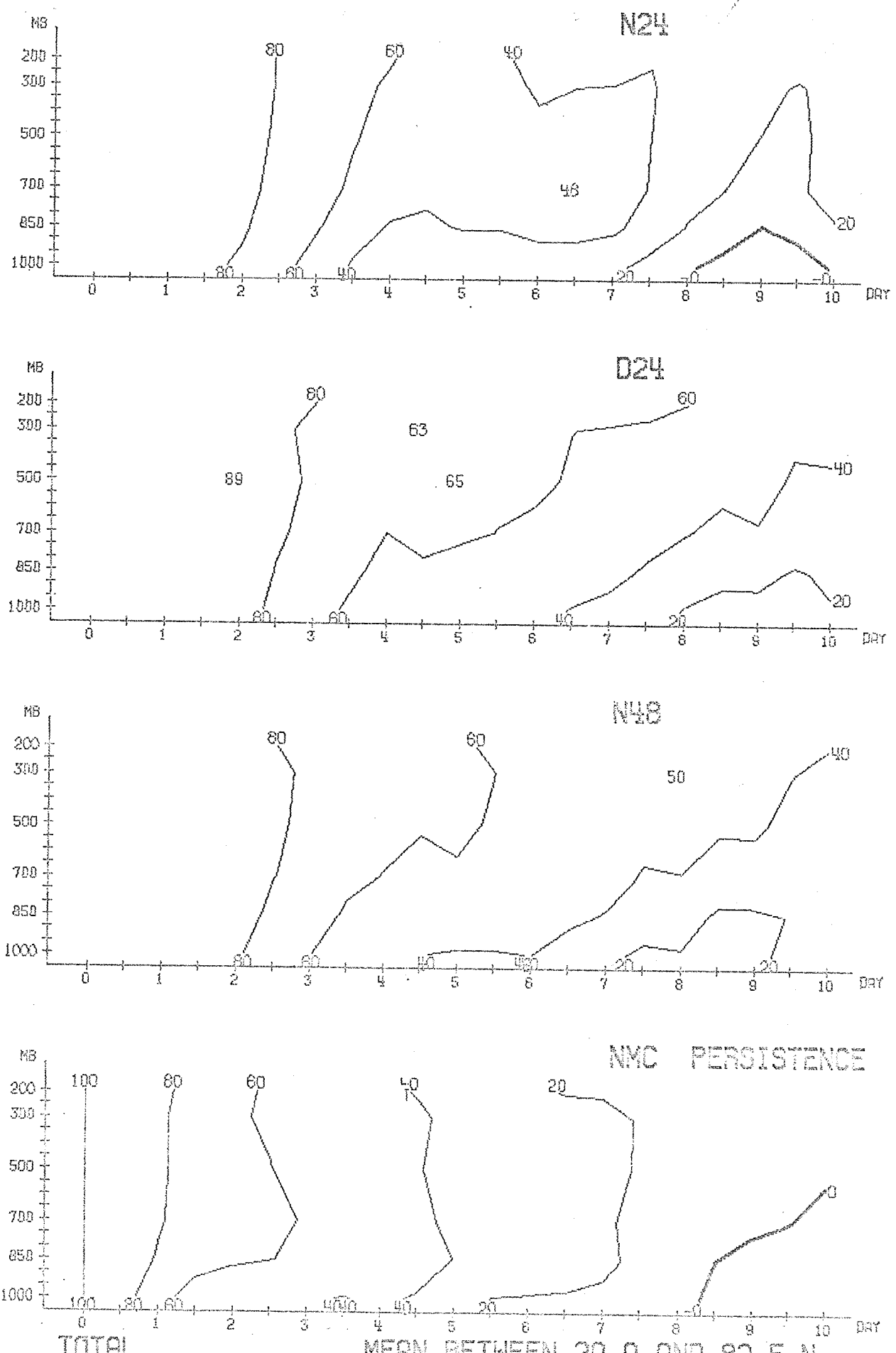
N24
MB
200
300
500
700
850
1000
80
60
40
48
20
0
DAY
D24
89
63
65
N48
50
NMC PERSISTENCE
100
TOTAL
MEAN BETWEEN 20.0 AND 82.5 N
CORRELATION OF HEIGHT Z

Fig. 3.2.6

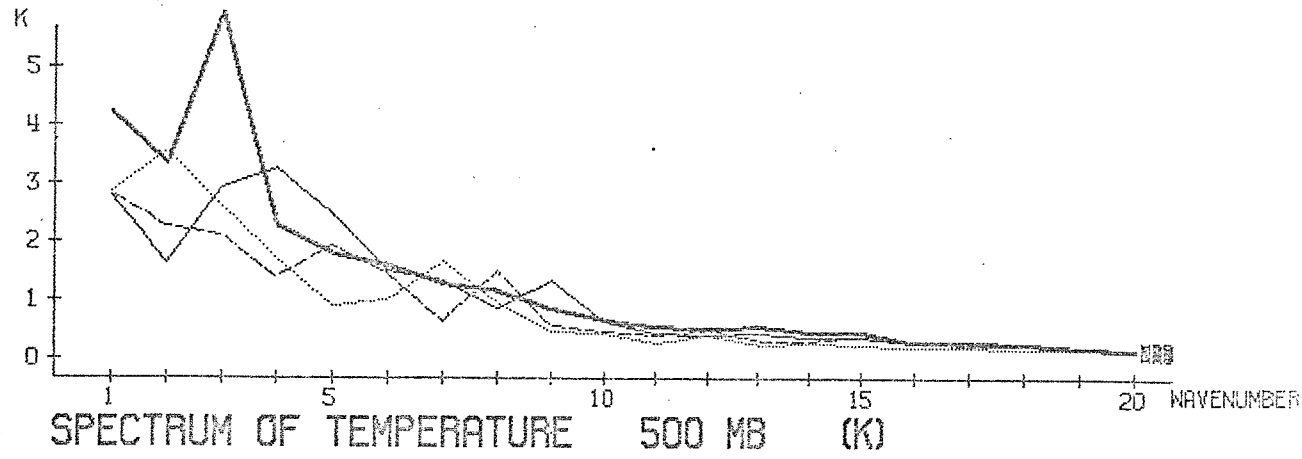

SPECTRUM OF TEMPERATURE 500 MB (K)

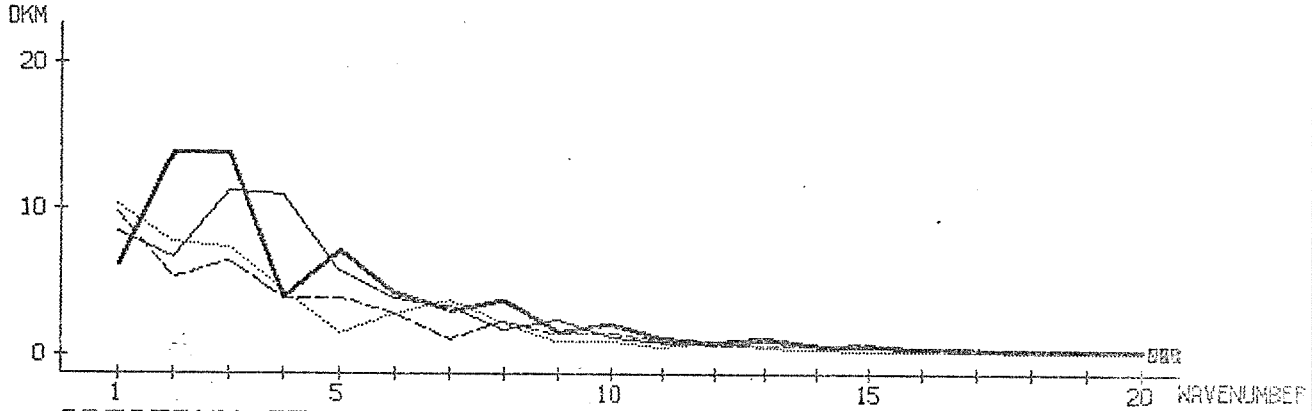

SPECTRUM OF HEIGHT 500 MB (DKM)

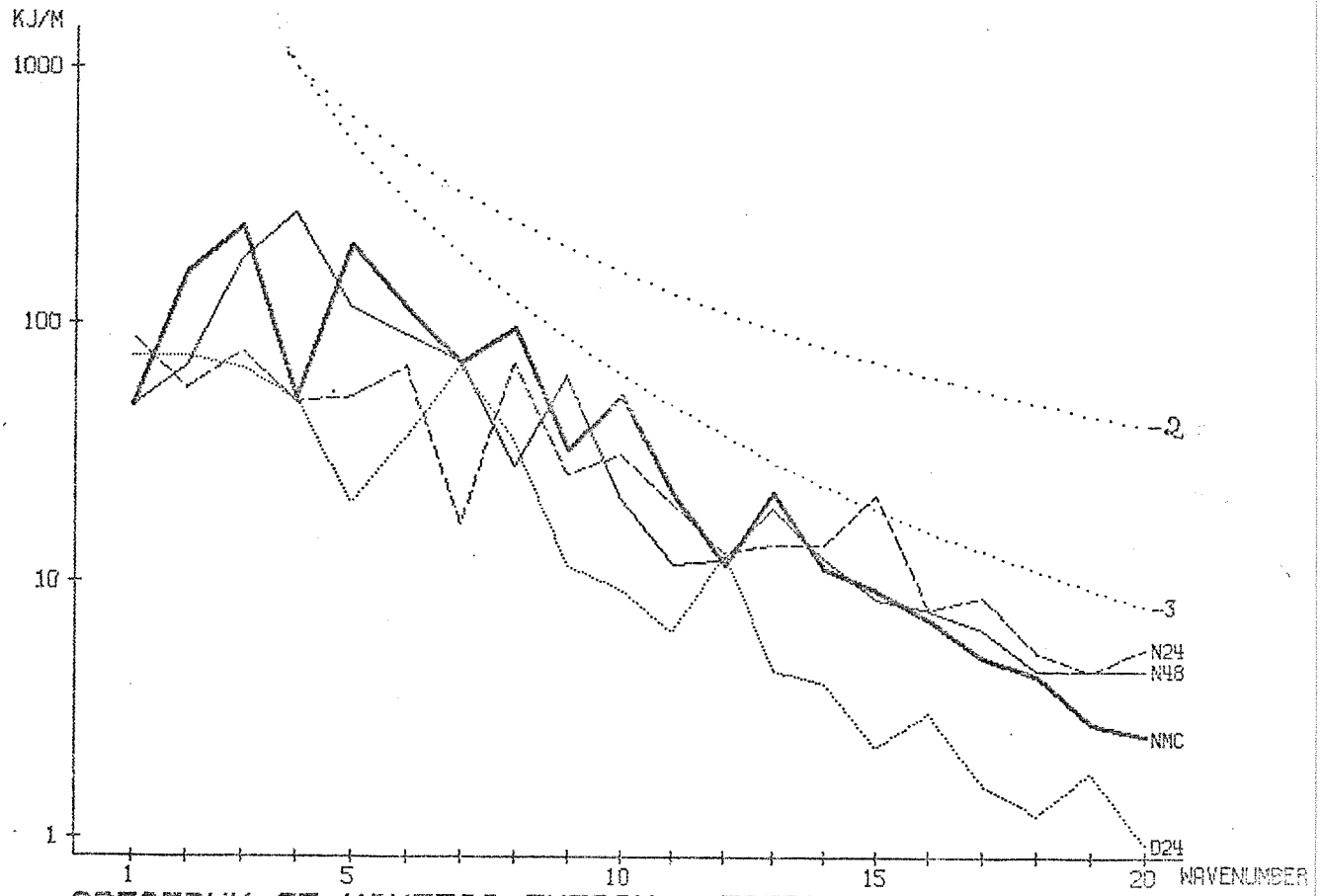

SPECTRUM OF KINETIC ENERGY TROPOSPHERE KJ/M2

DAY 7.5 TO 10.0 MEAN BETWEEN 40.0 AND 60.0

Fig. 3.3.1

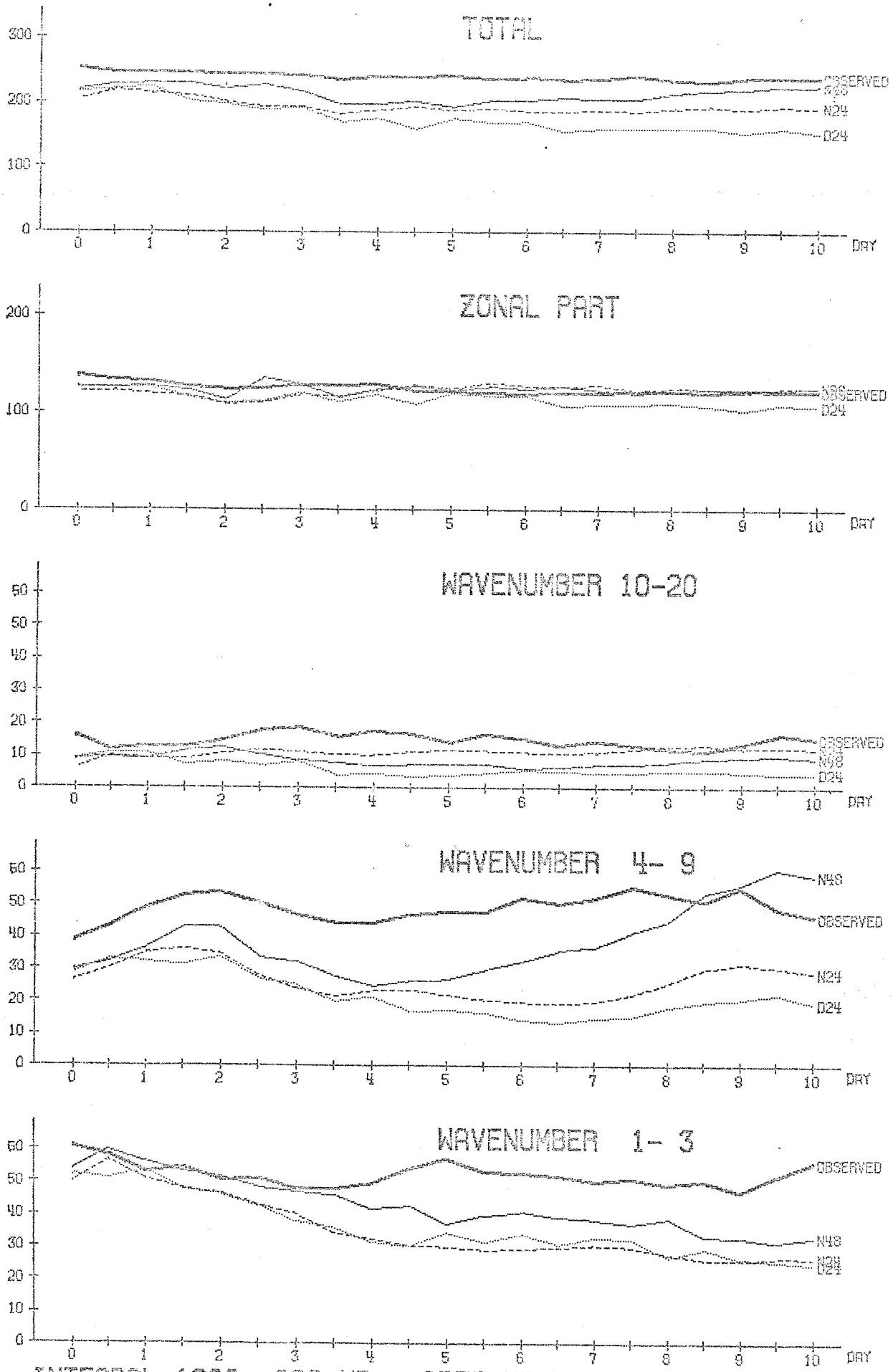
TOTAL
OBSERVED
N24
D24
DAY
ZONAL PART
OBSERVED
D24
DAY
WAVENUMBER 10-20
OBSERVED
N48
N24
D24
DAY
WAVENUMBER 4- 9
N48
OBSERVED
N24
D24
DAY
WAVENUMBER 1- 3
OBSERVED
N48
N24
D24
DAY
INTEGRAL 1000- 200 MB AREA MEAN 20.0- 82.5 N
KE (10 KJ/M2)

Fig. 3.3.2

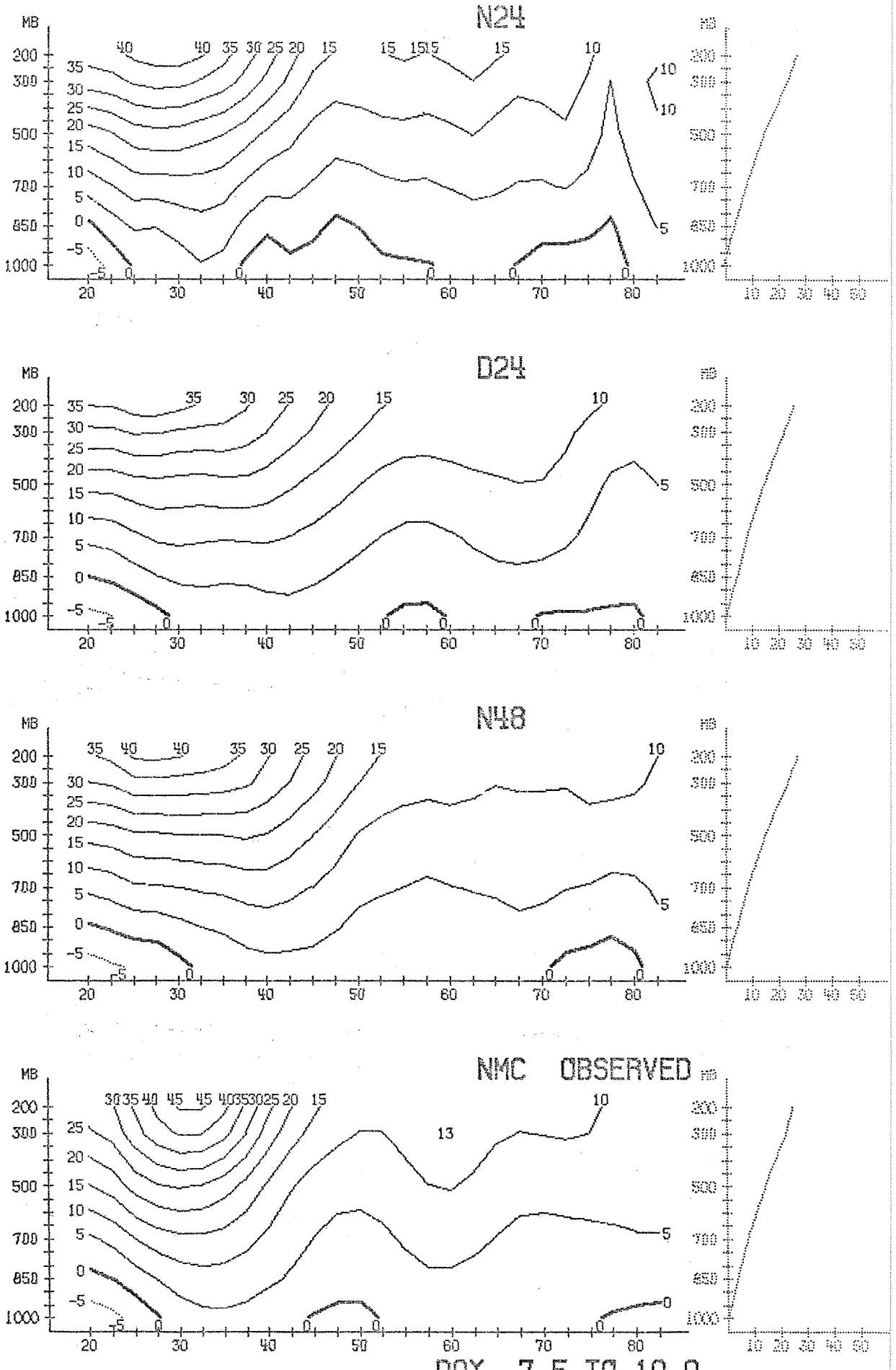
N24
D24
N48
NMC OBSERVED
MB
DAY 7.5 TO 10.0
ZONAL MEAN OF ZONAL WIND (M/SEC)

Fig. 3.3.3

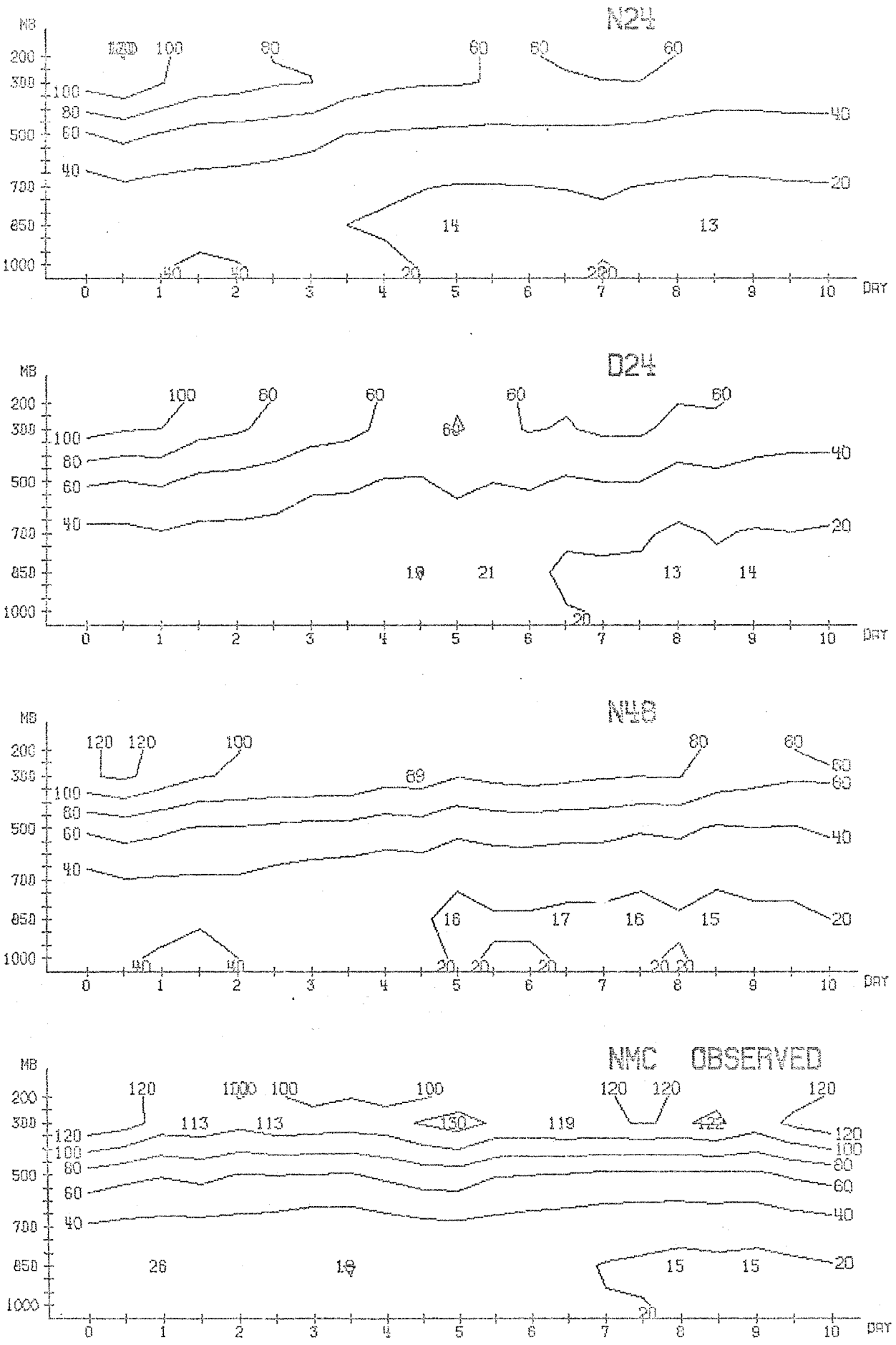
N24
MB
200
300
500
700
850
1000
100
80
60
40
20
14
13
DAY
0
1
2
3
4
5
6
7
8
9
10
D24
MB
200
300
500
700
850
1000
100
80
60
40
20
19
21
13
14
DAY
0
1
2
3
4
5
6
7
8
9
10
N48
MB
200
300
500
700
850
1000
100
80
60
40
20
16
17
16
15
DAY
0
1
2
3
4
5
6
7
8
9
10
NMC OBSERVED
MB
200
300
500
700
850
1000
120
100
80
60
40
20
113
113
119
26
15
15
DAY
0
1
2
3
4
5
6
7
8
9
10
WAVENUMBER 1- 3 MEAN BETWEEN 20.0 AND 82.5 N
KE (10 KJ/M2/BAR)

Fig. 3.3.4

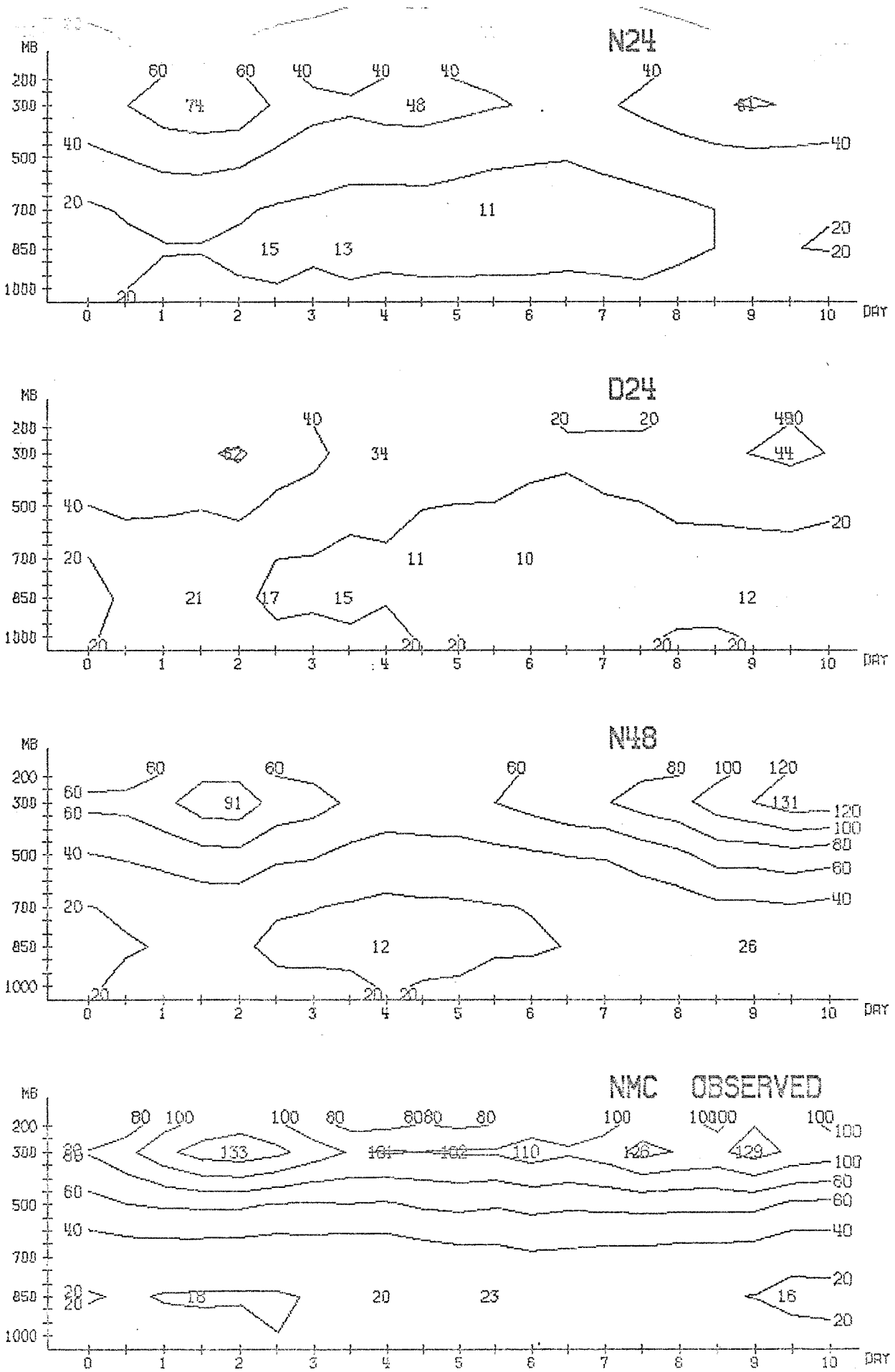
N24
MB
200
300
500
700
850
1000
60
60
40
40
40
40
74
48
40
40
20
11
15
13
20
20
20
0
1
2
3
4
5
6
7
8
9
10
DAY
D24
MB
200
300
500
700
850
1000
40
20
20
480
44
34
40
20
20
11
10
21
17
15
12
20
20
20
20
20
0
1
2
3
4
5
6
7
8
9
10
DAY
N48
MB
200
300
500
700
850
1000
60
60
60
60
40
20
91
60
80
100
120
131
120
100
80
60
40
12
26
20
20
20
0
1
2
3
4
5
6
7
8
9
10
DAY
NMC OBSERVED
MB
200
300
500
700
850
1000
80
100
100
80
80
80
80
100
100
100
100
133
161
102
110
126
129
100
100
60
60
40
60
40
20
20
15
20
23
16
20
0
1
2
3
4
5
6
7
8
9
10
DAY
WAVENUMBER 4- 9 MEAN BETWEEN 20.0 AND 82.5 N
KE (10 KJ/M2/BAR)

Fig. 3.3.5

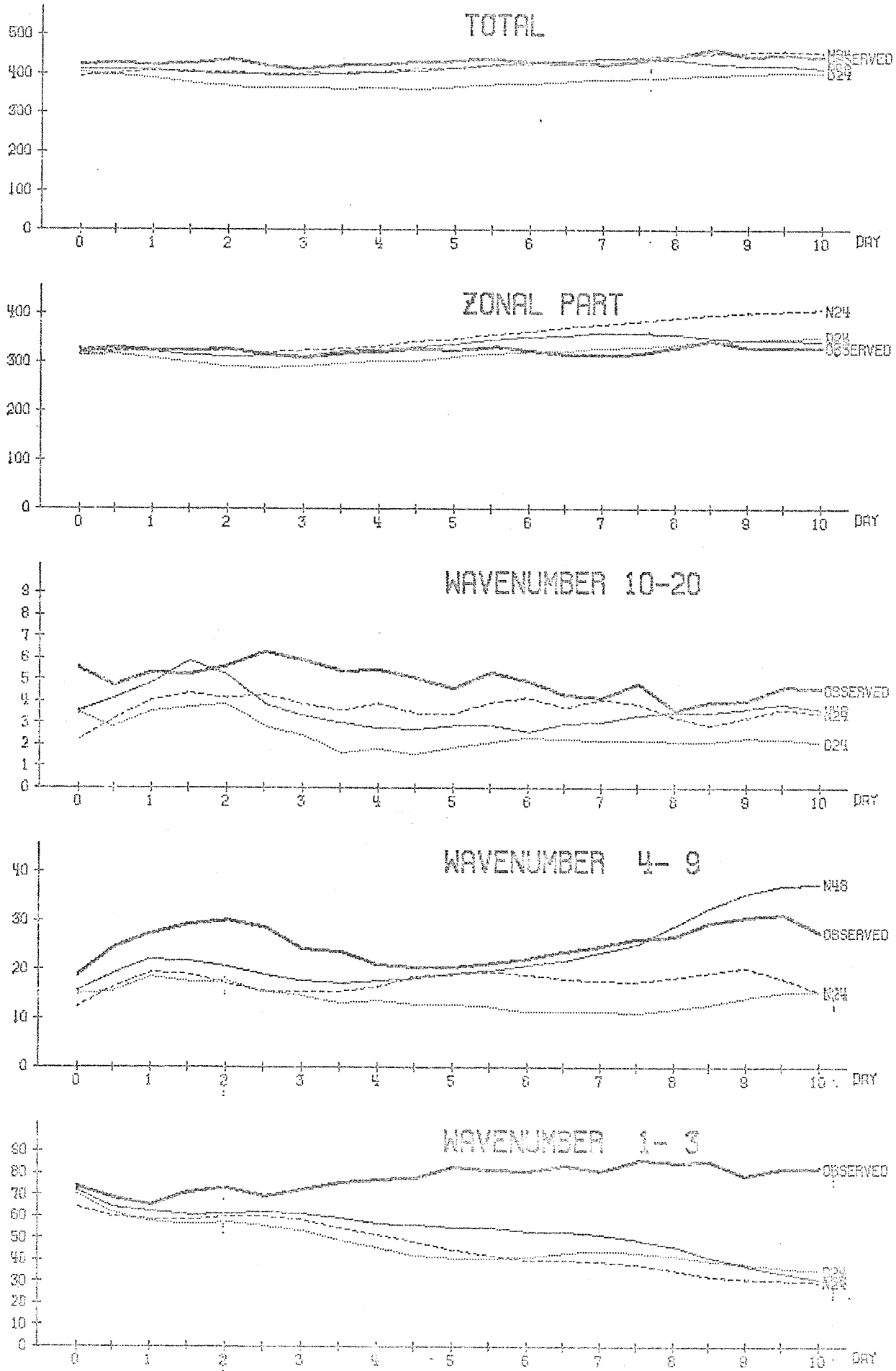

INTEGRAL 850- 200 MB AREA MEAN 20.0- 82.5 N
RE (10 KJ/M2)

Fig. 3.3.6

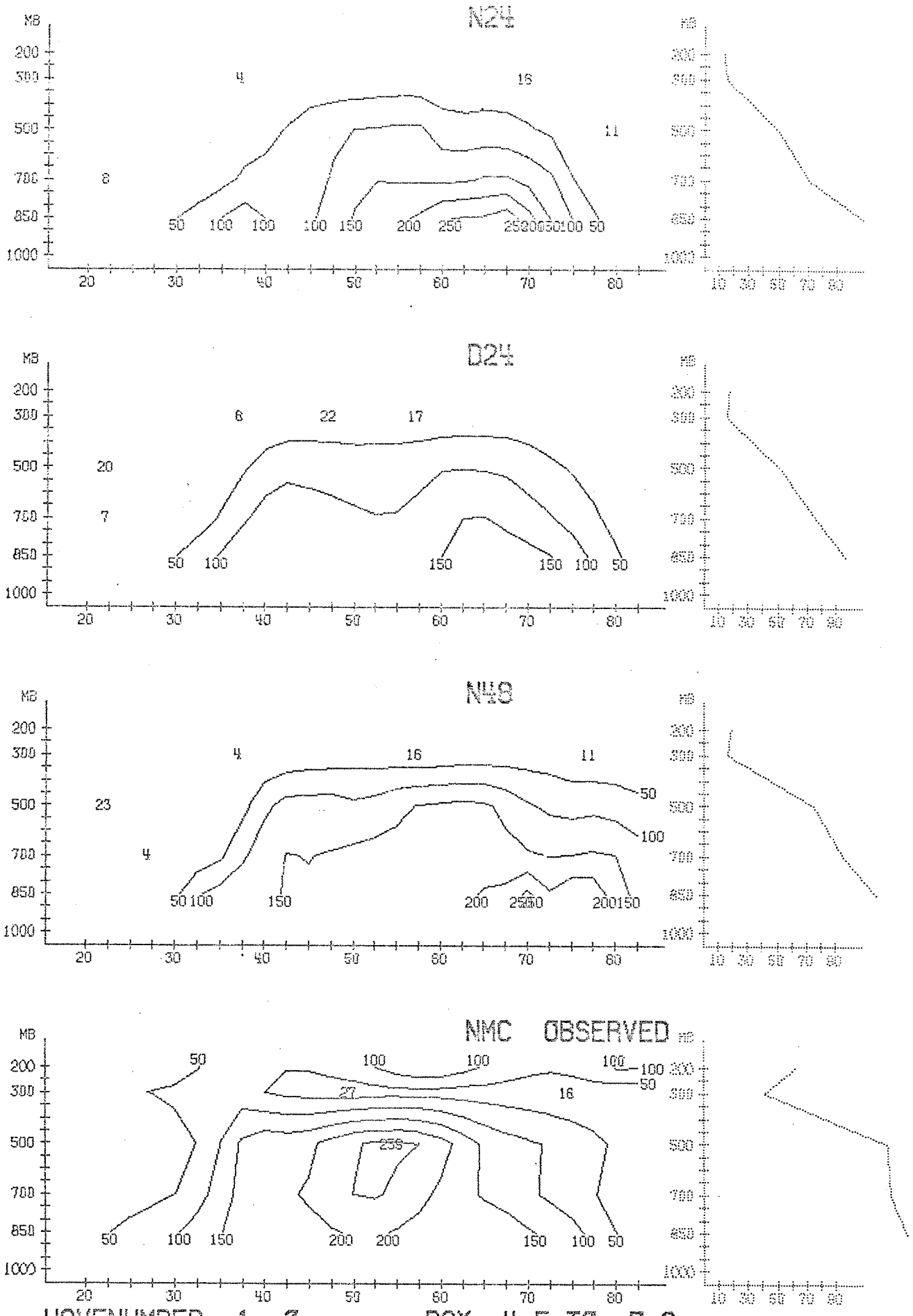
N24
D24
N48
NMC OBSERVED
MB
200
300
500
700
850
1000
20
30
40
50
60
70
80
WAVENUMBER 1- 3
DAY 4.5 TO 7.0
AE (10 KJ/M2/BAR)

Fig. 3.3.7

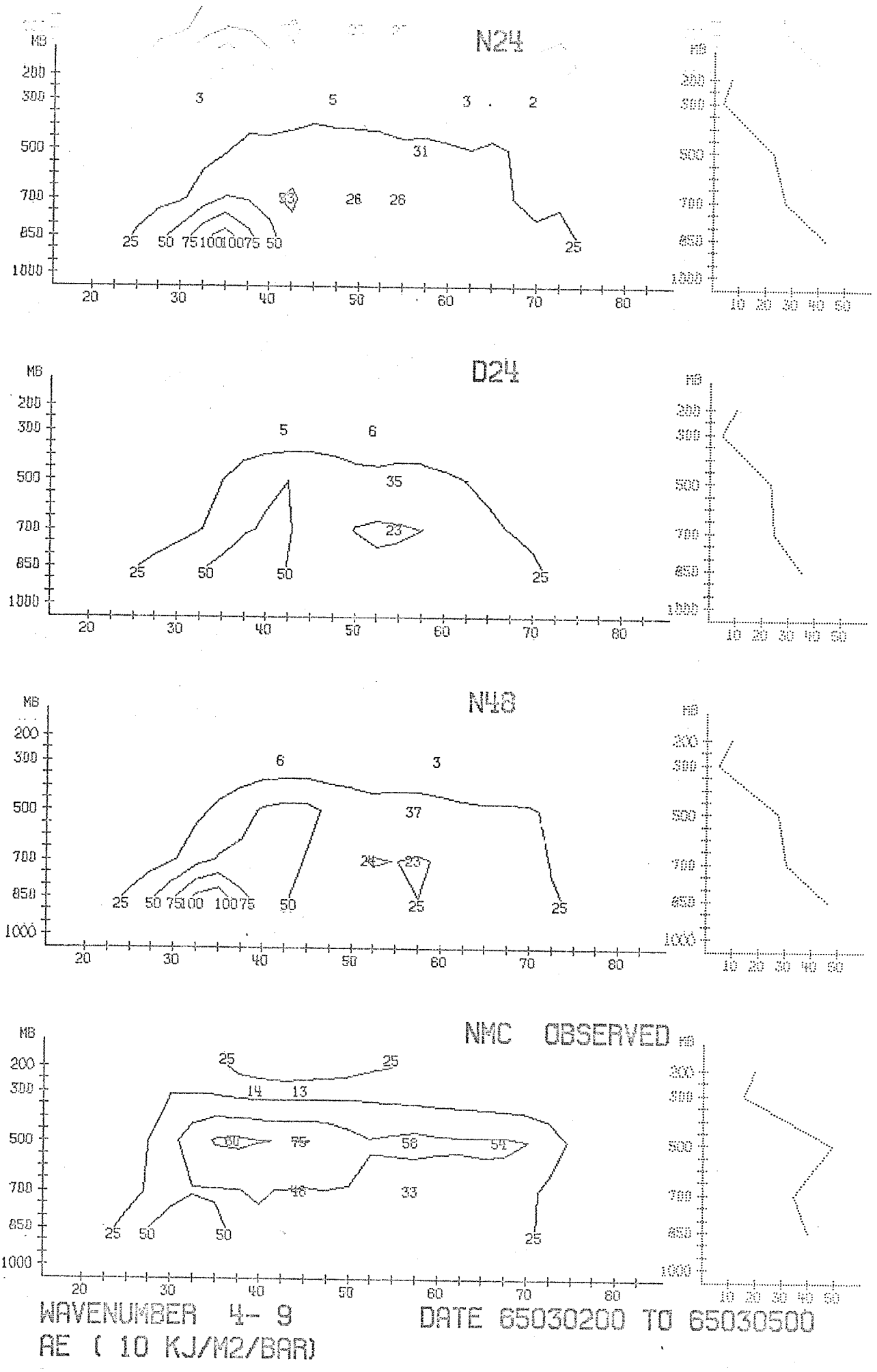
N24
D24
NW8
NMC OBSERVED
MB
200
300
500
700
850
1000
20
30
40
50
60
70
80
10
WAVENUMBER 4- 9
DATE 65030200 TO 65030500
RE (10 KJ/M2/BAR)

Fig. 3.3.8

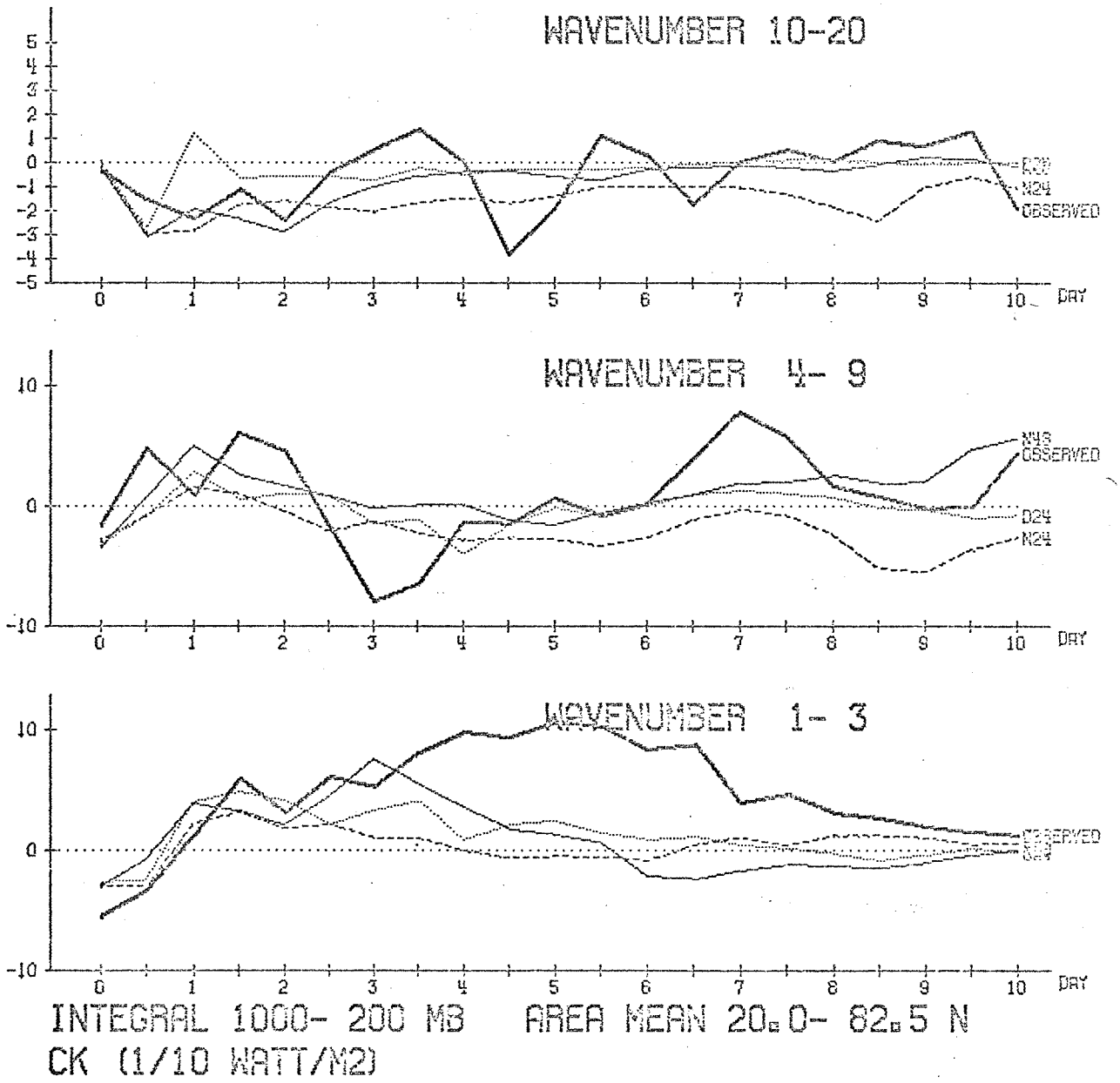
WAVENUMBER 10-20
5
4
3
2
1
0
-1
-2
-3
-4
-5
0
1
2
3
4
5
6
7
8
9
10
DAY
OBSERVED
N24
WAVENUMBER 4- 9
10
0
-10
N48
OBSERVED
D24
N24
WAVENUMBER 1- 3
OBSERVED
INTEGRAL 1000- 200 MB AREA MEAN 20.0- 82.5 N
CK (1/10 WATT/M2)

Fig. 3.3.9

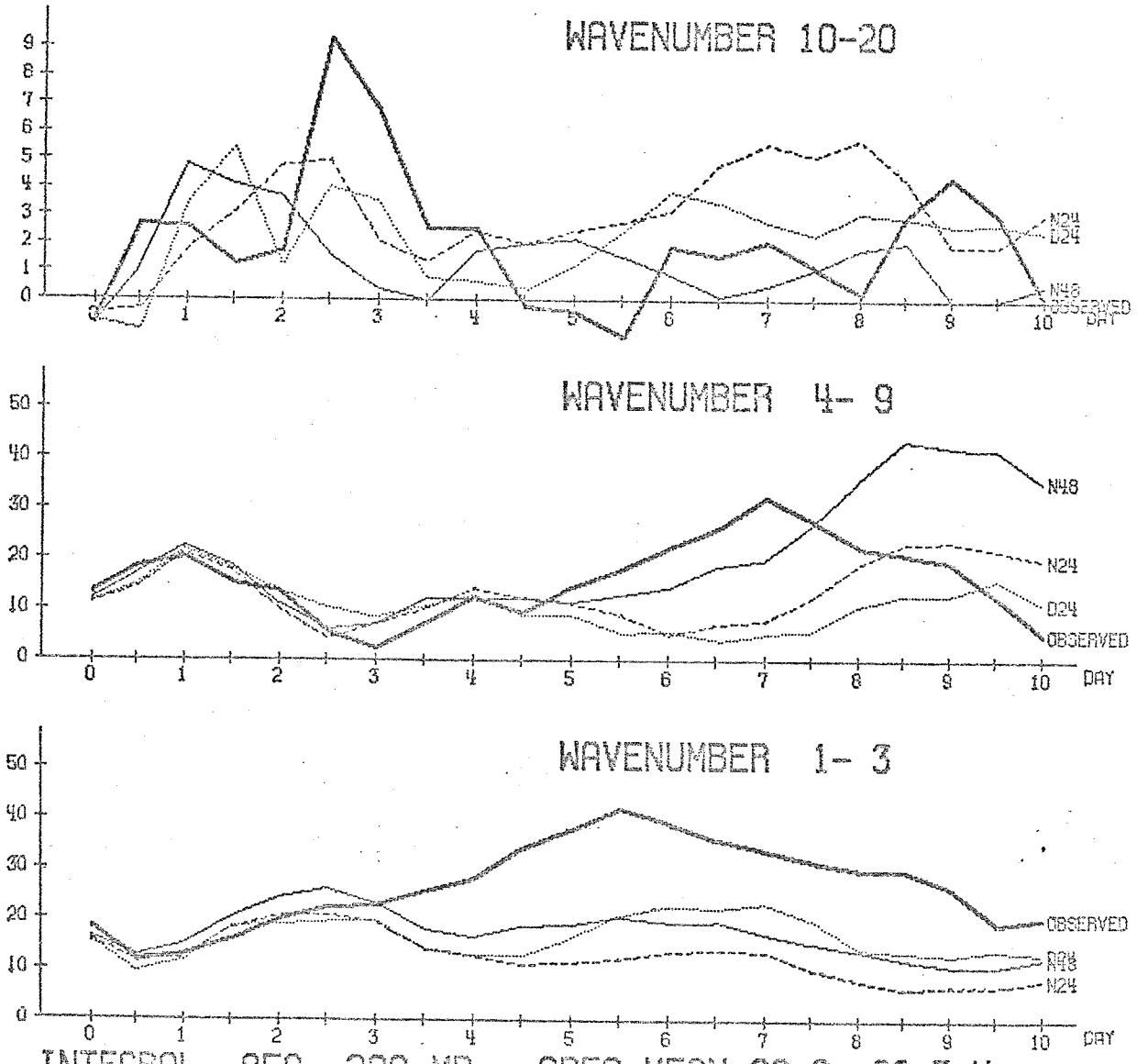

Fig. 3.3.10

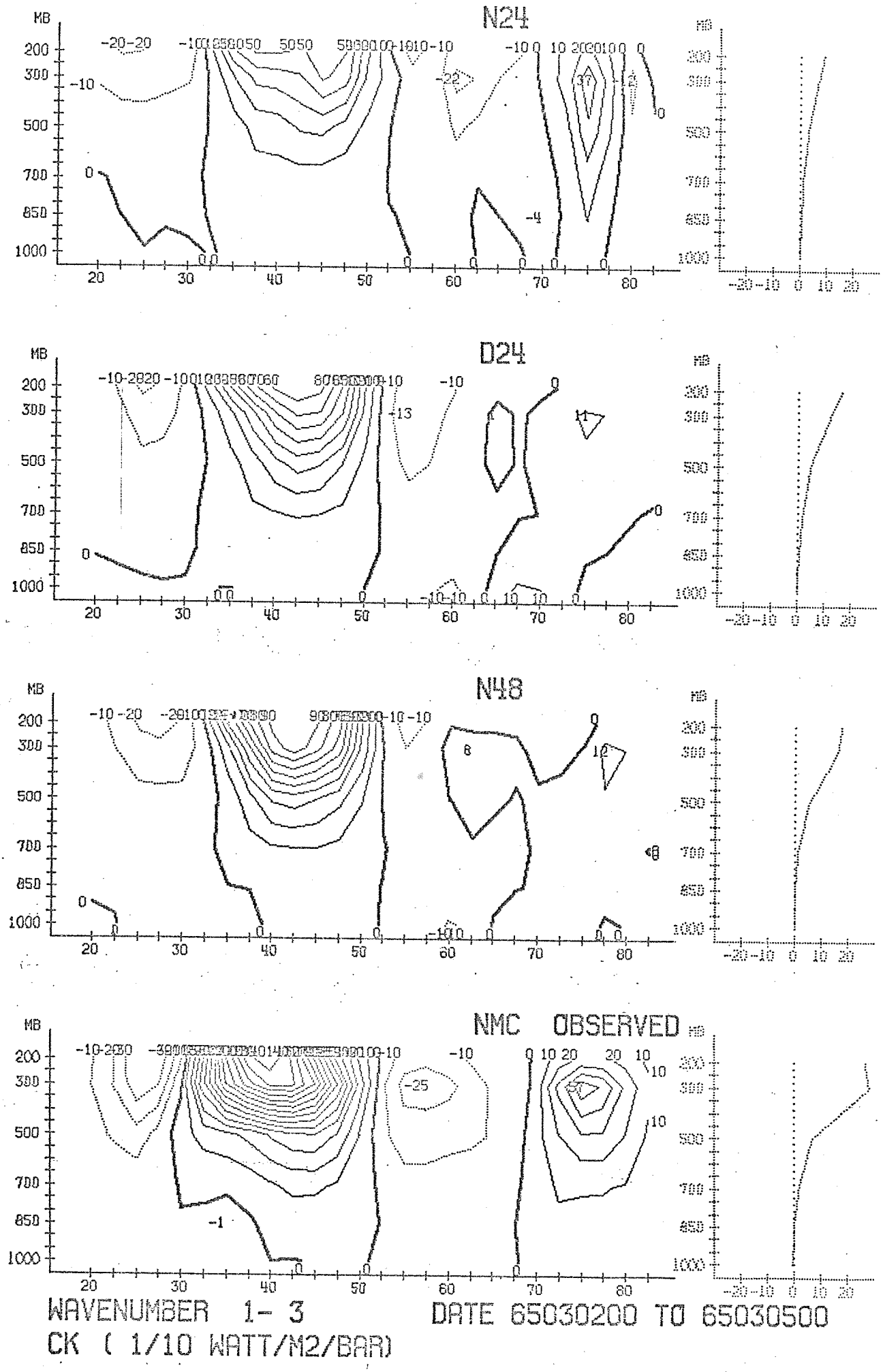
N24
D24
N48
NMC OBSERVED
MB
200
300
500
700
850
1000
20
30
40
50
60
70
80
-20 -10 0 10 20
WAVENUMBER 1- 3
DATE 65030200 TO 65030500
CK (1/10 WATT/M2/BAR)

Fig. 3.3.11